Quantum coherences in glycine probed with femtosecond x-rays

Dissertation
zur Erlangung des Doktorgrades
an der Fakultät für Mathematik, Informatik und Naturwissenschaften
Fachbereich Physik
der Universität Hamburg

vorgelegt von

David Schwickert

Hamburg

2022

Gutachter der Dissertation:	Priv.-Doz. Dr. Tim Laarmann Prof. Dr. Markus Drescher
Zusammensetzung der Prüfungskommission:	Priv.-Doz. Dr. Tim Laarmann Prof. Dr. Markus Drescher Prof. Dr. Daniela Pfannkuche Priv.-Doz. Dr. Michael Martins Prof. Dr. Nils Huse
Vorsitzende der Prüfungskommission:	Prof. Dr. Daniela Pfannkuche
Datum der Disputation:	31.03.2022
Vorsitzender Fach-Promotionsausschuss PHYSIK:	Prof. Dr. Wolfgang J. Parak
Leiter des Fachbereichs PHYSIK:	Prof. Dr. Günter H. W. Sigl
Dekan der Fakultät MIN:	Prof. Dr. Heinrich Graener

Eidesstattliche Versicherung / Declaration on oath

Hiermit versichere ich an Eides statt, die vorliegende Dissertationsschrift selbst verfasst und keine anderen als die angegebenen Hilfsmittel und Quellen benutzt zu haben.

Hamburg, den 20.02.2022

Unterschrift des Doktoranden

In Gedenken an meinen Zweitbetreuer Prof. Dr. Wilfried Wurth.

Abstract

Intramolecular charge migration plays a key role in photochemical reactions of bio-relevant molecules. This work combines ultrashort free-electron laser soft x-ray pulses with a kinematically complete pump-probe absorption measurement in order to monitor electronic and nuclear wave packet dynamics.

The Free-Electron LASer in Hamburg (FLASH) at the *Deutsches Elektronen-Synchrotron*[1] DESY is capable of producing single-mode Self-Amplified Spontaneous Emission (SASE) radiation with a bandwidth of $\Gamma = 0.37\%$ at a central wavelength of $\lambda = 4.55\,\mathrm{nm}$ ($E_{\mathrm{ph}} = 272.7\,\mathrm{eV}$). The small bandwidth of the ultrashort pulses allows for precise resonant or off-resonant excitation of molecular states. A self-developed grating-mirror based 'Split-and-Delay Unit' (SDU) [1, 2] enables the study of the temporal evolution of molecular states and more specifically intramolecular electronic wave packet dynamics with attosecond precision and up to picosecond range.

In the present experiment, the generation, migration and fate of a transient hole state in the simplest, proteinogenic amino acid glycine (NH_2–CH_2–COOH) is studied on a 175 fs time scale with ∼1 fs resolution. Purely electronic coherences are observed during the first 25 fs. Selected events, where the initial x-ray pump pulse ionizes the molecule and creates a pure one-hole (1h) state in the inner-valence 10a′ molecular orbital (MO) lead due to a level splitting of $(219^{+41}_{-30})\,\mathrm{meV}$ of the 10a′ MO and superposition of the pure 1h state and a mixture of two-hole-one-particle (2h1p) configurations to a periodic charge density oscillation throughout the molecule with a time period of (18.9 ± 3.0) fs. When the two-state system is periodically prepared in the 1h configuration, the x-ray probe pulse can resonantly excite a carbon core electron to fill the 10a′ hole. Subsequent Auger decay leaves behind a doubly charged glycine dication and an Auger electron, whose observed yield gives information about the electronic coherence at the time of the probe pulse absorption. Alternatively, if the x-ray photon energy is tuned out of the transition resonance, sequential double photoionization of a further valence orbital is the dominant process, which shows an equal maximum periodic relative yield change of $(20 \pm 11)\%$ with a period of (18.1 ± 0.7) fs. In this case, a π-phase shift is present between the delay-dependent yield of photoelectrons below and above the kinetic energy of (246 ± 2) eV, due to ionization transitions of higher-energy 1h to 2h or lower-energy cationic 2h1p to dicationic 3h1p final states.

After (46 ± 8.9) fs pump-probe delay, non-adiabatic coupling between electronic and nuclear degrees of freedom give rise to a vibronic oscillation of comparable strength as the electronic coherence but with a time period of (29.0 ± 4.0) fs.

The experimental results are complemented with *ab initio* many-electron simulations, using the exact same experimental pulse parameters, performed by Marco Ruberti, Imperial College London [3, 4], which are in perfect agreement with the obtained experimental electronic coherence oscillation period. However, computational models are still unable to couple electronic and nuclear degrees of freedom for complicated systems and cannot verify the experimentally observed vibronic oscillation period.

[1] transl.: 'German electron-synchrotron'

Zusammenfassung

Intramolekulare Ladungsbewegungen spielen eine Schlüsselrolle in photochemischen Reaktionen biorelevanter Moleküle. Diese Arbeit vereint ultrakurze weiche Röntgenpulse eines Freie-Elektronen-Lasers mit einer kinematisch vollständigen Pump-Probe[2]-Absorptionsmessung, um elektronische und nukleare Wellenpacketdynamiken nachzuverfolgen.

Der Freie-Elektronen LASer in Hamburg (FLASH) am Deutschen Elektronen-Synchrotron DESY ist in der Lage ein-modige selbstverstärkte spontane Emissionsstrahlung (SASE[3]) mit einer Bandbreite von $\Gamma = 0.37\%$ bei einer zentralen Wellenlänge von $\lambda = 4.55\,\mathrm{nm}$ ($E_{\mathrm{ph}} = 272.7\,\mathrm{eV}$) zu erzeugen. Die schmale Bandbreite der ultrakurzen Pulse erlaubt die präzise resonante oder nicht-resonante Anregung von Molekülzuständen. Eine selbstentwickelte, auf Gitterspiegeln basierende Strahlteilungs- und Verzögerungseinheit (SDU[4]) [1, 2] ermöglicht die Studie der zeitlichen Entwicklung von Molekülzuständen und insbesondere intramolekularen elektronischen Wellenpacketdynamiken mit Attosekunden-Genauigkeit und bis zu Picosekunden-Reichweite.

Das vorliegende Experiment untersucht die Erzeugung, Wanderung und das Schicksal eines kurzlebigen Lochzustands in der einfachsten, proteinogenen Aminosäure Glycin (NH_2–CH_2–COOH) auf einer 175 fs Zeitskala mit ∼1 fs Auflösung. Rein elektronische Kohärenzen wurden während den ersten 25 fs nachgewiesen. Selektierte Ereignisse, bei denen der erste Röntgenanregungspuls das Molekül ionisiert und einen reinen Ein-Loch-Zustand (1h) im innervalenten 10a′ Molekülorbital (MO) erzeugt, führen aufgrund einer Niveauaufspaltung des 10a′ MOs von (219^{+41}_{-30}) meV und Superposition des reinen 1h-Zustands mit einer Mischung aus Zwei-Loch-Ein-Teilchen-Konfigurationen (2h1p) zu einer eine periodischen Ladunsdichteoszillation innerhalb des gesamten Moleküls mit einer Zeitperiode von (18.9 ± 3.0) fs. Sobald das Zweizustandssystem sich periodisch in der 1h-Konfiguration befindet, kann der Röntgenabtastpuls resonant ein Kohlenstoffkernelektron anregen und das 10a′ Loch füllen. Nachfolgender Augerzerfall hinterlässt ein zweifach geladenes Glycindikation und ein Augerelektron, dessen beobachtete Ausbeute Auskunft über die elektronische Kohärenz zur Zeit der Abtastabsorption gibt. Falls die Röntgenphotonenenergie nicht resonant zu dem Übergang gestimmt ist, ist alternativ die sequentielle Doppelionisation der dominierende Prozess, welche zu einer gleichstarken maximalen periodischen relativen Ausbeute von $(20 \pm 11)\%$ mit (18.1 ± 0.7) fs Periode führt. In diesem Fall liegt ein Phasensprung um π zwischen der verzögerungsabhängigen Ausbeute von Photoelektronen unter und über (246 ± 2) eV vor, aufgrund von Ionisationen von höherenergetischen 1h zu 2h oder niedrigerenergetischen kationischen 2h1p zu dikationischen 3h1p Zuständen.

Nach (46 ± 8.9) fs Pump-Probe-Zeitverzögerung veranlasst nichtadiabatische Kopplung zwischen elektronischen und nuklearen Freiheitsgraden vibronische Schwingungen mit vergleichbarer Stärke zur elektronischen Kohärenz aber mit einer Zeitperiode von (29.0 ± 4.0) fs.

Die experimentellen Ergebnisse werden durch *ab initio* Vielelektronenberechnungen unter Verwendung von mit dem Experiment identischen Pulsparametern von Marco Ruberti, vom Imperial College London [3, 4] komplementiert, die mit der gemessenen Oszillationsperiode der elektronischen Kohärenz vollständig übereinstimmen. Allerdings, gelingt es rechnerischen Methoden noch nicht, elektronische und nukleare Freiheitsgrade effizient zu koppeln, sodass die experimentell beobachtete Vibrationsperiode nicht bestätigt werden kann.

[2] transl.: ‘pump’ = aufpumpen (hier: anregen), ‘probe’ = untersuchen

[3] engl.: Self-Amplified Spontaneous Emission (SASE)

[4] engl.: ‘Split-and-Delay Unit’ (SDU)

Contents

Introduction

Intramolecular charge migration plays a key role in photochemical reactions of bio-relevant molecules. Specific examples include radiation damages [5, 6], molecular electronics [7] and photosynthesis[5] [9–11], to name a few.

Quantum coherences mediating charge migration are formed and defined by the coherent superposition of several quantum mechanical eigenstates. The most stable and experimentally easiest detectable coherences are formed by a pure two-state system. For most molecules, this requires a coherent, narrow spectral bandwidth excitation source, in order to selectively excite the two-state system[6]. The period of the charge migration is defined by the energy difference between the two states. The detailed calculation will be shown in Section 1.4.7, but smaller energy level gaps lead to longer periods. So far studied examples are on timescales of ∼100 as [12] to 20 fs, corresponding to ∼40 eV to 0.2 eV bands. In most cases the charge migration is initiated through prompt photoionization leaving behind a hole state. The correlated motion of electrons then leads to the hole localizing at a particular site, where a subsequent photoionization, for example, may result in bond breakage. Thus, quantum coherences increase the speed and efficiency of electron or hole migration to the reaction centers, but it is possible for them to decohere due to coupling of electronic with nuclear degrees of freedom. Pure electronic quantum wave packet dynamics are usually named 'charge migration', while dynamics involving nuclear degrees of freedom are referred to as 'charge transfer' [13]. The charge migration is required to be ultrafast to traverse to the reaction site before electronic to nuclear coupling destroys the coherence [7]. If the coherences are preserved for multiple oscillation periods the efficiency of photochemical reactions is increased even further, since it is given additional occasions for the reaction with each full period after the initial charge migration. Of course, if the wave packets are coherently coupled to trap states, the efficiency decreases [14]. Therefore, it is imperative to precisely control the temporal and spectral phase of the radiation in photochemical control protocols.

The main question that needs to be answered is: How robust and long-lived can electronic coherences be? Further questions that are left open are: When do nuclear degrees of freedom come into play in the charge migration process? And can the charge migrations be directed, i.e., a specific reaction site be selected?

Time-resolved electron spectroscopy is a powerful tool to study the development and phase-resolved dynamics in molecules with element specificity and orbital selectivity. Here, both electron and ion spectroscopy are employed in conjunction to fully comprehend the complete

[5] Both charge migration and charge transfer, i.e., the coupling of electronic and nuclear degrees of freedom, play crucial roles in photosynthesis. The exact nature of this process is still a topic of debate [8].

[6] Nonetheless, a broad bandwidth can be used to coherently couple multiple states at once and still initiate charge migrations, but it will be experimentally more difficult to isolate and identify the respective contribution of each orbital.

picture. In the first step (pump), the neutral molecule *in vacuo* is ionized by a soft x-ray photon, initiating the correlated motion of electrons. In the second step (probe), after a variable time delay, the fate of the electronic and possible nuclear motion is inquired through a second photoionization and collection of the ionization products. By repeating this two-step measurement for various time delays a complete motion picture of the electron dynamics can be acquired. The pulse lengths of pump and probe are required to be significantly shorter than the studied charge migration time period and the temporal delay between the two pulses needs to be well-characterized. Isolating the studied molecules in the gas phase allows for the measurement of intrinsic properties free from environmental effects and consequently better comparability with theoretical computations [12].

In this work, glycine was chosen as the example study case. Glycine is a molecule of biological relevance as it is an abundant basic building block of proteins and plays part in the recognition sites on cell membranes and enzymes [15]. Stand-alone, it is utilized as an inhibiting neurotransmitter in the central nervous system [16]. Glycine has also been found in space [17, 18] and is therefore a first signature of extraterrestrial life.

Yet it is small enough with only 40 electrons in 20 molecular orbitals forming a closed-shell system in its ground state, which facilitates computational simulations. As such it has been studied by Brion *et al.* [19, 20], Cederbaum *et al.* [21] and Marangos *et al.* [22, 23], to only name a few. For example, Marangos *et al.* [23, (2014)] predict a ∼20 fs oscillatory charge migration based on a level splitting of the calculated inner-valence 10a′ molecular orbital spectral lines, which can be initiated *via* prompt ionization and probed by Auger electron yield measurements.

Other bio-relevant molecules have been extensively studied, both experimentally and theoretically, in recent years. Examples are the XUV[7]-pump/VIS[8]-NIR[9]-probe experiments on phenylalanine [24] or XUV-pump/NIR-probe experiments on tryptophan [25] by Calegari *et al.* which exhibit charge migration with a period of 4.3 fs and 4 fs, respectively.

The main part of this thesis is structured as follows:

The first chapter will guide the reader through the generation of the highly coherent high-intensity soft x-ray radiation used in the experiment, highlight the intricacies involved, when it comes to x-ray-matter interaction for the used optics and demonstrate the splitting of a single light pulse into two pulse replicas with full relative phase control. Afterward, the interaction of molecules with ionizing radiation and the studied glycine sample will be introduced. Finally, the diagnostics for determination of the kinetic energy of the electrons and mass-to-charge ratio of the ions after ionization, as well as a method for keeping track of the pump-probe delay are presented.

[7]XUV = extreme ultra-violet
[8]VIS = visible light
[9]NIR = near infra-red

The second chapter follows up on the topics of the first chapter by appending experiment specific details, methods and parameters. In particular, the all-reflective split-and-delay unit will be fully characterized.
The third chapter presents the experimental results from two measurement campaigns and compares them with *ab initio* simulations. First, the photon energy dependent electron spectra at zero pump-probe delay will be shown. Second, the pump-probe delay dependent relative yield variations will be analyzed. These represent a measure for the electronic coherence, which is preserved for at least 25 fs. Following, the pump-probe delay scanning range is increased to up to 175 fs and photoion-photoion coincidences, photoelectron-photoelectron coincidences and photoelectron-photoelectron-photoion correlations are evaluated. Lastly, the kinematically complete analysis shows a decay of the electronic coherence by coupling to nuclear vibrations after about 45 fs.

1 Theoretical framework

This chapter introduces the theoretical basis necessary to understand the generation of two identical ultra-short soft x-ray pulses, as well as their interaction with the molecule glycine. A brief description of one method for the collection of the ionization products and determination of their kinetic energy is also presented. Dynamic information from the collected data is derived using a continuous wavelet transform, which will be introduced at the end of this chapter.

Probing electron dynamics, which happen on a sub-10 fs timescale, requires even shorter light pulses. Modern x-ray synchrotron sources, while having strongly collimated beams with high intensity and great stability and tunability, only offer minimum pulse durations of tens of picoseconds [26, p. vii–viii]. Free-electron lasers, on the contrary, offer pulse lengths from over 50 fs as low as sub-1 fs [27]. Moreover, the peak brightness is increased by 10 orders of magnitude [26, p. viii] compared to synchrotron light sources.

1.1 Free-electron laser

Free-electron lasers (FELs) accelerate electrons to relativistic velocities in radiofrequency (RF) cavities and then send them through undulators to convert part of the electrons' energy into very intense, coherent light waves with low divergence.
The following section only elucidates the basic FEL principles relevant to this work. Novel FEL schemes such as harmonic lasing [28] or seeded FEL operation [29] will not be covered.

First, a pulsed ultra-violet (UV) photoinjector laser emits evenly spaced out bunches of N_e electrons from a semiconductor photocathode [30] by means of the photoelectric effect. The free electron bunches are then accelerated by superconducting RF cavities toward ultra-relativistic velocities ($E_\mathrm{kin} \sim 1\,\mathrm{GeV}$) and regularly compressed *via* chicanes before entering the undulator. After the undulator around 0.01 to 0.1% of the electron beam energy has been converted into light [31] and the electrons are deflected into a beam dump.

1.1.1 The undulator

An undulator consists of multiple alternating magnetic fields with the maximum field strength B_0. The longitudinal distance between two closest aligned sections determines the undulator period λ_u. Combined, these sections form the periodic magnetic field component B_y in the vertical direction $\vec{e}_y$ on the central horizontal plane ($y = 0$), sketched in Figure 1.

$$B_y = B_0 \sin\left(\frac{\lambda_\mathrm{u}}{2\pi} z\right) \tag{1}$$

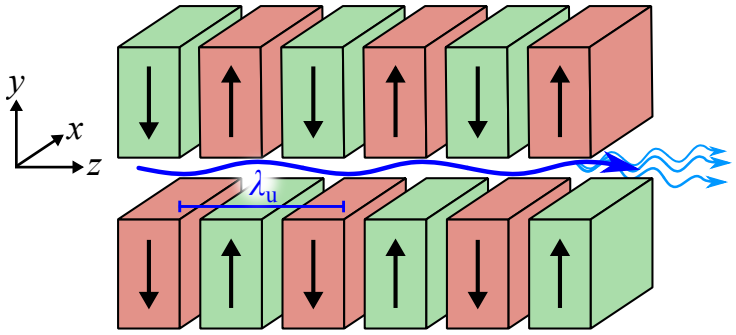

Figure 1: Scheme of an undulator. An electron beam (dark blue) is undergoing a sinusoidal motion in the alternating magnetic field of the undulator with period λ_u emitting x-rays (light blue) of wavelength λ_ℓ. The lateral deflection is exaggerated and typically in the µm range [32].

A charge with relativistic speed v, $\gamma = \dfrac{1}{\sqrt{1-\beta^2}}$, $\beta = \dfrac{v}{c}$ and c being the speed of light in vacuum, moving through the magnetic fields experiences an alternating Lorentz force and carries out a sinusoidal motion around the central axis. Synchrotron radiation photons are emitted in a narrow cone with opening angle $\theta_{\text{cone}} = \dfrac{1}{\gamma}$ around the electron trajectory, which itself has the maximum opening angle $\theta \coloneqq \theta_{\text{tang,max}} \approx \dfrac{K}{\beta\gamma} \approx \dfrac{K}{\gamma}$ [32]. K is the dimensionless undulator parameter [32] with the elemental charge e and the mass m_e of an electron.

$$K = \frac{\lambda_u e B_0}{2\pi m_e c} \tag{2}$$

Longer magnet sections ($\propto \lambda_u$) or larger magnetic field strengths result in stronger deflection of the electrons. Sufficient overlap of the emitted radiation along the undulator axis is guaranteed if $\theta \overset{!}{\leq} \theta_{\text{cone}} \Rightarrow K \overset{!}{\leq} 1$. This gives the undulator condition for constructive interference and forming a monochromatic spectrum. The fundamental wavelength of such radiation is given by the undulator equation [32]:

$$\lambda_\ell \cong \frac{\lambda_u}{2\gamma^2}\left(1 + \frac{K^2}{2} + \gamma^2\theta^2\right). \tag{3}$$

Since $\gamma \gg 1$ for relativistic particles it follows that $\lambda_\ell \ll \lambda_u$. Assuming a fixed undulator period the radiation wavelength can be continuously tuned by changing the electrons energy $W = \gamma m_e c^2$ [32] or changing the magnetic field strength by either using variable gap undulators with permanent magnets or constant gap undulators with electromagnets. The polarization of the light is in the horizontal plane when the gap of the undulator is oriented vertically.

When the electrons are distributed uniformly in the undulator, each electron emits undulator radiation with a random phase and the intensity I of the radiation scales linear with the number of electrons, $I \propto N_e$ [33]. This is called spontaneous emission.

1.1.2 Self-amplified spontaneous emission

Charge density fluctuations on the scale of $\sqrt{N_e}$ [34], which are called 'shot noise', in the electron bunch lead to enhanced radiation with similar phases. As soon as the first coherent light waves are randomly formed, these interact with the electrons, taking energy from the electrons in phase with the light wave and giving energy to electrons where the phase is opposite [31], thus creating electron microbunches with an intermediate distance of λ_ℓ. The formation of microbunches and generation of coherent radiation amplify each other exponentially. This is termed the 'high gain regime'. At the FEL power saturation the microbunches are fully formed and the net energy transfer is zero or slightly oscillating around zero. The average longitudinal length scale on which the microbunches are evenly spaced [35] (without phase jumps) is called coherence length L_{coh} with an equivalent coherence time $\tau_{\mathrm{coh}} \simeq cL_{\mathrm{coh}}$ [35]. Each electron bunch of total duration T_{bunch} can have multiple Fourier-limited modes, also called 'spikes', with individual intensities. The number of spikes M is given by:

$$M \approx \frac{T_{\mathrm{bunch}}}{\tau_{\mathrm{coh}}}. \tag{4}$$

As the bunches become more compressed, i.e., shorter in length and time, during the high gain regime, the number of modes (spikes) decreases. Due to the statistical nature of the self-amplified spontaneous emission (SASE) generation the intensity of each single spike in the intensity profile fluctuates on a scale of 100% [35]. The overall SASE intensity scales with the product of the total number of electrons N_e in the bunch and the number of electrons within one coherence length N_{coh} [35].

$$I_{\mathrm{SASE}} \propto N_e N_{\mathrm{coh}}. \tag{5}$$

1.1.3 Single-mode SASE

In order to obtain an even narrower bandwidth pulse, a single mode could be filtered out after the undulator using a monochromator, at the expense of intensity and beam orbit stability. Alternatively, the modulation of the electrons could be seeded by an external laser. Such a seed laser would need a high enough intensity to overcome the shot noise and also be tunable for all target FEL wavelengths.

Single-spike operation can also be achieved by using a photoinjector with reduced pulse duration and limiting the bunch charge to facilitate the bunch compression and decrease the bunch length to coherence length ratio in equation (4). For example, having a photoinjector pulse duration of 1 ps instead of 6.5 ps and bunch charges of 55 pC instead of 1 nC it has been demonstrated at FLASH that on average 1.5 spikes with Fourier limited pulse durations of (2.4 ± 0.2) fs are possible at a wavelength of 7 nm [36].

Other purely theoretical approaches include imprinting of the initial density modulation of the electrons already during their creation or having an energy modulation present in the electron

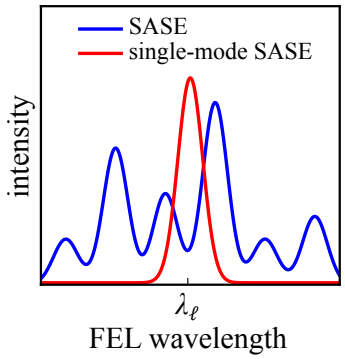

Figure 2: Contrived spectra of the SASE (blue) and ideal single-mode SASE (red) process.

beam [32, p. 66-67]. Both of these methods rely on being able to induce modulations with periods in the range of 10 to 500 as for generation of XUV radiation.

1.1.4 High power gain FEL

The power gain length L_g is defined by the length over which the FEL power in the undulator increases by a factor of $e \approx 2.72$ [37] in the exponential gain regime. The exponential gain regime starts after the first ~4 gain lengths [32, p. 66] and saturation is usually obtained after 10 to 20 gain lengths [32, 33]. At saturation, the power is periodically exchanged back and forth between the electrons and the light wave [32, p. 69].

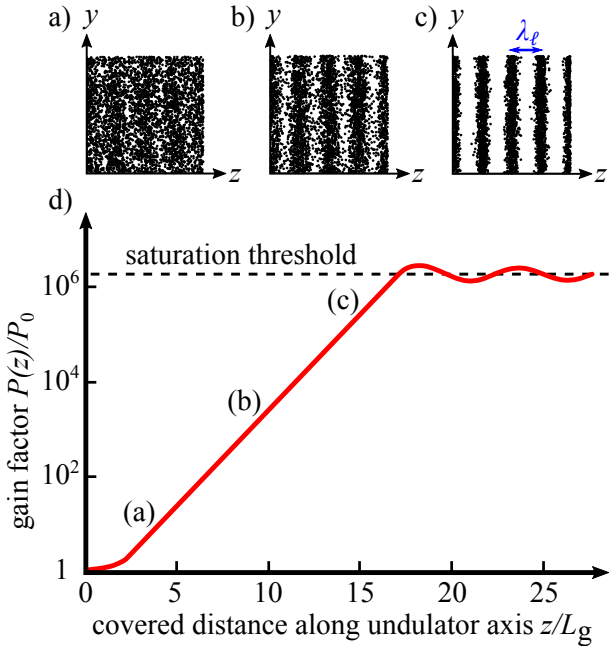

Figure 3: **a)-c)** Formation of microbunches during their excursion through the FEL undulator (stylized). **d)** FEL power gain in the spontaneous emission, high gain and saturation regime. The gain length L_g describes the distance by which the power increases by a factor of e in the high gain regime. The oscillation amplitude around the saturation threshold is exaggerated. Adopted from [32].

1.2 X-ray optics

Vacuum ultra-violet (VUV), extreme ultra-violet (XUV) and soft x-ray radiation have a high absorptance in materials and thus optical devices cannot rely on transmissive optical elements. They require an alternative approach using grazing incidence reflection or multilayer mirros.

1.2.1 Grazing incidence

The refractive index n of materials for x-rays is smaller than unity defined by the correction factors δ and β, which are dependent on material properties [38] and both scale quadratically with the wavelength λ. These dimensionless factors are on the order of 10^{-4} to 10^{-2} for soft x-rays and 10^{-6} to 10^{-5} for hard x-rays [39].

$$n = 1 - \delta - i\beta \tag{6}$$

The critical grazing incidence angle α_c below which the radiation only evanescently enters the material and is thereby totally externally reflected is defined by [39]:

$$\sin \alpha_c \approx \sqrt{2\delta} \tag{7}$$

Equation (7) is derived from Snells's law by setting the angle between the mirror surface and the refracted beam to zero. Additionally, the small angle approximation $\sin \alpha_c \approx \alpha_c$ can be applied, since $\alpha_c \ll 1$.

When the mirror surface exhibits some surface roughness σ measured as the root-mean-square (rms), part of the reflected intensity I_r is lost to diffuse reflection plus the diffuse rays may additionally decrease the specular intensity I_{sp} due to destructive interference. Furthermore, the specular intensity I_{sp} decreases for shallower grazing incidence angles α and also for shorter wavelengths [40].

$$I_{sp} = I_r \cdot \exp\left(-\left(\frac{4\pi\sigma \sin\alpha}{\lambda}\right)^2\right) \tag{8}$$

1.2.2 Toroidal mirrors

Toroidal mirrors use two different perpendicular surface curvatures with radii r_{tan} and r_{sag} to focus light hitting the mirror on the tangential and sagittal plane toward the focal points F_{tan} and F_{sag}, respectively. By choosing the correct ratio between r_{tan} and r_{sag} for a given grazing incidence angle α, the two focal lengths can be matched $f_{tan} \stackrel{!}{=} f_{sag} =: f$. This only works for the point on the mirror surface, where the tangential and sagittal planes meet and in approximation works best for incidence light beams close to the center of the mirror.
An incoming collimated beam can be expressed by setting the source point S to infinity. In that

case the image point S' lies at the focal point F. Inversely, placing S at F results in a collimated beam after the toroidal mirror.
The relation between the above parameters is specified by the Coddington equations [41]:

$$\frac{1}{s} + \frac{1}{s'_{\text{sag}}} = \frac{2\sin\alpha}{r_{\text{sag}}} = \frac{1}{f_{\text{sag}}} \tag{9a}$$

$$\frac{1}{s} + \frac{1}{s'_{\text{tan}}} = \frac{2}{r_{\text{tan}}\sin\alpha} = \frac{1}{f_{\text{tan}}}. \tag{9b}$$

Here s and s' denote the always positive distances between the image points S and S' and the mirror center and f the focal length to the focal point F.

The ratio of the two radii r_{tan} and r_{sag} of the toroidal mirror can be specifically chosen such that the tangential and sagittal foci coincide for a specific design angle α and thus preventing astigmatism.

$$f_{\text{tan}} \stackrel{!}{=} f_{\text{sag}} \quad \Rightarrow \quad \frac{r_{\text{tan}}}{r_{\text{sag}}} \stackrel{!}{=} \frac{1}{\sin^2\alpha} \tag{10}$$

The overall focal length $f_{\text{tan}} \stackrel{!}{=} f_{\text{sag}} =: f$ can be chosen through the absolute values of the radii during manufacturing.

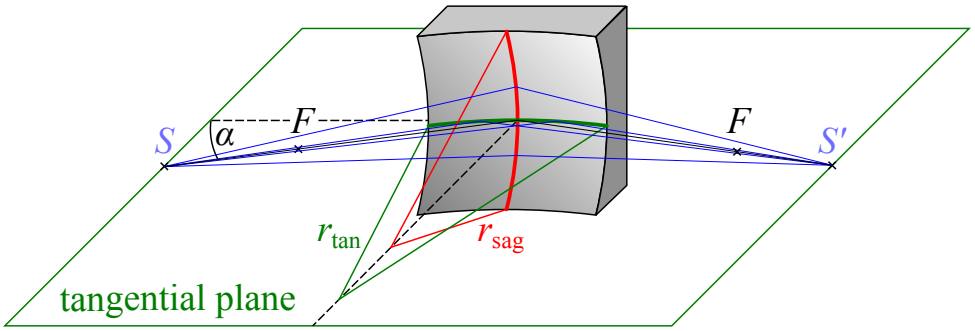

Figure 4: Incoming light from the source S under incidence angle α is reflected and focused toward S'. The two radii r_{tan} and r_{sag} of the toroidal mirror are chosen such that $f_{\text{tan}} \stackrel{!}{=} f_{\text{sag}} =: f$ for a specific grazing angle α.

1.3 Pump-probe spectroscopy

Complementary to spectroscopic studies, where the matter response is monitored as a function of photon energy after light-matter interaction, electron kinetic energy spectroscopy uses a monochromatic source and characterizes the likelihood of electron creation as a function of their kinetic energy. The obtained energy spectrum is characteristic for specific molecules. Furthermore, mass-to-charge spectra of simultaneously generated ions can be recorded equivalently.
Pump-probe spectroscopy yields time-resolved spectral information by first exciting a molecule using a pump pulse and, after an adjustable time delay Δt, inquiring the temporal evolution of

the involved molecular states by using a probe pulse.
Given the absence of beam splitters in the VUV and soft x-ray range, splitting one pulse into two time-delayed monochromatic pulse replicas (pump and probe) can be achieved by two split half-mirrors with a relative longitudinal displacement d. The two beams then need to be re-overlapped under an angle ϑ in the focus, which also results in tilted wavefronts and averaging of their relative phase in the focal volume.
Alternatively, using two interleaved reflective gratings naturally produces two collinear pulses. Figure 5 shows the retardation of one half of a beam regardless of half-mirror or grating-mirror assembly.

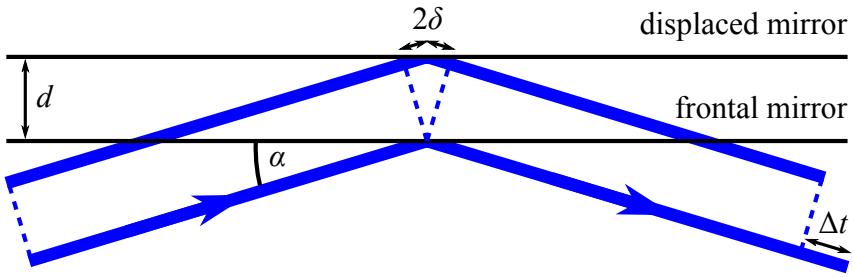

Figure 5: Incoming light under incidence angle α is partially reflected by the frontal mirror and to equal parts by the displaced mirror. Relative displacement d between the two mirror surfaces leads to a path difference of 2δ and time delay Δt. The displacement is greatly exaggerated compared to the beam diameter.

For the arrangement shown in Figure 5 the time delay Δt is dependent upon the displacement d and incidence angle α.

$$\Delta t = \frac{2d \sin \alpha}{c} \tag{11}$$

with c the speed of light in vacuum.

1.3.1 Diffraction grating

A collimated, highly coherent electromagnetic wave with wavelength λ incident on either a reflective or transmissive lattice grating with grating period g results in diffraction orders n under the angles φ_n. Equation 12 states the Bragg condition for constructive interference behind the grating [42][10].

$$\varphi_n = \arcsin\left(\frac{n\lambda}{g}\right), \quad n = 0, \pm 1, \pm 2, \ldots \tag{12}$$

For short wavelengths $\lambda < 10\,\text{nm}$ and relatively large lattice constants $g \approx 250\,\mu\text{m}$ the angle between two adjacent orders is smaller than $3\,\text{m}^\circ$.
When only a finite number N of grating lamellas with width b is illuminated, additional side orders are present between the main orders. Subsequently, the intensity of the main orders is decreased, but their amount and diffraction angles are preserved.

[10]The angle definition has later been redefined by W. L. Bragg to the here presented commonly used form.

In the special case of two interleaved gratings with the same lattice constant g that can also move relative to each other, the odd orders periodically disappear. When both gratings are coplanar, they have an effective grating period of $g/2$. Thus, the odd orders corresponding to grating period g interfere destructively and the actual visible orders are spaced twice as far apart as in the case of a singular grating. At longitudinal displacements d of multiples of the wavelength the odd orders disappear.

1.4 Molecular Physics

The following sections focus specifically on the interaction of light and matter and the properties of glycine. In the end the theoretical description of the pump-probe experiment will be discussed.

1.4.1 Photoexcitation

A photon with sufficient energy can elevate an electron from an atom or molecule into an excited state. If the photon's energy is higher than the orbital dependent binding energy of the electron, the electron can be emitted from the atom or molecule into the continuum. The kinetic energy E_{kin} of this photoelectron (PE) corresponds to the initial photon energy reduced by the electron's binding energy (BE) E_{b}.

$$E_{\mathrm{kin,PE}} = E_{\mathrm{ph}} - E_{\mathrm{b}} \tag{13}$$

The BE of the remaining electrons is progressively increased with the ionization level of the atom or molecule, due to less screening.

1.4.2 Rydberg states

Similar to the quantized energy levels E_n of an H atom, whole molecules exhibit these energy levels too, with

$$E_n = -\frac{R_\infty}{(n-\mu)^2}. \tag{14}$$

$R_\infty \approx 13.6\,\mathrm{eV}$ is the Rydberg constant, n is the principal quantum number and μ quantifies the deviance from the simple hydrogen example [43]. High level states with $n > 100$ require very little ionization energy and are nearly degenerate. The interaction of soft x-rays with molecules, which leads to the generation of ions and free electrons also leads to possible population of Rydberg states [44].

1.4.3 Auger decay

After an x-ray induced inner-shell photoionization in an atom, an electron from a higher orbital can fill the inner-shell hole and thereby 'fall down' from a higher energy level to a lower one. If the excess energy is high enough to induce a subsequent ionization, a so called 'Auger electron' will be emitted. The kinetic energy of the Auger electron (AE) is solely dependent on the energy

difference between the involved orbitals (compare Figure 6b) and equation (15)). The initial photon energy only establishes a threshold of the possible Auger decays.

$$E_{\mathrm{kin,AE}} = \Delta E - E_{\mathrm{b,AE}} \tag{15}$$

Since an atom has many possible Auger decay channels, which are labeled by their involved orbitals (e.g., L_3-$M_{2,3}M_{2,3}$)[11] the Auger spectrum consists of many close lying lines, which are distinctive for that particular atom.
The time between the initial photoelectron and the Auger electron emission is in the sub- to few-fs regime [45]. The Auger decay lifetime is slightly shorter [45].

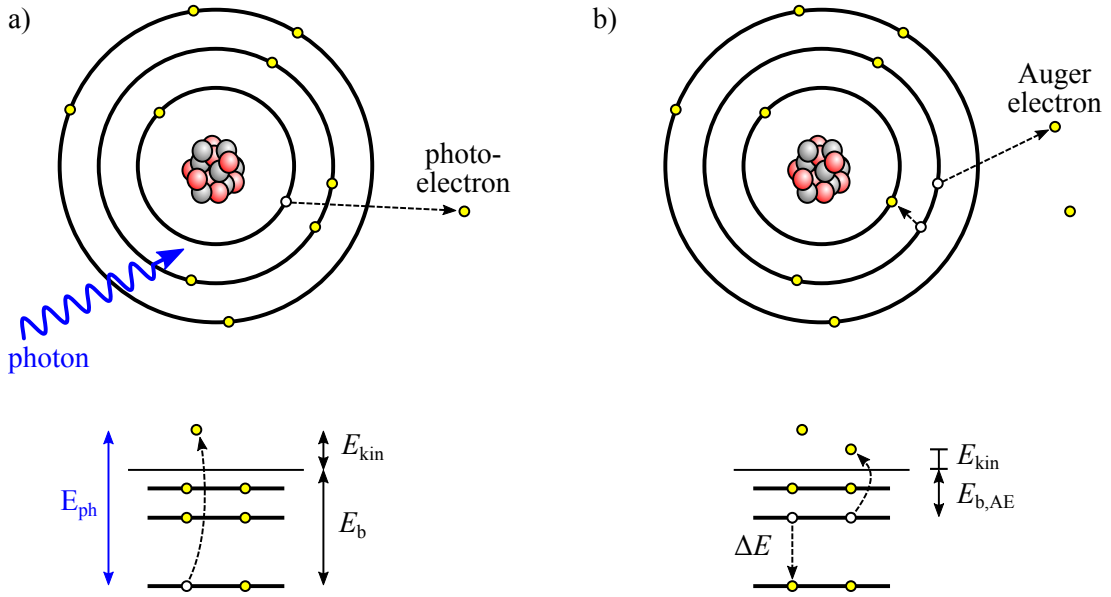

Figure 6: Principles of photoionization **(a)** and subsequent Auger decay **(b)**. Full description in the main text.

1.4.4 Double photoionization

If two valence photoionizations happen sequentially on the same molecule, the final two-hole (2h) dicationic state with two unbound continuum electrons is similar to that from Auger decay. In the special case, when the kinetic energy of such electrons happens to overlap with that of Auger electrons, the two processes become virtually indistinguishable by their end products. The photoelectron spectrum of the second photoelectron is generally shifted by the difference between the first and second ionization potentials but may also cover the extends of the single ionization spectrum due to ionization of high-lying Rydberg states of the cation.
In addition to the former sequential double photoionization (SDI) process, single-photon double photoionization (SPDI) is also possible. In a quasi-classical picture, a photon can only be absorbed by one electron but simultaneous ejection of a second photoelectron may occur if

[11] Specifically, L_3-M_2M_3 describes the internal transition $M_2 \rightarrow L_3$ and emission from the M_3 orbital.

energy is transferred through the correlated motion of the electrons. The cross-section of this high-order process can be ∼5 times or up to four orders of magnitude lower than that of direct photoionization [46, 47] depending on the photon energy and binding energies of the molecule. The amount of energy shared and thus the splitting ratio of the electrons' kinetic energies is a complex problem and varies from interaction to interaction. Whether the secondary electron is ejected through a shake-up or knockout mechanism is still subject of active research [46].

1.4.5 Quantum coherences

The concept of quantum coherence bases on treating electrons and holes as wave-like (with the de Broglie wavelength $\lambda_e = \frac{hc}{E}$ [48] and Planck's constant h). When traveling through a molecule, these particle waves can loose their temporal coherence by interaction with other electrons or nuclei. Electronic decoherence is expected during ∼10 fs [49]. Vibrational timescales for small molecules such as glycine are generally in the range of 10 to 100 fs for particular bonds and partial groups and up to 1 ps for intramolecular vibrations [50]. Rotations of small moieties around bonds are carried out on timescales of 100 to 350 ps [51]. All of these nuclear motions can lead to electronic decoherence.
New observable states are formed through the superposition of two or many single quantum states. Contrary to a mixture of systems in different states, systems with superpositions of said states will generally exhibit time dependent behavior [14]. Accordingly, the creation of a coherent superposition of states needs to happen in phase and thus requires ultra-short light pulses.

1.4.6 Density functional theory and algebraic diagrammatic construction

The later experimental results will be compared to *ab initio* simulations. This section will give a brief, simplified introduction of the methods and approximations used to facilitate calculations of excitonic correlations of complicated many-body systems.

In principle, every molecule can be modeled fully quantum mechanically by a set of interdependent Schrödinger equations. However, the computational effort of exact diagonalization of the Hamiltonian to derive the eigenvalues of the system scales exponentially with the number of particles N. Exact calculations including both electrons and nuclei have been performed for 4 electrons coupled to 2 vibrational modes [49, (status as of 2018)].
Instead, density functional theory (DFT) can be applied where nuclei are treated as motionless within the frame of the Born-Oppenheimer approximation and the electrons only experience a constant external field from the nuclei. Most essentially, electron-electron interaction is reduced to single electron interaction with a collective cloud of electrons with density ρ in the Hartree approach. Since every single electron is also part of this electron density an *Ansatz* for the wave function is used to solve the self-consistent equation for each electron, called 'Hartree equations'.

The antisymmetry condition for fermions is resolved through use of a Slater determinant. The wave functionals in these Hartree equations are then iterated until the energy of the system is minimized, giving the ground state of the system.
Furthermore, interaction corrections can be added at the expense of increased computational effort. Thus, the number of free parameters scales on the order of N^3 to N^7 [52]. Open-shell molecules require even more computationally expensive algorithms.

While time-dependent DFT has been developed to study dynamics of excited many-body systems, the calculations are either computationally very expensive or the applied electron-electron interaction approximations are not reliable enough [53], especially for doubly excited states or charge migration [54], for example initiated *via* sudden x-ray ionization. Alternatively, algebraic diagrammatic construction (ADC) can predict time-dependent density fluctuations based on perturbation theory with the second-order ADC(2) method being widely adopted due to reliable accuracy at reasonable computational effort [54]. For this, the polarization propagator, which contains the transition amplitudes, acts on the known[12] ground state by perturbing its electron density and describing the time-dependent propagation of the density fluctuations for each state in the many-body system [54]. Thus, a complete set of correlated excited states is obtained, which can be represented as a matrix with each matrix element describing the degree of quantum electronic coherence between two respective states.

1.4.7 Time-dependent two-state systems

The two-state model usually describes the repeated absorption and stimulated emission in an atom with a ground and excited state in a periodic electric field such as a laser. In the present charge migration study, instead a charge is merely brought into the two-state system beforehand by means of photon absorption. Afterward, the two-state model is used to characterize the periodic charge density oscillation within the molecule [55].

In the case of two eigenstates $|\psi_1\rangle$ and $|\psi_2\rangle$ with eigenenergies E_1 and E_2 and unperturbed stationary Hamiltonian $\hat{H}_0 = \begin{pmatrix} E_1 & 0 \\ 0 & E_2 \end{pmatrix}$ the time-dependent two level quantum state $|\Psi(t)\rangle$ can be expressed as a linear combination of the eigenstates [55].

$$\begin{aligned} |\Psi(t)\rangle &= c_1(t)\ |\psi_1\rangle + c_2(t)\ |\psi_2\rangle \\ &= \frac{1}{\sqrt{2}} \left(e^{-iE_1 t/\hbar}\ |\psi_1\rangle + e^{-iE_2 t/\hbar}\ |\psi_2\rangle \right) \end{aligned} \tag{16}$$

Equation (16) fulfills the time-dependent Schrödinger equation $\hat{H}_0 |\Psi(t)\rangle = i\hbar \frac{\partial}{\partial t} |\Psi(t)\rangle$ and boundary condition $|c_1(t)|^2 + |c_2(t)|^2 = 1$. For simplicity, it is assumed that both states will be

[12] For example calculated using DFT with enhanced accuracy.

equally likely to populate: $|c_1(t)|^2 = |c_2(t)|^2 = \frac{1}{2}$.

Transitions between $|\psi_1\rangle$ and $|\psi_2\rangle$ are modeled by $\hat{H} = \hat{H}_0 + \hat{H}_1 = \begin{pmatrix} E_1 & \kappa \\ \kappa^* & E_2 \end{pmatrix}$ with the coupling barrier κ.

In this coupled system $|\psi_1\rangle$ and $|\psi_2\rangle$ are no longer eigenstates. Instead two new eigenstates[13] $|\psi_\alpha\rangle$ and $|\psi_\beta\rangle$ are formed from the linear combination of $|\psi_1\rangle$ and $|\psi_2\rangle$.

$$|\psi_\alpha\rangle = \frac{1}{\sqrt{2}}(|\psi_1\rangle + |\psi_2\rangle) \qquad (17a) \qquad |\psi_1\rangle = \frac{1}{\sqrt{2}}(|\psi_\alpha\rangle + |\psi_\beta\rangle) \qquad (18a)$$

$$|\psi_\beta\rangle = \frac{1}{\sqrt{2}}(|\psi_1\rangle - |\psi_2\rangle) \qquad (17b) \qquad |\psi_2\rangle = \frac{1}{\sqrt{2}}(|\psi_\alpha\rangle - |\psi_\beta\rangle) \qquad (18b)$$

Substituting $|\psi_1\rangle$ and $|\psi_2\rangle$ in equation (16) with equations (18a) and (18b) gives:

$$\begin{aligned} |\Psi(t)\rangle &= \frac{1}{2}\left[e^{-iE_1t/\hbar}\ \left(|\psi_\alpha\rangle + |\psi_\beta\rangle\right) + e^{-iE_2t/\hbar}\ \left(|\psi_\alpha\rangle - |\psi_\beta\rangle\right)\right] \\ &= \frac{1}{2}\left[\left(e^{-iE_1t/\hbar} + e^{-iE_2t/\hbar}\right)|\psi_\alpha\rangle + \left(e^{-iE_1t/\hbar} - e^{-iE_2t/\hbar}\right)|\psi_\beta\rangle\right] \\ &=: c_\alpha(t)\,|\psi_\alpha\rangle + c_\beta(t)\,|\psi_\beta\rangle\,. \end{aligned} \qquad (19)$$

The probability of finding the particle in state $|\psi_\alpha\rangle$ is $P_\alpha(t) = |c_\alpha(t)|^2 = \cos^2\left(\frac{|E_1 - E_2|}{2\hbar}t\right)$ and for $|\psi_\beta\rangle$ it is $P_\beta(t) = |c_\beta(t)|^2 = \sin^2\left(\frac{|E_1 - E_2|}{2\hbar}t\right)$.

The oscillation period T with the Planck constant $h \approx 4.14\,\text{eV fs}$ [57] is purely dependent on the level splitting ΔE.

$$T = \frac{h}{|E_1 - E_2|} = \frac{h}{\Delta E} \qquad (20)$$

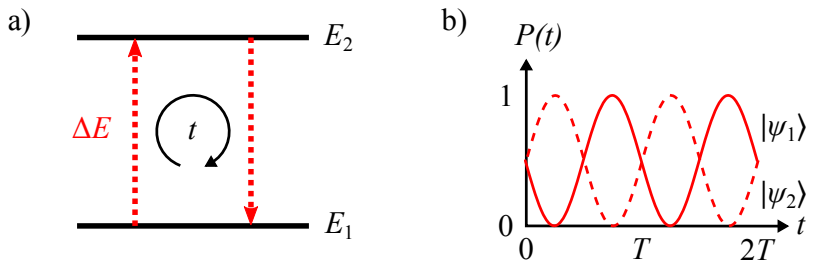

Figure 7: Resonant particle migration in-between a two-state system of eigenstates $|\psi_1\rangle$ and $|\psi_2\rangle$ with eigenenergies E_1 and E_2. The oscillation period of the probability that either state $|\psi_1\rangle$ or $|\psi_2\rangle$ is populated is given by $T = \frac{h}{\Delta E}$. $\left(|c_1(t)|^2 = |c_2(t)|^2 = \frac{1}{2}\right)$

[13] Diagonalization of $\hat{H}$ gives the two new eigenenergies $E_{\alpha,\beta} = \frac{1}{2}\left(E_1 + E_2 \pm \sqrt{(E_1 - E_2)^2 + 4|\kappa|^2}\right)$ [56].

Figure 7b) shows the oscillatory probabilities $P_1(t)$ and $P_2(t)$ which have a phase offset of $\frac{T}{8}$ relative to $P_\alpha(t)$ and $P_\beta(t)$. One can see that the oscillation starts at $|\Psi(t=0)\rangle = |\psi_\alpha\rangle$ the equipollent superposition of $|\psi_1\rangle$ and $|\psi_2\rangle$.
Figure 7 shows the coherent, resonant case with equal probabilities $\left(|c_1(t)|^2 = |c_2(t)|^2 = \frac{1}{2}\right)$. Unequal c_n cause a bias in the two probability amplitudes.
In case of incoherent evolution of the two-state system or dephasing due to collisions the probability oscillations are damped [58].

1.4.8 Electronic-vibrational coupling

In a complex molecule, the potential energy curves are not necessarily constant as presented in the previous section. Keep in mind, that the previous theoretical description also works for two harmonic potential wells separated by the potential barrier κ. Traditionally, vibrational coupling between two energetically well-separated electronic states is governed by the Franck-Condon principle [59]. Electronic-vibrational, or 'vibronic', transitions are favored, when the probability of presence of the nuclei goes from one maxima to another, while the position and momentum of the slow nuclei (compared to the electrons) does not significantly change (see Figure 8a)). In this way, a transition between electronic states is often accompanied by a transition of vibrational states. Vibronic coupling, which results in a change of the internuclear distance is greatly enhanced in the vicinity of conical intersections or avoided crossings, depicted in Figure 8b). In this case, the Born-Oppenheimer approximation fails and the nuclear and electronic wave functions can no longer be separated. The molecule can no longer be correctly described by DFT.

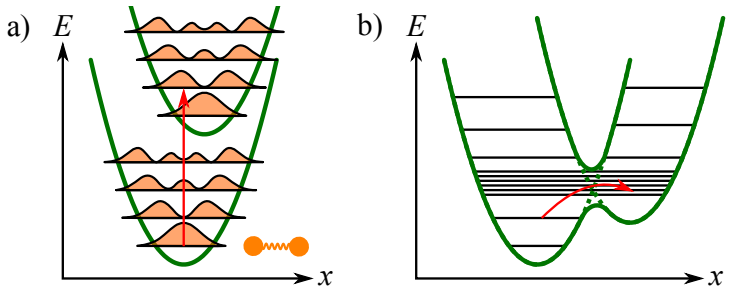

Figure 8: Electronic-vibrational coupling. For simplicity two identical harmonic potentials are stand-ins for more complicated curve shapes and only a selection of vibrational levels (black) are drawn. (In the case of diatomic molecules the potential energy curves are described by Morse potentials.)
a) Electronic excitation from a lower to a higher energy state based on the Franck-Condon principle. Vibronic transitions, which do not change the internuclear distance x, are favored (vertical arrow). The position dependent probability of presence of the atom cores is featured in orange for the first four vibrational levels [60].
b) In the vicinity of a conical intersection (green, dashed) or avoided crossings (green, solid) the coupling of nuclear vibrations to electronic states is greatly enhanced. An electronic excitation leads more easily to a change of the internuclear distance.

In a three dimensional molecule the potential energy of the system is represented by potential energy surfaces (PES) instead of curves.

1.4.9 Amino acids

Amino acids are the basic building blocks of proteins and thereby play a key role in the understanding of processes in life sciences on the molecular level. Proteins have manifold functions in both flora and fauna including ion transport, catalysis of biochemical reactions, transport of smaller compounds and many others [61].
Amino acids contain an amino group ($-NH_2$, $-NR_2$), the acidic carboxyl group ($-COOH$), the central C_α atom and a side chain ($-R$). Depending on at which C atom of the side chain the amino group is located, the amino acid is distinguished as an $(\alpha, \beta, \gamma, ...)$-amino acid. Multiple amino acids of various types can link together by substituting the hydroxyl ($-OH$) with the amino group of the next amino acid through elimination of one H_2O molecule. Oligomers and polymers comprising of up to 50 or 100 amino acids are usually labeled as peptides, while polymers with lengths above 100 are called proteins [62, 63]. The exact threshold number of linked amino acids to form proteins is fluid. There are 20 canonically naturally occurring proteinogenic and more than a hundred non-proteinogenic amino acids [63].

1.4.10 Glycine

Glycine (Gly) is the simplest amino acid with its side chain comprising only one H atom. Due to its compact nature and tendencies to form hydrogen bonds it facilitates the coiling of proteins and is therefore incorporated frequently in hydrophobic protein helices[14], where it reduces helix packing voids and sets the orientation of "multiple helices in a folded protein complex" [64]. Stand-alone, it is utilized as an inhibiting neurotransmitter in the central nervous system [16].

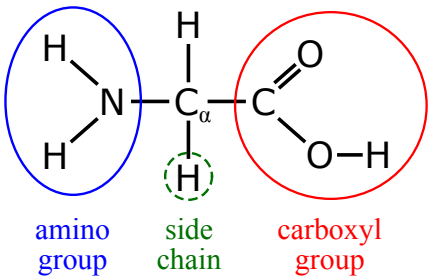

Figure 9: Structural formula of the simplest α-amino acid glycine.

Glycine has 40 valence electrons occupying 20 closed-shell molecular orbitals (MOs) for which the first 17 binding energies are listed in Table 1. The LUMO is 5a″. The notations a′ and a″ denote in- and out-of-plane orbitals. a′ orbitals can comprise of σ and/or π symmetry MOs,

[14] At the same time it is also the cause of the breaking of helices in water-soluble proteins due to the augmented hydrogen bonds with water molecules [64].

whereas a″ only comprises of π symmetry MOs. The first and second ionization potentials (IP) of glycine are 10 and 22 eV, respectively. As such, the double ionization potential (DIP) is 32 eV [22].

Orbital	BE
16a′ (n_N) (HOMO)	10.0[1]
15a′ (n_O)	11.1[1]
4a″ (π_{OO})	12.2[1]
3a″	13.6[1]
14a′	14.4[1]
13a′	15.0[1]
2a″	15.6[1]
12a′	16.6[1]
11a′	16.9[1]

(cont.)

Orbital	BE
1a″	17.6[1]
10a′ (C_α 2s)	20.2[1]
9a′ (C 2s)	23.2[1]
8a′ (N 2s)	28.3[2]
7a′ (O_C 2s)	32.3[2]
6a′ (O_H 2s)	34.3[2]
5a′ (C_α 1s)	292.5[3]
4a′ (C 1s)	295.0[3]

Table 1: Binding energies (BE) of glycine orbitals (conformer Gly I) in eV ([1][65]; [2][66]; [3][23]). a′ and a″ denote different orbital orientations (in-plane and out-of-plane). The shown experimental data might differ from theoretical calculations by up to 1 eV. O_C belongs to the carbonyl group (C=O), while O_H belongs to the carboxyl group (C–OH)

In aqueous solution the molecule may exist as a zwitterion while gaseous it has its canonical neutral form [66]. Glycine evaporates above ∼80°C with noticeable vapor pressures above ∼135°C [67] and dissociation above ∼230°C [68]. There are eight glycine conformers: Gly I–VIII with ever increasing enthalpies. Below 100 K only Gly I is present [69], while with increasing temperature the higher energy conformers become accessible. Calculated abundances between 137°C and 165°C are, rounded to full integers, 41–55% for Gly I, 9–24% for Gly II, 6–35% for Gly III and 7–15% for Gly IV. The rest are below 3% combined ([70] and references therein [19, 20, 71]). The binding energies given in Table 1 slightly vary for different conformers. For details the interested reader is referred to reference [72].

Predominant stretching modes of the neutral glycine have found to be the C–C bond with 41.7 fs, C–O with 30.3 fs and C=O with 18.7 fs periods [73, (514.5 nm excitation in Ar matrix)]. The X–H stretching periods range from 9.4 to 11.3 fs with moderate to weak intensities. C–N stretching plus C–C vibrations correspond to 32.2 fs [74]. Further C–C stretching modes exhibit periods of 24.1 fs [73] and 26.4 fs [75]. Other publications report 23.9 to 25.1 fs for the C–C stretch and 35.7 to 40.9 fs for the C–C stretch including NH_2 wagging [76, (exp. solid glycine)], [77, (calc. gaseous glycine)].

Upon photoionization of the glycine molecule the covalent bonds suffering electron deficiency may break. In the case of doubly charged glycine the two positive charges can be distributed equally (1:1) or unequally (0:2) on the fragmentation products, dependent on homo- or heterolytic bond fission and location of the second charge. The newly created cations or dications may

dissociate further. Neutral fragments remain intact and also cannot be detected in this work. The whole fragmentation sequence happens on a timescale of a few hundred fs [78]. The most abundant ionization fragments of Gly^{2+} are found in Table 2.

m/q	Fragment
1	H^+
2	H_2^+
12	C^+
13	CH^+
14	N^+, CH_2^+
16	O^+, NH_2^+
17	OH^+

(cont.)

m/q	Fragment
18	H_2O^+
27	CNH^+
28	N_2^+, CO^+, CNH_2^+
28.5	CH_2NHCO^{2+}
29	COH^+, CNH_3^+
29.5	$CH_2NH_2COH^{2+}$

(cont.)

m/q	Fragment
30	$[CH_2–NH_2]^+$
32	O_2^+
42	$C_2OH_2^+$, $C_2NH_4^+$
44	CO_2^+
45	CO_2H^+
46	$HCOOH^+$, $(OH)_2C^+$
57	CH_2NHCO^+

Table 2: Cationic ionization fragments of glycine. The mass-to-charge ratio m/q is given in units of u/e. Reproduced from [78], which studies the "fragmentation patterns of glycine dications that are created by the Auger decay process of [C 1s] core vacancies," which has similarities to the present study.

Itälä *et al.* [78] found the most common fragmentation pathway of Gly^{2+} to be cleavage of the C–C bond creating $CH_2NH_2^+$ and $COOH^+$, followed by further fragmentation into the cations found in Table 2 or neutral species thereof. Another fragmentation pathway is the elimination of a neutral (rarer cationic) water molecule especially when there exists a hydrogen bond between the amino and hydroxyl group.

1.4.11 Theoretical expectations of the single-color soft x-ray pump-probe experiment

The purpose of the pump-probe experiment is to ionize the glycine molecule and initiate a coherent charge migration throughout the molecule driven by a level splitting in the 10a′ MO. Following, the evolution of the underlying coherent superposition of states will be determined by the probe pulse at different time delays Δt.

The pump pulse with a central energy of 273 eV ionizes the glycine molecule, marking $\Delta t = 0$. The kinetic energy of the outgoing photoelectron gives conclusion about the involved molecular orbitals. Here, events featuring electrons with $E_{\text{kin}} \approx (253 \pm \Gamma_{\text{FEL}})$ eV, where Γ_{FEL} is the FEL's bandwidth, from the 10a′ orbital are of interest. A hole state in the inner-valence 10a′ orbital will undergo oscillatory charge migration according to Section 1.4.7 since it has a level splitting of $\Delta E \sim 0.2$ eV. The two distinct levels are both comprised of ~50% of a pure inner valence hole state (1h) and ~50% of a series of two-holes-one-particle (2h1p) configurations [23]. Based on

Section 1.4.7 the superposition of these states ψ_1 and ψ_2 can be described by:

$$|1h\rangle = \frac{1}{\sqrt{2}}(|\psi_1\rangle + |\psi_2\rangle) \tag{21}$$

$$|2h1p\rangle = \frac{1}{\sqrt{2}}(|\psi_1\rangle - |\psi_2\rangle) \tag{22}$$

Only the 1h state can be prepared through the initial photoionization, which ensures that all observed dynamics start with a common phase. The theoretical ionic degree of coherence between the two states is very high at ~95% and the predicted starting phase is $\varphi_0 = 0$. Higher energy level gaps lead to incoherent coupling by narrow pump-pulse bandwidths and vanishing coherence [79].

The 10a′ orbital spans nearly the full molecule (see Figure 10b)) and in consequence the transient local electron hole density moves to the same extent, thus making it an excellent candidate for the study of charge migration. The oscillation period T is expected to be in the range of ~20.7 fs based on equation (20). Since the glycine conformers have slightly different binding energies and their abundances are quite varied and cannot be determined with the experimental setup, some variation of the predicted period of around ±25% should be expected and must be evaluated from the experimental data. However, the measured effective oscillation period T will always be based on the mix of conformers present in the molecular beam [79]. Other theoretical calculations predict timescales varying from ~49 fs (Gly I) to 27 fs (Gly III) and 21 fs (Gly II) for the 1h state in the 10a′ molecular orbital (with involvement of additional orbitals) [21].

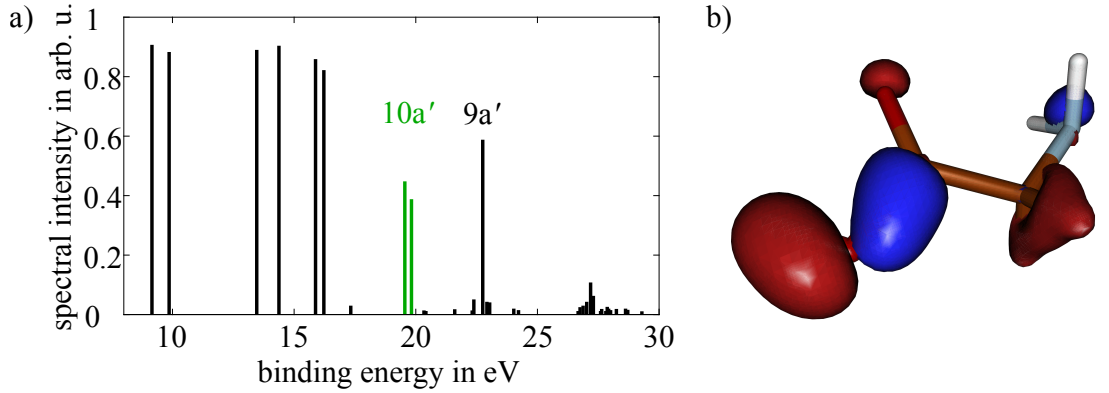

Figure 10: **a)** Calculated spectral intensities of glycine orbitals. The 10a′ orbital is split into two levels with an energy separation of ~0.2 eV. The calculated binding energies might differ from the experimentally obtained values given in Table 1 by 1 eV. Reproduced from [23].
b) Electron density isosurfaces of the glycine 10a′ inner-valence molecular orbital (blue and red lobes). The colors of the stick-model represent: C (orange), O (red), N (blue), H (white). ADC calculations performed and reproduction permission granted by Marco Ruberti, Imperial College London [23]

If the electronic wave packet survived until after the variable time delay Δt and the 1h state is localized in the vicinity of the C_α nucleus again, the 273 eV probe pulse can resonantly excite a C_α 1s electron into the 10a′ vacancy, allowing for subsequent Auger decay and emission of

an Auger electron. Note that the molecule has two C 1s orbitals, 4a′ and 5a′ with an energy difference of 2.9 eV, which is somewhat larger than the spectral bandwidth of the FEL, making a coherent superposition of these states in the resonant absorption process rather unlikely. Also note that the corresponding time period of 1.4 fs for the 2.9 eV energy difference lies beyond the present time resolution of the pump-probe experiment.
The measured yield of Auger electrons versus pulse delay will represent the oscillatory charge migration with time period T since the 5a′ $\rightarrow$ 10a′ transition will more likely occur the closer the transient hole is to the corresponding C_α atom. Alternatively, a second photoionization event can occur bearing a similar dication and same oscillatory electron yield. The kinetic energy range of the second photoelectron, generated in the sequential process, largely overlaps with that from Auger decay, as can be seen in Figure 37 of Section 3.1. The ratio between Auger decay and the sequential double ionization (SDI) contribution depends on the photon energy and will be discussed in detail in the results Section 3.3.

The C_α 1s orbital has a binding energy of 292.5 eV and is only accessible for resonant excitation by 273 eV photons, because of the resonant transition into the inner-valence 10a′ state of the molecular cation. The FEL photon energy is tuned in the range between 269 eV and 281 eV, which is specifically chosen to stay beneath the carbon K-edge (284.2 eV) as well as the nitrogen and oxygen K-edge (410 eV, 543 eV) [80, 81].
After a few hundred fs fragmentation of the doubly charged glycine is expected to set in [78]. There are many fragmentation pathways, as discussed above, predominantly lead by cleavage of the C–C_α bond, resulting in 2 to 7 fragments with CNH_n^+, $n = 1, ..., 4$ the most abundant [78].
The kinetic energy of the photoelectrons will be measured using a magnetic-bottle electron spectrometer, giving information about involved molecular orbitals. At the same time, the intact Gly^{2+} ions from the double ionization or the respective fragments can be distinguished using an ion time-of-flight mass spectrometer.

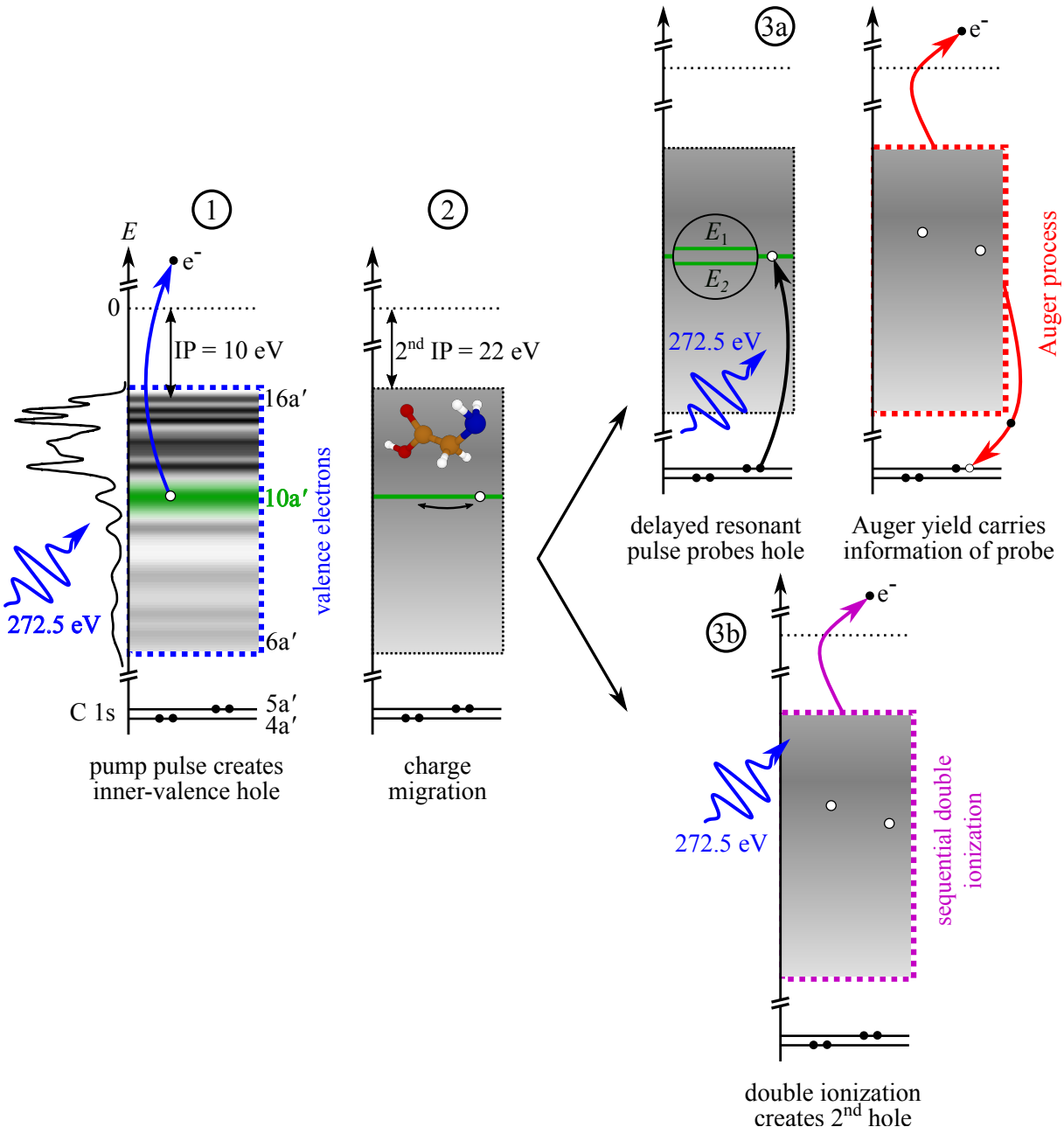

Figure 11: Excitation scheme for studying charge migration in glycine, leading toward the final two-hole (2h) state with 2 emitted electrons. For a more in-depth description please see the main text. Used with permission from [79].
(1) The density of states is given as both a shading of gray and spectrum with amplitude on the horizontal axis. Data obtained from [66].
(2) After the first ionization the binding energies are no longer the same as for the neutral molecule.
Steps (3a) and (3b) are mutually exclusive.

1.5 Magnetic-bottle electron spectrometer

A magnetic-bottle electron spectrometer (MBES) uses a cylindrically symmetric magnetic field to guide electrons, which are for example emitted by photoionization in the focus of the FEL, the interaction zone, toward a detector without altering their kinetic energy. Around the interaction zone, the density of the magnetic field is increased, forming a magnetic mirror, which reverts the velocity of electrons moving away from the detector. Furthermore, charged particles emitted in all directions within a flat double cone around the longitudinal z-axis of the magnetic-bottle can be collected. Due to the Lorentz force acting on charged particles in a homogenous magnetic field, the electrons carry out helical trajectory around a particular field line while being guided to the detector. Provided the magnetic field transitions adiabatically from the high intensity to the low intensity region, meaning the longitudinal field strength changes along z are negligible during one gyration period of a particle, it can be shown (for example by Goldston and Rutherford [82, p. 36–39]), that the electrons magnetic moment $\mu = \frac{m_e v_\perp^2}{2B}$ is invariant. From $\mu_i \equiv \mu(z)$, where the subscript 'i' denotes the value of the parameter in the interaction zone ($z = 0$), follows:

$$\frac{v_{\perp,i}^2}{B_i} = \frac{v_\perp^2(z)}{B(z)}. \tag{23}$$

A decrease of magnetic field strength is accompanied by a decrease of the perpendicular velocity and, since the total velocity $v^2(z) = v_\parallel^2(z) + v_\perp^2(z) \equiv v_i^2$ of the electron is constant, an increase of the parallel velocity component. Combining the two previous equations yields:

$$v_i^2 = v_\parallel^2(z) + v_{\perp,i}^2 \frac{B(z)}{B_i}. \tag{24}$$

For an electron traveling toward higher magnetic fields, there exists a maximum limit of $B(z)$, where $v_\parallel(z) = 0$ and the electron gets reflected. The velocity vector components can also be expressed by an angle θ with $v_{\perp,i} = v_i \sin\theta_i$ and inserted in equation (23) gives the maximum acceptance angle $\theta_{max,1}$ below the interaction zone and $\theta_{max,2}$ above it.

$$\theta_{max,1} = \arcsin\sqrt{\frac{B_i}{B_{max}}}, \qquad \theta_{max,2} = \arcsin\sqrt{\frac{B_{drift}}{B_i}} \tag{25}$$

Figure 12 visualizes the velocity components and the acceptance double cone defined by $\theta_{max,1}$ and $\theta_{max,2}$.

1.5.1 Time-of-flight to kinetic energy conversion

After the first few cm of flight, the electrons enter the electric field-free drift tube and the magnetic field no longer decreases. The parallel velocity is constant and dominant and the kinetic energy E_{kin} of an electron can be derived from measuring its time of flight (ToF) $(t - t_0)$ between the light pulse (creation time t_0 of the electron) and its arrival time t at the detector.

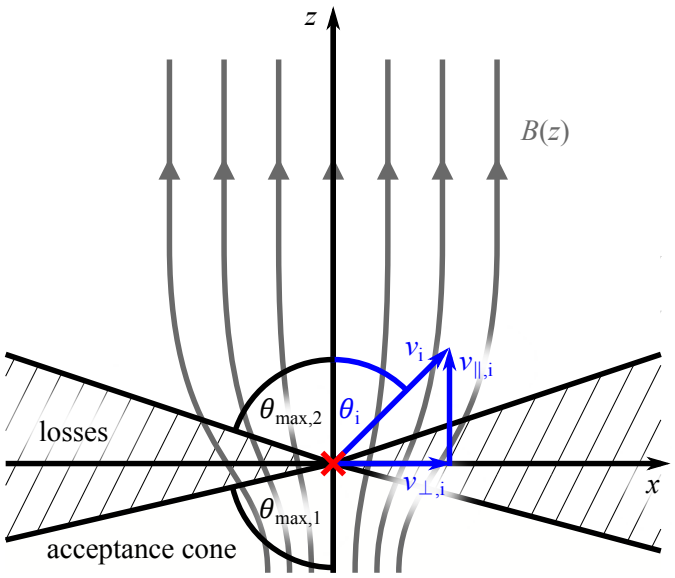

Figure 12: Scheme of a magnetic-bottle electron spectrometer visualizing the acceptance angles $\theta_{\mathrm{max},1}$ and $\theta_{\mathrm{max},2}$. The real-world case is rotationally symmetric around the z-axis. Electrons whose initial velocity vector v_i does not direct in the acceptance double cone below and above the interaction zone (red cross) cannot be collected. A possible electron flight path will be shown in Figure 33.

Equation (26) gives the first order relation between ToF and E_kin.

$$E_{\mathrm{kin,e}} = \frac{1}{2} m_\mathrm{e} \left(\frac{L}{t - t_0} \right)^2 - eU_\mathrm{ret} \tag{26}$$

L denotes the length of the flight path, so that $v_\parallel \simeq \dfrac{L}{t - t_0}$ is the electrons velocity. A negative retardation voltage U_ret can be applied to the first electrodes which discriminates slow electrons with less kinetic energy than $-eU_\mathrm{ret}$, thus increasing the energy resolution of high energy electrons.

1.5.2 Ion time-of-flight mass spectrometer

A ToF mass spectrometer uses static electric fields to accelerate charged particles toward the detector. The ions' mass-to-charge ratio m/q can be inferred from the ToF. Since the photoions are much heavier than the escaping photoelectrons the energy transfer to the ion is negligible and the ions start from rest[15]. The ions are accelerated toward the first extractor electrode with

[15]At 150°C an ideal gas particle has an average kinetic energy of ~55 meV, much smaller in comparison to the energy it will gain from the applied electric field. For a particle with 75 u this means an average velocity of 375 m/s compared to the $2 \cdot 10^4$ to $7 \cdot 10^4$ m/s after the acceleration and even higher for smaller or doubly charged ionization fragments.

applied voltage U_{ion} and than travel field free in the drift tube.

$$E_{\text{kin,ion}} = \frac{1}{2}m\left(\frac{L_{\text{ion}}}{t_{\text{ion}} - t_{0,\text{ion}}}\right)^2 = qU_{\text{ion}} \tag{27}$$

By reordering this equation the ToF can be converted to the mass-to-charge ratio m/q.
If more than one potential is applied instead of the field free drift tube, the travel path with individual electric fields can be split into sections. In the case of two sections L_1 and L_2 with potential differences U_1 and U_2 the equations of motion can be expressed as:

$$L_1 = \frac{1}{2}\frac{q}{m}\frac{U_1}{L_1}t_1^2 \tag{28}$$

$$L_2 = v_1 t_2 + \frac{1}{2}\frac{q}{m}\frac{U_2}{L_2}t_2^2 \tag{29}$$

with $L_{\text{ion}} = L_1 + L_2$ and $t_{\text{ion}} = t_1 + t_2$ and $v_1 = \sqrt{\frac{2qU_1}{m}}$ the velocity immediately after the first section. Solving for m/q yields:

$$\frac{m}{q} = \frac{(t_{\text{ion}} - t_{0,\text{ion}})^2}{\left(L_1\sqrt{\frac{2}{U_1}} - L_2\frac{\sqrt{2U_1}}{U_2} + \sqrt{2}L_2\sqrt{\frac{U_1}{U_2^2} + \frac{1}{U_2}}\right)^2}. \tag{30}$$

1.5.3 Jacobian coordinate transformation

The count rates $S(t)$ per time-of-flight bin can be converted to count rates $S'(E)$ per kinetic energy bin *via* the Jacobian coordinate transformation [83].

$$S'(E) = \left|\frac{\partial t}{\partial E}\right| \cdot S(t), \tag{31}$$

where $\left|\frac{\partial t}{\partial E}\right|$ is the Jacobian (determinant).

1.6 White-light interferometry

A Michelson-type interferometer uses a beam splitter to split a light beam, reflecting them from two different surfaces and combining them again after a second pass through the beam splitter. Depending on the relative path difference (within the coherence length of the light source) the wavefronts either interfere constructively or destructively.
If the overlapping wavefronts are slightly tilted, the interference pattern will appear as stripes of maximum and minimum intensity due to constructive or destructive interference at different lateral positions. Changing the path difference then shifts the stripes left or right instead of an extensive modulation in brightness. A relative displacement of the mirrors by $\frac{\lambda}{2}$ shifts the wavefronts by λ and results in a full 2π phase shift of the intensity modulation independent of

the applied tilt angle. Thus, relative movement of the two interference arms can be determined very precisely by monitoring the lateral location of the fringes.
The closer the overlapping wavefronts are to planarity the wider the stripes and the more precise the distance difference between the mirrors can be evaluated, however, the monitorable range decreases. The final relative displacement resolution limit also depends on the camera's pixel density and bit depth. It is not necessary to know the value of the skewing angle; only knowledge of the central wavelength is required.

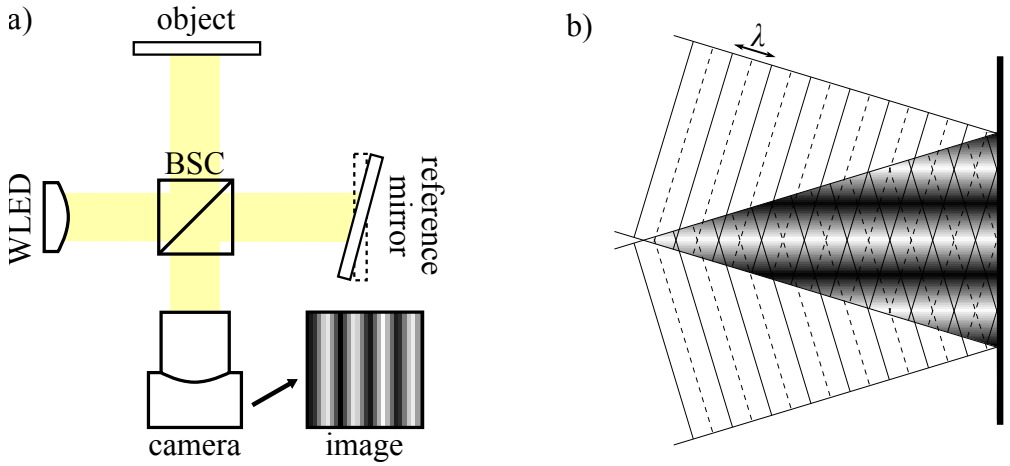

Figure 13: Schematics of a white-light interferometer (WLI) **(a)** and creation of interference fringes **(b)**.
a) A collimated beam from a white-light emitting diode (WLED) is split by a 50:50 beam splitting cube (BSC) and forming interference fringes upon overlapping of both reflected beams if the path difference of the two reflective surfaces is within the coherence length of the light source. Adapted with permission from [84].
b) Two light beams with wavefronts (maxima and minima as solid and dashed lines) overlapping under an angle result in constructive interference (white) or destructive interference (black).

In the present work, the WLI is also used to record extensive 'heightmaps', monitoring the surface topography of the lamellar mirror assembly. Steadily moving the reference mirror and recording the interference fringes with the camera produces an interferogram for each pixel. The relative height of the object at each pixel location is inferred from fitting the central position of each interferogram in relation to the known displacement of the reference mirror, thus mapping the surface profile of the object.

1.7 Continuous wavelet transform

The continuous wavelet transform will be used extensively in Section 3.5 in the analysis of time-dependent signals with multiple frequency components and variable amplitudes. In general, a wavelet analysis allows to study the amplitude evolution of a non-stationary signal at scaling frequencies [85].

A wavelet $\psi(t) = g(t)e^{i\omega t}$ is a modulated signal with frequency ω convoluted with an envelope $g(t)$ (see Figure 14a)). The classification and naming of wavelets refer to the shape of the envelope. The generalized Morse wavelets encompass a wide selection of wavelets by introducing the shaping parameters β and γ describing the width of the envelope in frequency and time domain. With $\gamma = 3$, so-called Airy wavelets, the most Gaussian-like envelope shape can be achieved, as well as the symmetry in frequency domain maximized. The generalized Morse wavelets $\Psi_{\beta,\gamma}(\omega)$ in frequency domain are given by [86]:

$$\Psi_{\beta,\gamma}(\omega) = \int_{-\infty}^{\infty} \psi_{\beta,\gamma}(t)\, e^{-i\omega t}\, dt \tag{32}$$

$$= H(\omega)\, c_{\beta,\gamma}\, \omega^{\beta} e^{-\omega^{\gamma}} \tag{33}$$

where $c_{\beta,\gamma}$ is a normalization constant and the Heaviside function $H(\omega)$ ensures that $\Psi_{\beta,\gamma}(\omega) = 0$ for $\omega < 0$.

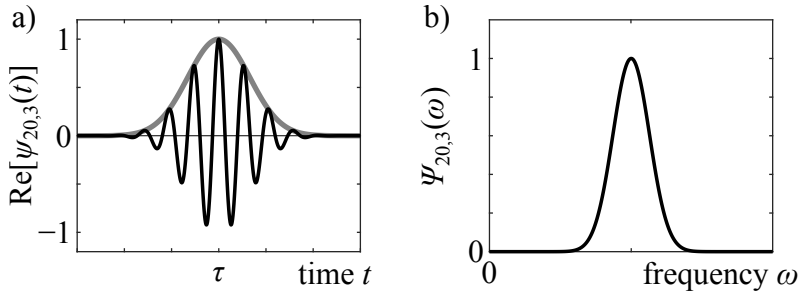

Figure 14: Normalized generalized Morse wavelet with $\beta = 20$ and $\gamma = 3$ in time domain **(a)** and frequency domain **(b)**. Only the real part is shown. The absolute value (i.e., modulus) of the wavelet function is given as a thicker gray line.

Introducing the time-bandwidth product $P^2_{\beta,\gamma} = \beta\gamma$ [86], the number of oscillations in Figure 14a) is $\frac{P_{20,3}}{\pi} \approx 2.5$.

The continuous wavelet transform (CWT) compares different wavelets $\psi(t)$ against the time-dependent signal $x(t)$ at specific times τ.

$$W_\psi(\tau, s) \equiv \int_{-\infty}^{\infty} \frac{1}{s}\,\psi^*\left(\frac{t-\tau}{s}\right) x(t)\,dt = \frac{1}{2\pi}\int_{-\infty}^{\infty} \Psi^*(s\omega)\,X(\omega)\,e^{i\omega\tau}\,d\omega \tag{34}$$

Here, s is a scaling parameter. When the wavelet stretches in time, its modulus is proportionally decreased and in frequency domain centered around the scaling frequency $s\omega$.
The time-frequency distribution $W_\psi(\tau, s)$ can be graphically represented as an intensity map which shows how well the wavelet matches for a given (τ, s). $|W_\psi(\tau, s)|^2$ represents the magnitude of the wavelet and signal at (τ, s) and is thus called 'magnitude scalogram'.

Computationally, s needs to be discretised[16] with the spacing between $s_{k\in\mathbb{N}}$ growing exponentially. The number of points within one doubling of s are referred to as 'voices per octave' v. This results in sampling scalings $s_k = 2^{k/v}$. Increasing the number of voices per octave improves the frequency resolution at the cost of increased computation time.

Furthermore, where part of the wavelet (in time domain) extends past the finite signal uncertainties arise. The boundary for the start of these uncertainties is called 'cone of influence' (COI). Here, the COI is chosen as the points where the autocorrelation magnitude of the respective wavelet decays by $\frac{1}{e}$ [88]. The COI is then also mirrored around the center of the signal.

[16]This must not be confused with the discrete wavelet transform (DWT) [87].

2 Experimental setup and parameters

The present chapter details the construction of the 'split-and-delay' unit, preparation of the grating-mirrors, design of the molecular beam source and calibration of the electron and ion spectrometers.

2.1 FLASH

The Free-Electron LASer in Hamburg (FLASH) at DESY started user operation in 2006 [30]. The electron source of FLASH uses a Cs_2Te photocathode. A UV photoinjector laser hitting the semiconductor photocathode under near normal incidence [30] generates electrons by means of the photoelectric effect. The electrons are then accelerated and directed by a $1\frac{1}{2}$ cell long normal conducting RF cavity, followed by further superconducting RF cavity accelerators and bunch compressor chicanes, which are alternating. Up to 800 electron bunches are grouped in a bunch train of around 1 ms total length with 1 µs spacing (or multiples of 1 µs if less bunches are used). The more exact FEL pulse repetition rate is 1003.086 kHz. The bunch trains can be split up to supply two experimental halls: FLASH1 and FLASH2. FLASH1 uses fixed-gap undulators with permanent magnets and relies on varying the electron energy for tuning the FEL wavelength. Whereas the wavelength provided at FLASH2 can be independently tuned by variable-gap undulators [89]. Both undulators produce linearly polarized light in the horizontal plane. Furthermore, each experimental hall contains multiple beamlines with different experimental setups ('end stations'), which are operated mutually exclusive.

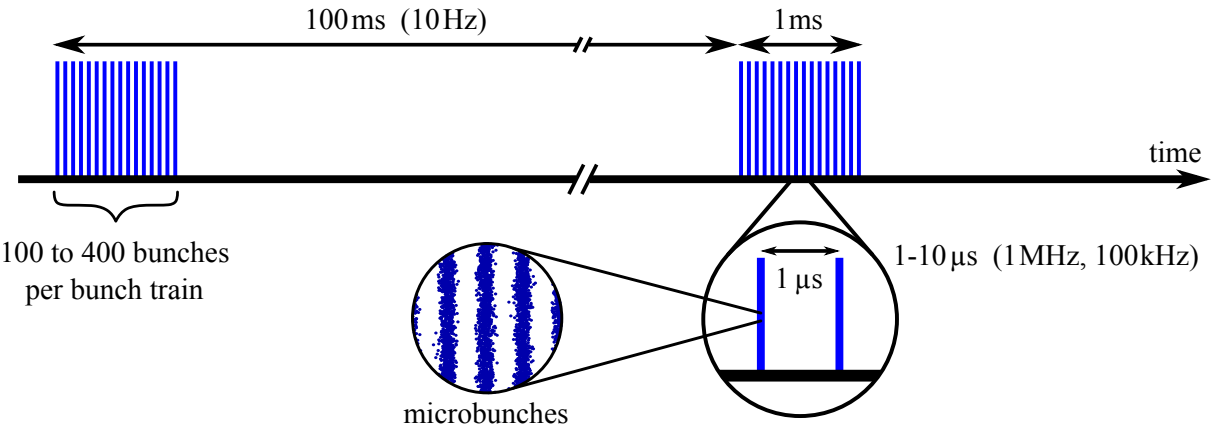

Figure 15: Electron bunch pattern at FLASH used in this work. Every bunch generates an FEL pulse.

Figure 15 shows the electron bunch pattern at FLASH. Every electron bunch of a bunch train generates a light pulse in the pulse train. The electron bunch charge was 70 pC in the 2018 experimental campaign and 50 pC in 2020, resulting in average FEL pulse energies of 3.6 and 0.9 µJ, respectively. The pulse energies are measured with non-invasive gas monitoring detectors (GMD) which count the number of ions generated in a low-density gas target on a

pulse-to-pulse basis with an accuracy of 10% [90].

Beamline FL24 is a beamline located in the FLASH2 experimental hall which (so far) does not offer a permanent end station. In the presented experiment the focusing Kirkpatrick-Baez mirrors are bypassed in order to obtain a nearly collimated FEL beam. The unfocused beam size is ~5 mm and can be limited by apertures (albeit creating Airy discs). A HeNe laser is used for a first alignment of the experimental user setup.

The provided analog-to-digital converters (ADCs) have a 2 Gsps sampling rate[17] and 12 bit dynamic range. All events of a complete FEL pulse train are recorded in one ADC trace or time-to-digital (TDC) time count ('sweep') started by the FEL trigger. The ADC/TDC signals are then resampled and split so that all light pulses align. All electrons and ion products are collected before the next light pulse arrives.

2.1.1 Online photoionization spectrometer

FLASH2 uses a non-invasive online photoionization spectrometer (OPIS) [91] to infer the FEL wavelength and beam orbit. Four electron ToF spectrometers arranged in a cross pattern detect the photoionization electrons from a low density noble gas target, such as Ar. By comparing the ToF difference of the same photolines of two opposite spectrometers the origin position can be calculated. The wavelength can be equally determined by comparing the absolute ToF of all spectrometers with calibration values. Shorter overall ToFs mean higher electron kinetic energies and photon energies. Both values include both the FEL bandwidth and the positional spread of the beam as an uncertainty. Usually the wavelength measurement is derived from spectra averaged over approximately 10 pulse trains. The pulse-to-pulse variation is likely higher.

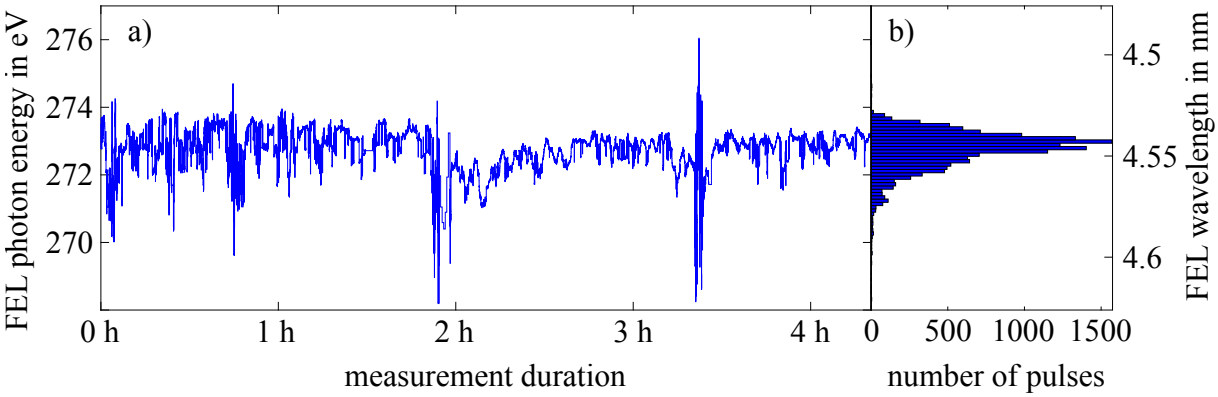

Figure 16: FLASH photon energy around a central energy of 272.7 eV (4.55 nm) over a time span of 4:15 hours **(a)** and histogram thereof **(b)**. The photon energy variation is (mostly) unrelated to the FEL bandwidth but appears as an additional energy spread in the integrated direct photoelectron spectra.

[17] sps = samples per second

2.1.2 FEL spectral bandwidth

A soft x-ray Gotthard spectrometer [92] developed at DESY in cooperation with the Paul Scherrer Institut (PSI) was placed behind the MBES. The Gotthard spectrometer has been successful in recording shot-to-shot SASE spectra at FLASH at $\lambda = 12.3$ nm [92]. However, due to the single-mode SASE intensity being around 50–300 times lower compared to the standard SASE operation, the final intensity after all optical elements was too low to deliver shot-to-shot spectra above the noise level, the average bandwidth had to be derived from the OPIS system.

Figure 17 shows two exemplary ionization events where the coincidence of two electrons from two different Ar atoms is detected in opposite ToF spectrometers in the OPIS. At the average photon energy and centered FEL beam position the Ar $2p_{1/2}$ photoelectron spectra will form a narrow peak at each of the dotted vertical lines, only blurred by the FEL bandwidth and beam diameter. Two further aspects widen these peaks: A non-centered FEL beam position leads to a reduced ToF measurement in one spectrometer and an increased one in the opposing spectrometer, here indicated by the red stars in Figure 17. On the other hand, a change of the FEL photon energy leads to a symmetric change of the ToF in both spectrometers, in this exemplary case, a decrease of photon energy, indicated by red crosses. Since these two cases happen simultaneously the positional jitter and beam diameter is intertwined with the spectral bandwidth and FEL photon energy fluctuations. By taking the difference of the two deviations from the average peak center, the FEL photon energy fluctuations can be eliminated from the spectral bandwidth. However, the positional jitter and beam diameter influence will still be included, therefore only an upper limit of the spectral bandwidth can be determined.

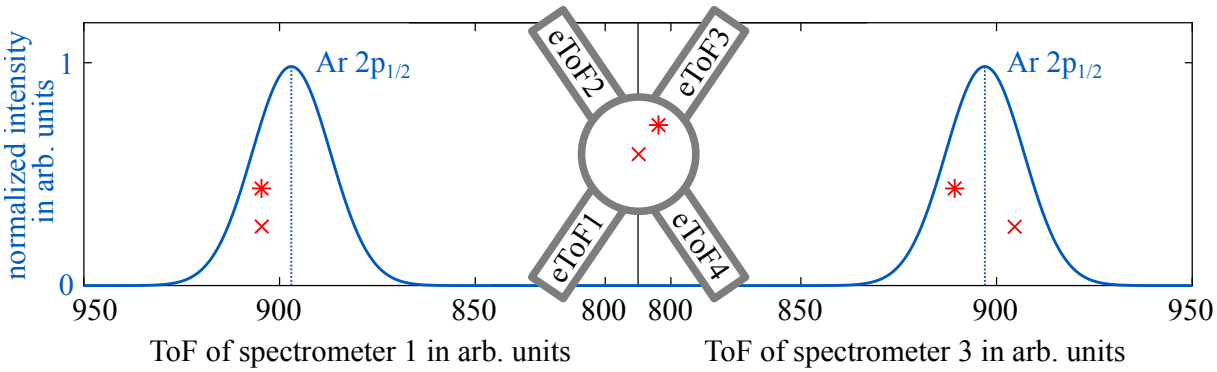

Figure 17: FLASH bandwidth estimation scheme using two opposite ToF spectrometers of OPIS. Two distinct event cases have been indicated by a red star and red cross. The center inset depicts a cross-section of the OPIS vacuum chamber with the four ToF spectrometers. The FEL beam propagates along the normal of the image plane.

Figure 18 shows such an upper limit of the spectral bandwidth where all four ToF spectrometers and the Ar $2p_{1/2}$ and $2p_{3/2}$ peak have been evaluated. No higher harmonics could be identified within the given energy resolution and range.

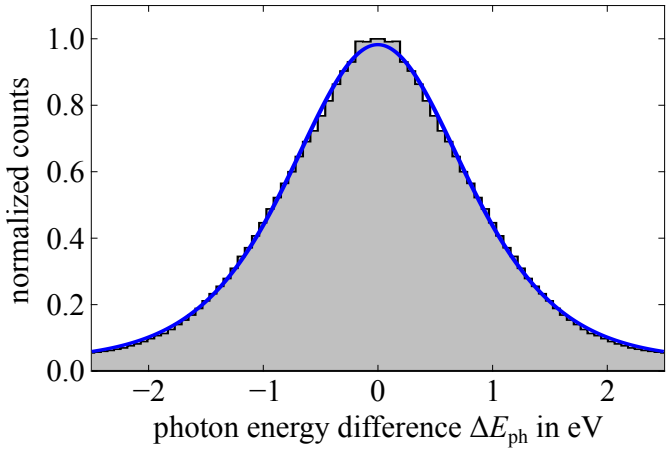

Figure 18: Spectral autocorrelation of the FLASH single-mode SASE spectrum. The energy spread of Ar $2p_{1/2}$ and $2p_{3/2}$ PEs in four ToF spectrometers gives an upper limit for the bandwidth Γ. A fitted sech^2 curve (blue) yields $\Gamma = 1.01\,\text{eV}$ around the central photon energy $E_{ph} = 274\,\text{eV}$. The histogram has been symmetrized around $\Delta E_{ph} = 0\,\text{eV}$.

A hyperbolic secant squared distribution of the form

$$f(\Delta E_{ph}) = a\ \text{sech}^2\left(\Delta E_{ph}/\Gamma\right) + c \tag{35}$$

with amplitude a, offset c, bandwidth Γ and time-bandwidth product of 0.315 was fitted to the spectrum. At $E_{ph} = 274\,\text{eV}$ the upper limit of $\Gamma = 1.01\,\text{eV}$ relates to a spectral width of 0.37% and, assuming a Fourier limited pulse, a pulse duration[18] of 1.28 fs. The in this way retrieved spectral bandwidth is in good agreement with previous measurements of single-mode SASE spectra at FLASH at $\lambda_{FEL} = 7\,\text{nm}$ ($E_{ph} = 177\,\text{eV}$) giving an upper limit bandwidth of 0.4% [36].

2.2 'Split-and-delay' unit

The self-built, all-reflective, 'split-and-delay' unit (SDU) is centered around two interleaved grating-mirrors. One of these mirrors is fixed, while the second one can be vertically and horizontally pivoted in order to planarly align the two. The mirror can also be linearly moved in the direction of the surface normal to enable the delay of one of the two pulse replicas and thereby facilitate time-resolved pump-probe experiments. A rotation of one or both of the mirrors around the surface normal axis is undesirable. Each of these three degrees of freedom (DoF) is controlled by a respective linear piezo actuator. The two rotational DoFs are realized *via* lever arms and torsion return springs. The movable pedestal of the horizontal rotation also rests on a polytetrafluoroethylene (Teflon®) mat for reduced friction.

The x-ray radiation is reflected under a fixed grazing incidence angle of $\alpha = 8°$. Though generally the reflectivity increases with shallower incidence, the width of the smaller of the two

[18]The pulse duration from the Fourier limit generally describes the lower limit. In this case, since ΔE_{ph} itself only defines an upper limit, the pulse duration can be slightly longer.

mirrors is 6 mm and the width of the reflected beam profile scales with $1/\sin\alpha$.
Another limiting geometric effect arises from the cardan suspension points for the rotation around the horizontal axis, which will cast shadows for shallower incidence angles or larger beam sizes. Spacing these suspension points further apart increases the load and weakens the structural rigidity of the setup and scales unfavorably with α. Figure 19 shows the normalized reflectivity R of the coplanar grating-mirrors. The convolution of the Ni reflectivity curve with the curve describing the geometric effects shows that the nominal 8° are a good compromise. The absolute reflectivity of the SDU when assuming perfectly flat grating-mirrors is around 25%. For the inclusion of surface roughness please refer to Section 2.2.3.

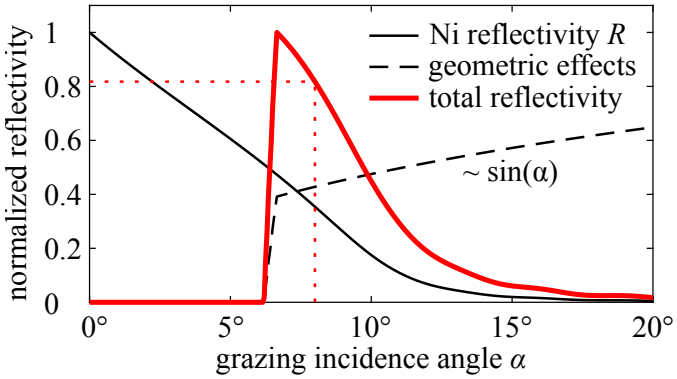

Figure 19: Simulated reflectivity of perfectly flat Ni coated mirrors under grazing incidence angle α including geometric effects for wavelength $\lambda = 4.5$ nm. A Gaussian beam with 3 mm FWHM beam diameter was used for the simulation. The Ni reflectivity curve is adapted from [93] and reference within [94].

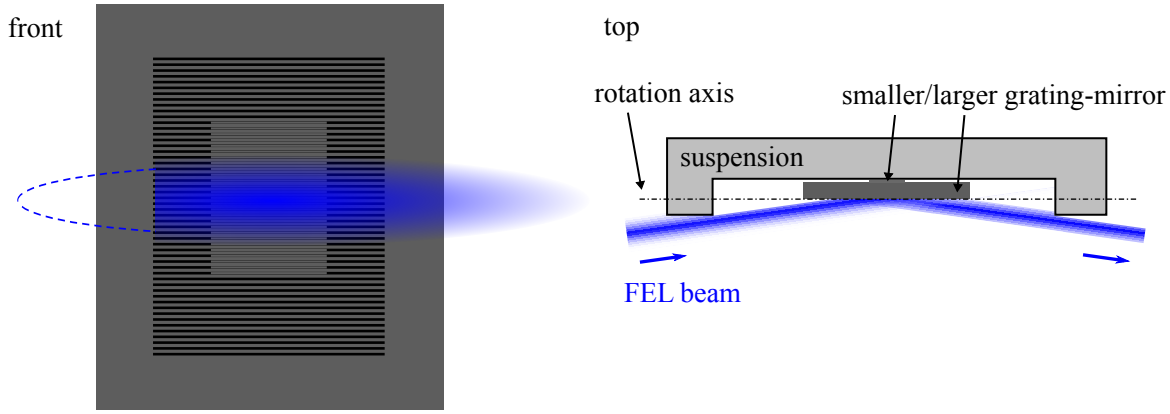

Figure 20: **front view:** FEL beam profile (blue) with a FWHM of 3 mm impinging on the grating-mirrors under grazing angle $\alpha = 8°$. The shadow on the left is cast by a cardan suspension point of the setup. The right side of the beam profile will be equally blocked after passing the second suspension point.
top view: The two-fold clipping of the incoming and reflected FEL beam can be seen. The majority of the small grating-mirror is occluded by the larger one at this viewing angle. Not to scale.

The aforementioned shadow casting also supports in getting closer to a 1:1 splitting ratio between

the two grating-mirrors by blocking the light beyond the extent of the lamellar grating. The beam profile is required to cover areas beyond the width of the smaller of the two grating mirrors at zero displacement to ensure sufficient coverage of the smaller grating mirror at non-zero lateral displacements.

The SDU performs its two name-giving actions in a single step, whereas more conventional pump-probe setups first split the pulse into two replicas, then delay the probe pulse *via* a chicane and afterward refocus the two beams. The present grating-based SDU requires only a single reflection of each beam path and permits truly collinear outgoing beams, maximizing the interference contrast. Compared to two-color SDU setups it offers many advantages, mainly significantly faster finding of time-zero and low time-delay jitter, while having ultrashort, narrowband high intensity x-ray pump/x-ray probe pulses.

Given the incidence angle $\alpha = 8°$ a lateral displacement of $d = 1\,\mu m$ between the two mirror surfaces relates to a pump-probe time delay $\Delta t = 0.9285\,fs$ according to equation (11). A hypothetical deviation from the nominal angle by $\pm 1°$ results in a systematic relative error of $\pm 12.4\%$. A precursor of the present SDU has been successfully used to generate pulse replicas with sub-cycle precision of light-waves with an oscillation period of 129 as [95].

Immediately after the SDU a Ce:YAG[19] screen can be moved into the beam path to inspect the footprint of the outgoing beam (see Appendix 5.1). The support frame for the vacuum chamber of the SDU stands on three air bearing feet, which allow for smooth translation and rotation around the entrance vacuum flange during the initial optics alignment. The SDU itself can be moved *in situ* along and perpendicular to the incoming beam axis by a xyz-stage with stepping motors and about 10 mm total range per coordinate. The focusing mirror vacuum chamber is also firmly mounted to the support frame. Figure 21 gives an overview of the experimental setup. The slits, oven and MBES will be discussed in the Sections 2.3, 2.4 and 2.5, respectively.

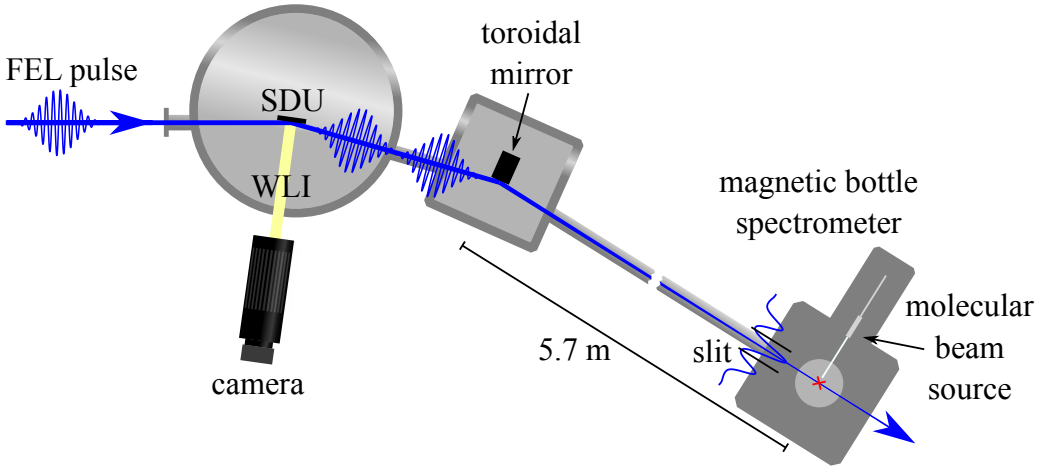

Figure 21: Overview of the experimental setup. The top-view of the vacuum chambers is to scale. The SDU grating-mirrors and the slit are enhanced. The support frames are not shown.

[19]Ce:YAG = cerium-doped yttrium aluminum garnet (Ce:$Y_3Al_5O_12$)

2.2.1 Grating-mirrors

The grooves of the grating-mirrors were sawn by Dr. Haunhorst in the group of Prof. Dr. Kip from the Helmut-Schmidt University, using a circular saw blade. The grating-mirrors have a grating period of 250 µm with 100 µm wide lamellas. The fill factor of each of the two interleaved gratings is 40%. The smaller of the two grating-mirrors is about 6 mm by 10.3 mm, determining the usable surface area (see Figure 22).

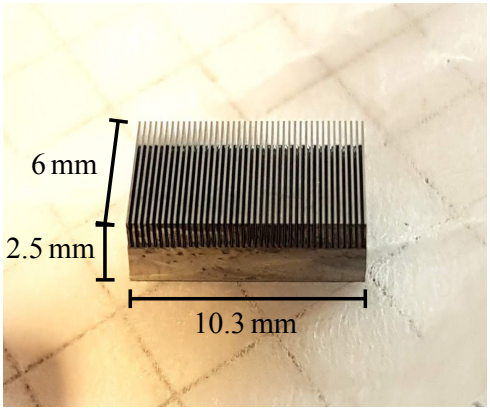

Figure 22: Annotated photograph of the smaller of the two grating-mirrors.

Before sawing, the Si mirror substrates from Pilz-Optics, albeit being only 2.5 and 3.5 mm thick, feature a high grade surface flatness with a radius of curvature of at least 5 km and a target value of 10 km. The roughness of both substrates is less than 0.5 nm rms. Excellent work and research has been performed by the collaborators to preserve the surface quality and keep chipping damage at a minimum. For the sawing process, prior grooves are filled with an adhesive, to prevent the lamellas from bending, breaking or twisting, which has to be removed afterward. Figure 23 shows the gratings before and after residue removal under a reflected light microscope. Different methods have been experimented with, ranging from overnight soaking in acetone or using a heated magnetic stirrer, followed by a quick bath in iosopropyl alcohol and delicate wiping. Acceptable results came down to numerous repetitions of delicate wiping while also bearing the largest risk of lamellas bending or breaking and micro scratches. Diminishing results were observed due to anew contamination of the surface with uprooted leftover adhesive from the grooves.

The Si grating-mirrors were then uniformly coated, using a sputter source [96] operated by Dr. Bocklage, with a 36 nm thick Ni layer for a 8 times increased x-ray reflectance compared to the bare Si substrate at the given grazing incidence angle and photon energy. An incidence angle dependent comparison between Ni and Si can be found in the Appendix 5.3. The backside of the less than 1 mm thick lamellas of the larger grating were coated identically to avoid bending caused by differing thermal expansion coefficients. For this a special holder has been designed, which ensures that all three to be coated surfaces are equidistant to the sputter source.

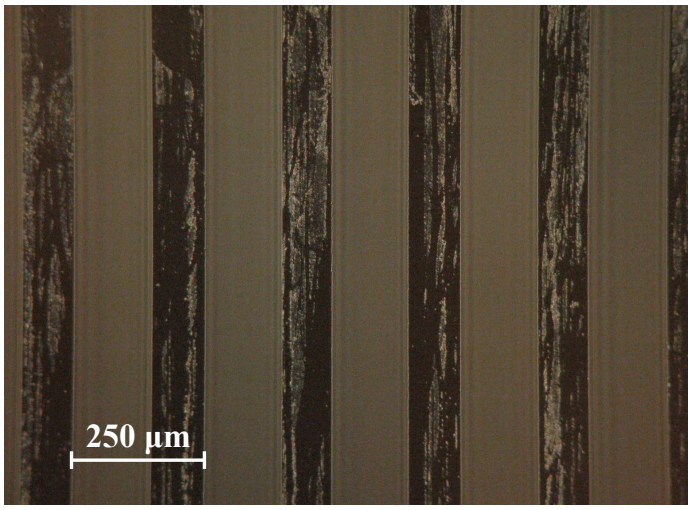

(a) The 100 µm wide lamellas of the grating-mirror are covered with adhesive residue from the sawing process (50× magnification).

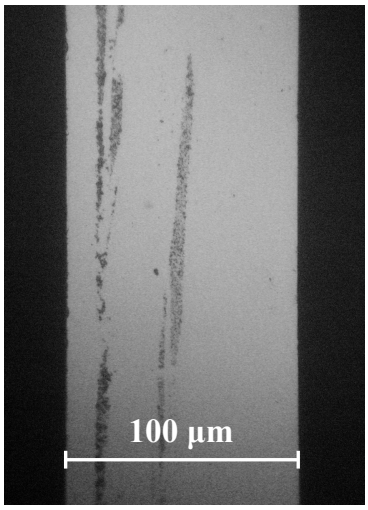

(b) A single lamella before cleaning (500×).

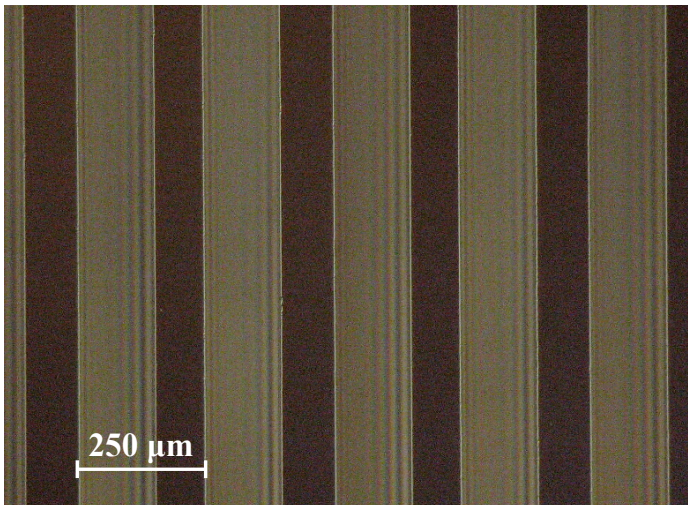

(c) The grating-mirror after cleaning (50×).

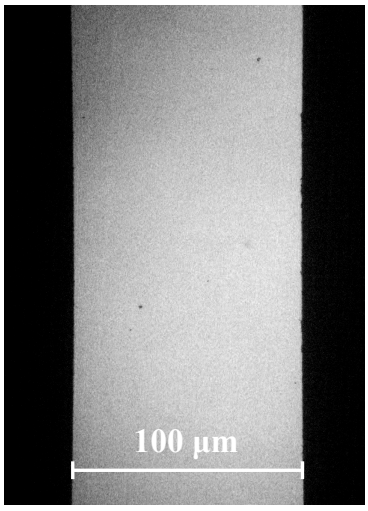

(d) A single lamella after cleaning (500×).

Figure 23: Reflected light microscopy images of grating-mirrors before **(a, b)** and after **(c, d)** adhesive removal. The shown areas are not identical. Apparent bends in the grating lamellas are due to image field curvature of the microscope lenses.

2.2.2 White-light interferometer

A beam splitting cube (BSC) is mounted in front of the SDU as part of an *in situ* white-light interferometer (WLI). A planar reference mirror (surface flatness better than 1.8 nm rms) is located beneath the BSC. The non-polarizing BSC has a splitting ratio of 50:50 and surface flatness of $\lambda/10$ at 633 nm. Several BSCs from Thorlabs and Edmund Optics ($\lambda/8$) have been tested for the quality of their interferograms using two planar mirrors. Important qualifiers are symmetry and a normal distributed envelope to facilitate fitting with an ideal simulated interferogram using the known WL spectrum (see Appendix 5.2). Figure 24 showcases an example of a real-world interferogram. What cannot be seen in the single image is the phase

relation over the extent of the BSC surface. If the main peak of the carrier wave shifts in regard to the envelope for different lateral positions a reliable path difference determination is not possible, in other words, it is crucial for the carrier-envelope phase (CEP) to stay constant.

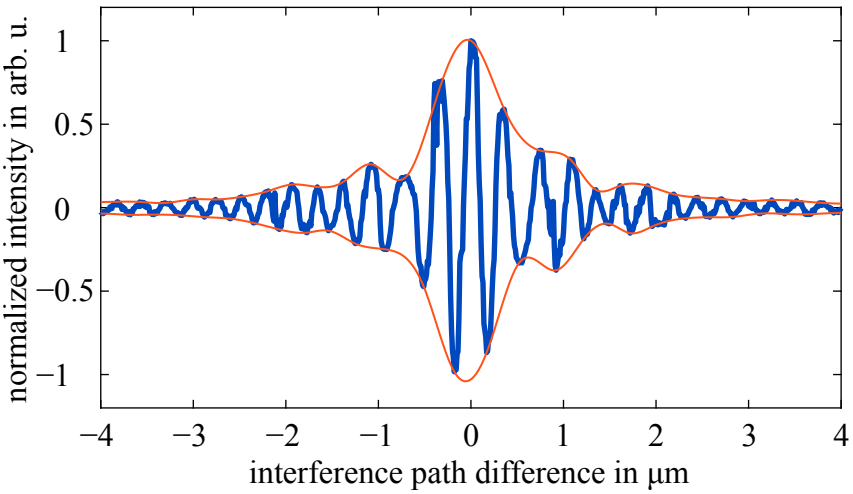

Figure 24: Exemplary interferogram (blue) and envelope (red) of a beam splitting cube from Thorlabs. The interferogram was measured in the center of the cube and averaged over 10 vertically stacked pixels.

The 1 W white-light emitting diode (WLED) is located outside of the vacuum chamber with multiple adjustment options. It emits a neutral white spectrum with a central wavelength of 570 nm. The coherence length is <2µm. Its divergence angle of 3° is sufficiently small without any further collimation. The reference arm length of the WLI can be manually adjusted *ex situ* by about 2 mm and *in situ* by a piezo actuator with a closed-loop travel range of 80 µm.
The WLI is used during the experiment to frequently perfectly co-align the two grating-mirrors *via* automated software and continuously monitor the relative displacement between them.

2.2.3 Grating-mirror surface roughness

The WLI can be used to estimate the longitudinal and angular displacement of the SDU within a few 100 µm range and can also be used to quantify the surface quality of the grating-mirrors, as described in Section 1.6. Figure 25 shows a so called 'heightmap' of a single grating-mirror. Any unevenness of the reference mirror or inconstant velocity of the piezo actuator results in adulterated measured profiles. The flatness of the reference mirror was ensured by sampling it with a second flat mirror and arranging them at different positions and orientations to exclude coincidental distortions. The accuracy of the fit depends on the point density of the interferograms and thereby the recording speed. Smaller skewing angles in the setup require less points. The custom-written software allows for arbitrary binning of neighboring pixels to reduce computer memory demand and fitting times. The gaps between the lamellas can also be excluded from the fit.

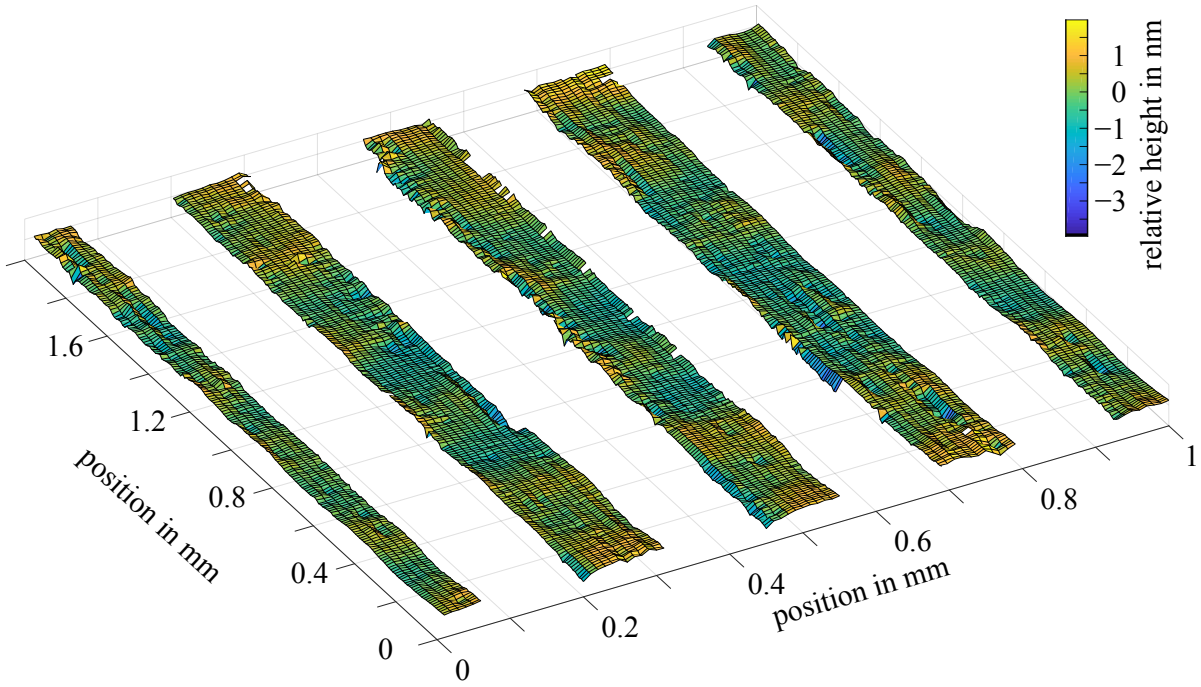

Figure 25: 'Heightmap' of a single grating-mirror covering a surface area of 1 mm × 2 mm. A larger BSC with a more symmetric interferogram has been used compared to the in-vacuum versions. Certain points at the edges of the lamellas were digitally removed because of bad interferometer fitting quality and the leftover gaps do not represent the real edges.

Figure 25 shows a heightmap and Figure 26 a histogram of the height distribution of a 1 mm by 2 mm surface area. A normal distribution with FWHM = 1.73 nm (rms = 1.27 nm) could be fitted to the height distribution, shown in Figure 26. According to equation (8), 22% of the total reflected intensity are lost due to diffuse reflection in this case. As such, the total reflectivity of the SDU alone is reduced to 15%. In general, a worse surface flatness results in larger focus spot sizes, but this effect is negligible at short wavelengths. Larger flat areas also allow for larger beam profiles and thereby increased intensity in the interaction zone without risking radiation damage of the grating-mirrors.

2.2.4 Camera

Initially, the WLI interference patterns were recorded using a 'Basler beat' camera with 12 MP resolution at ~60 frames per second (fps). The pixel size was $(5.5\ \mu m)^2$. The data was transmitted to an PCIe-1433 frame grabber card from National Instruments utilizing the full Camera Link specification.

Even though the camera's frame rate could be as high as ~800 Hz with custom regions of interest (ROI), all the FEL light pulses of one pulse train would arrive during a single camera frame[20] rendering the following ~79 frames superfluous. Therefore, the camera was operating at only 10 Hz, synchronized to the repetition rate of FLASH. Each camera frame is stored with the corresponding train ID, which can be received from a network address over Ethernet.

[20]The exposure time was 700 µs.

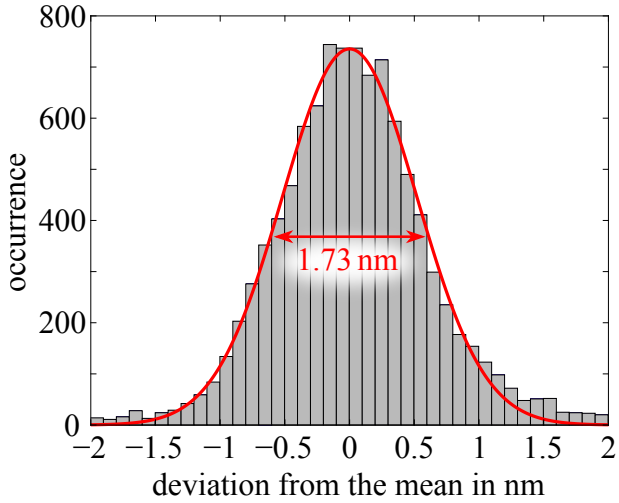

Figure 26: Height distribution of the single grating-mirror 1 mm × 2 mm surface shown in Figure 25. The fitted normal distribution has a FWHM of 1.73 nm.

Synchronization has been tested using the so-called 'fast shutter' at FLASH, a chopper wheel temporarily blocking one pulse train in the beamline. The self-written software manages all camera settings and data streams and saves the data frames in a custom uncompressed binary file format. Afterward, the files were losslessly compressed.

Paired with a 1:1 magnification macro lens the Basler camera covers an area of the object commensurate to the sensor size. The lens's focal length of 180 mm also allows it to be operated *ex situ*. The aperture is opened to the widest setting of $f/2.8$, which gives shallow depth of field but maximum sharpness in the focal plane. An optional teleconverter can be used to increase the magnification to 2:1.

Later on the camera was replaced by a 'Basler acA 1920-40gm' with 2 MP at 60 fps, pixel size of (5.86 µm) and data transfer over Ethernet.

2.2.5 Background vibrations

Any floor or air vibrations might be transmitted to the grating-mirrors and lower the interference contrast in the FEL beam focus and also reduce the WLI accuracy when the vibration periods are in the range of or longer than the camera exposure time. This is especially problematic if the two grating-mirrors tilt non-uniformly. Therefore, the stiffness of the torsion return springs is as high as possible without impeding the linear piezo actuators.

Furthermore, three passive vibration isolator feet VIB100-0205 from Newport have been tested beneath the SDU. Additionally a 12 mm thick solid steel plate was added to increase the oscillating weight and decrease the oscillation frequencies. The total mass above the three feet would be 6 kg, just below their combined load capacity of ~7 kg. Figure 27 shows the difference in the vibration amplitude without and with vibration isolators. The relative movement of the two grating-mirrors could be measured by reducing the region of interest of the camera to a minimum and increasing the frame rate to 800 fps.

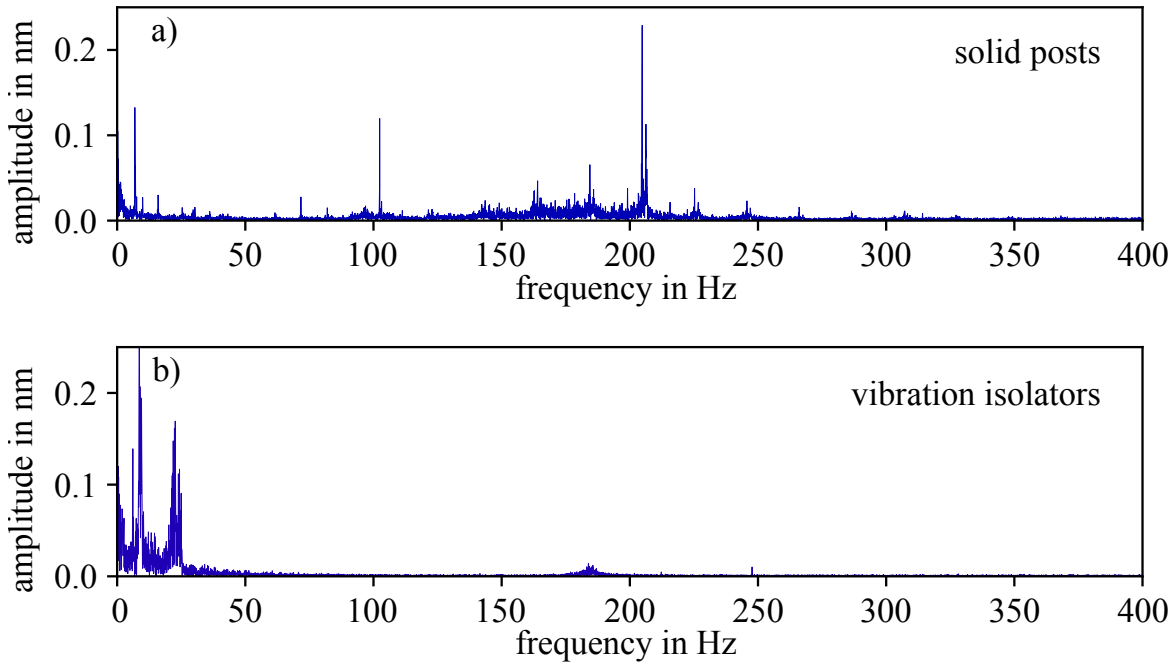

Figure 27: Fast Fourier transform (FFT) spectra of background vibrations without **(a)** and with vibration isolators **(b)**.

The vibration isolators effectively eliminate all vibrations with frequencies above 25 Hz but noticeably increase the slower ones, which could in return be monitored with the WLI and camera. Nonetheless, the next section describes the development of a superior active stabilization approach, which was key to achieve the experimental results presented in Section 3.

2.2.6 Active stabilization utilizing laser interferometers

In the course of this PhD project, the WLI was complemented by three in vacuum 'PicoScale' laser interferometers from the company SmarAct. Based on a 1530–1555 nm infrared (IR) laser [97] these position sensors allow for active feedback to the three linear actuators controlling the motion of the movable lamellar-grating mirror at a sample rate of approximately 39 kHz with self-reported picometer precision.

The PicoScale interferometers use a $(2\,\mathrm{mm})^3$ BSC and a deflection mirror to split the laser light into two parallel reference arms. The interference signal is then guided back through the optical fiber into the processing unit. An additionally imposed wavelength modulation helps in reconstructing the direction of movement and keeps the sensitivity phase-independent.

Each interferometer has four inter-dependent *ex situ* adjustable degrees of freedom for alignment. The three interferometers are mounted on a custom-made U-bracket between the WLI BSC and the grating-mirrors (see Figure 29). The U-shaped recess allows for the WL to pass through.

Due to the long coherence length of lasers it is not possible to determine the absolute zero of the path difference. For this reason the WLI still needs to be operational for calibration purposes. On the other hand, the absolute measurable range is increased to 30–65 cm, mainly limited by

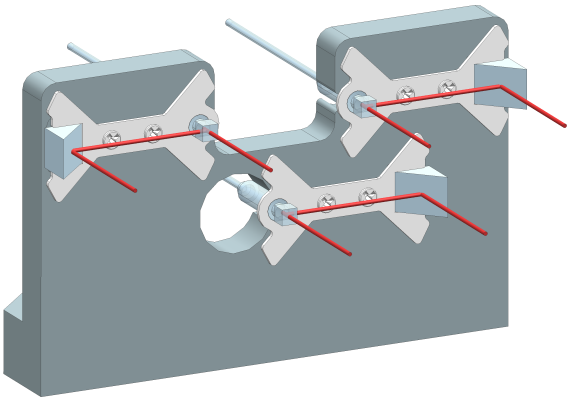

Figure 28: U-bracket with three differential 'PicoScale' laser interferomters. Each of the three units measures the changes in longitudinal distance between the two beam spots.

the beam divergence instead of the coherence length.
For each interferometer one beam spot is reflected directly from the fixed grating-mirror, while the second one is reflected from the movable grating-mirror mount. Reflectivity of the used IR wavelength is around 75% for Ni [98] and 55% for Si [99]. Retro-reflectors are employed in the movable grating-mirror mount to always guide the beams back to their origins[21]. Five out of six beam spots lie on the rotational axes to simplify the calculation of the three DoF. Only one spot is off-axis due to space restrictions. Displacement and horizontal angle can be calculated independently, conversely the vertical angular measurement is dependent on the two previous values. The implemented calculations are shown in Table 3. Detailed derivations can be found in [84, (in German)].

Displacement	$d = \dfrac{s_1 + s_2}{2}$
Horizontal angle	$\vartheta_\mathrm{h} = \dfrac{s_1 - s_2}{2(c_1 + c_2)}$
Vertical angle	$\vartheta_\mathrm{v} = \dfrac{s_3 - c_1 \cdot \tan(\vartheta_\mathrm{h}) - d}{c_3}$

Table 3: Calculation of the SDU's movement parameters with three linear distance measurements. s_1 and s_2 refer to the measurements of the two upper interferometers and s_3 to the lower one. $c_{1,2,3}$ are constant lengths (see Appendix 5.5).

The field programmable gate array (FPGA), which performs the above calculations has eight logic blocks of which three are reserved for the unaltered interferometer signals. The encountered miniscule angles allow for safe application of the 'small-angle approximation' eliminating the need of look-up-tables. Second and third order corrections for the interplay

[21] Different entry points in the retro-reflector do not alter the path difference. However, since the beam diameter is much smaller than the retro-reflector it must still hit the center to ensure overlap in the BSC.

between the degrees of freedom were explored but have not been implemented. First order uncertainties such as manufacturing imperfections on the scale of µm and non-parallelism of the interferometer arms prevail but still allow for nm precision. The corresponding pump-probe delay precision of ~1 as is well below the 15 as optical cycle of the $\lambda = 4.5$ nm radiation used in the FEL experiments.

The permanent path difference due to deflection of one of the reference arms is subject to thermal expansion. A countermeasure to this problem will be described in Section 4.2.

The three piezoelectric actuators for the SDU's DoF were replaced by piezoelectric inertia motors from SmarAct, which exert less force but have increased travel range. The restoring force of the torsion springs was lowered accordingly by a factor of 8. In Section 2.2.5 it was mentioned, that higher spring stiffness equals less vibrations. Now, a lower spring stiffness allows for faster active stabilization.

During each pulse train 16 grating displacement and relative angle measurements are taken with

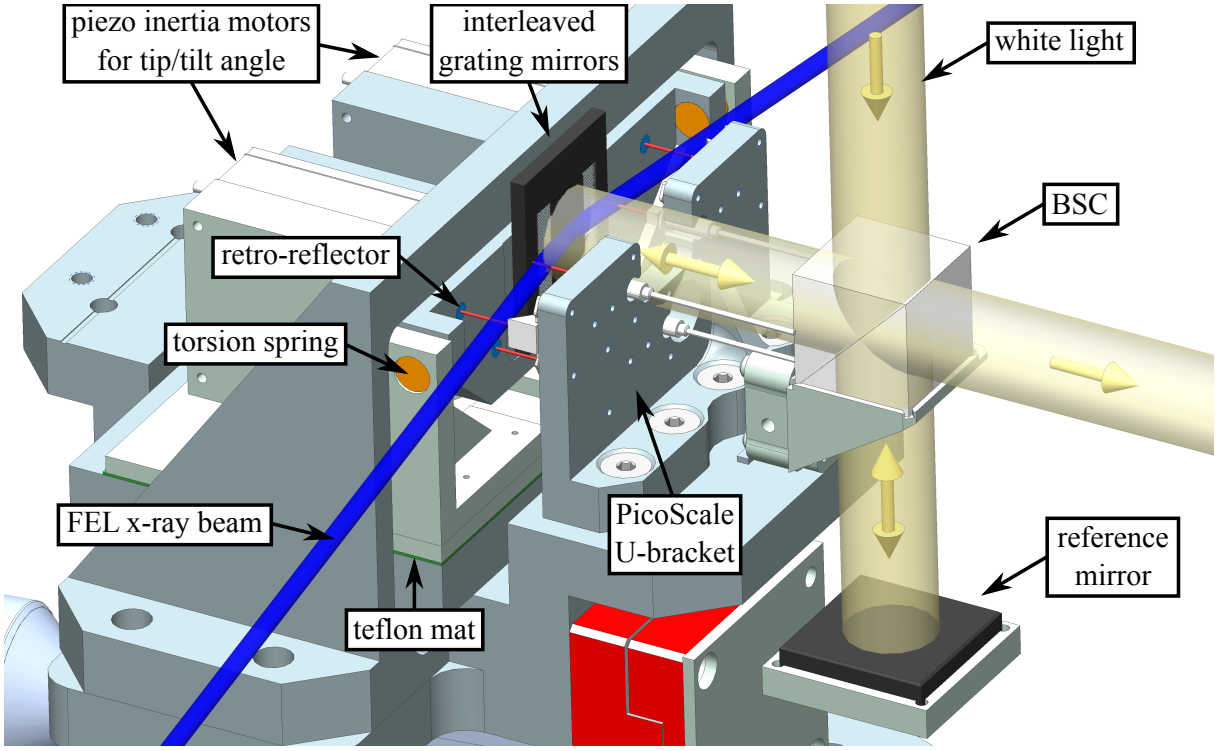

Figure 29: 3D model of the 'split-and-delay unit' with interleaved grating-mirrors, white-light interferometer, and three 'PicoScale' laser interferomters.

a spacing of 25.6 µs and subsequently averaged. For each pulse train the averages and standard deviations are saved together with the train ID, superseding the saving of WLI camera frames as done in previous experimental campaigns. The position data is used for absolute calibration of the FEL pump- FEL probe delays, i.e., used in the active feedback loop while the delay is scanned.

2.3 Focusing and order separation

The nearly collimated beams of each divergent diffraction order are focused by a Ni coated monocrystalline Si toroidal mirror with a mirror surface of $25 \times 25\,\mathrm{mm}^2$ unto the interaction zone. The source point of the FEL radiation is roughly 130 m away from the mirror; the mirror's focal length is 5.463 m; inserted in equation (9) this places the focal point 5.7 m away from the mirror. Assuming a TEM_{00} mode the Rayleigh length will be 291 mm.

The toroidal mirror is mounted on a parallel manipulator that allows it to move within 6 DoF with nm and µrad precision. This facilitates precise steering of the beam through the ideal interaction zone despite the 5.7 m long lever arm as well as matching the nominal 8° incidence angle of the toroidal mirror to prevent any astigmatism.

An additional plane mirror after the toroidal mirror can be lowered into the beam path under an incidence angle of 7.5° to redirect the beam toward a wavefront sensor (WFS) for beam profile diagnosis.

The separation of the diffraction orders is necessary in both spatially- and non-spatially-resolved detection. In the latter case all higher orders aside from the zeroth will be blocked, as is the case here.

Fixed tungsten slits with sizes 30, 50 and 100 µm, as well as a Ce:YAG screen or clear aperture can be moved in and out of the beam path 127 mm before the interaction zone. Tungsten was chosen as the slit material due to its high laser ablation threshold. Placing the slits as close to the focal point as possible is crucial for the separation of the orders without relying on even longer focal lengths. According to equation (12) the first order diffraction angle is 1 m°. Combined with the distance between the grating-mirrors and the slits this yields an order separation of 0.1 mm. Figure 30 depicts the beam profile on the illuminated Ce:YAG screen at the slit position. The sharpness of the orders will improve significantly at the focal point.

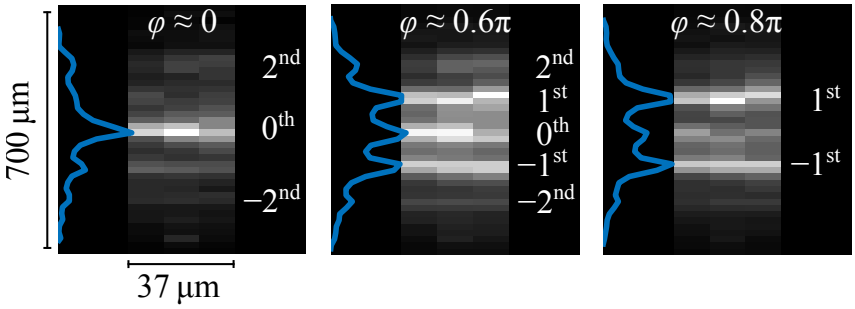

Figure 30: Diffraction order separation at the slit position for three different delays. The projected sum of the intensity is overlaid in blue. The sharpness of the orders will significantly improve at the focal point. An approximation for the phase difference φ between the pump and probe pulse beamfronts as well as the expected diffraction orders are indicated (at $\varphi = \pi$ the 0^{th} order will vanish completely.)

2.4 Molecular beam source

An effusive molecular beam was produced using a temperature-controlled, resistively heated oven design. The sample reservoir is made of a $14 \times 15 \times 40\,\mathrm{mm}^3$ aluminum cuboid and has a 150 mm long stainless steel capillary with 1 mm outer and 0.5 mm inner diameter attached to deliver the sublimated Gly molecules to the interaction zone. Both the crucible and the capillary have respective thermocouples and heating elements. In this way, the capillary can be prevented from clogging by keeping it heated until the reservoir has cooled down. The effusive[22] molecular beam source was operated at around 140°C to 160°C which results in a gas pressure on the order of 10^{-3} to 10^{-2} mbar in front of the nozzle.

An electrostatic potential is applied to the whole oven assembly and the capillary is guarded by a ceramic (AlO_2) sheath from electrical contact with the proximal electrodes. The oven is mounted on a xyz-manipulator so that the orifice can be steered as close as possible in front of the focus.

Figure 32 gives an estimate of the target density in the interaction zone, which is around ~350 to 900 molecules/mm^3. Since the capillary has a high length to diameter ratio, the spread of the gas immediately after the orifice can simply be approximated with the orifice area. Earlier measurements used a 10 mm distance between the orifice and interaction zone and a by an additional 25 mm retracted position for measuring the residual gas contribution to the spectra, where the target density is over an order of magnitude lower. For the calibration with noble gases the whole MBES chamber had to be flooded until an ambient pressure of about 1.6×10^{-6} mbar in the case of Ar was reached[23].

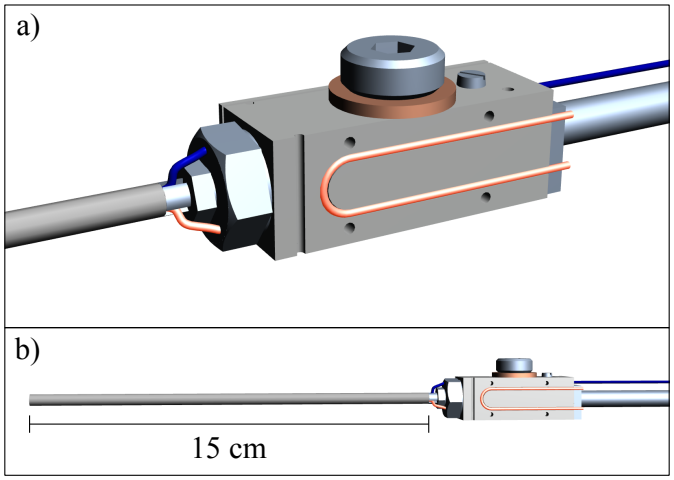

Figure 31: 3D rendering of the molecular beam source used for sublimating glycine. The capillary is welded onto a hollow screw. The top of the crucible is sealed by a screw and a softer copper washer. The heating wires (orange) are symmetrically on both sides of the crucible and held in place with side panels (not shown). The two thermocouples are colored blue. The ceramic sheath is held on by friction from clamping down the wires.

[22] Above 190°C the oven becomes a diffusive source.

[23] A correction factor of ~1.3 [100] has been applied to match the Ar pressure reading to an equivalent N_2 or air pressure.

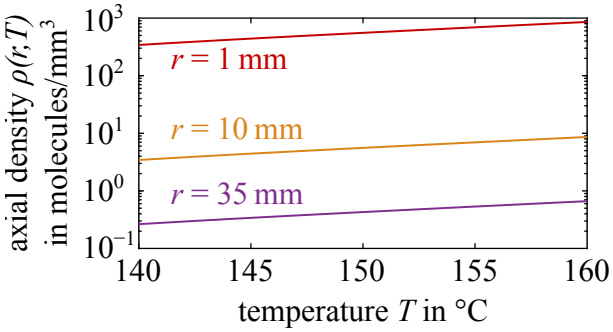

Figure 32: Estimated glycine effusive beam density $\rho(r,T)$ for three example axial distances r from the orifice as a function of temperature T. Since $\rho(r) \propto \frac{1}{r^2}$, the target density for any other distance r can be calculated. Glycine vapor pressure data is obtained from [67] and formulas are from [101].

An improved oven design was used for the later half of this work, additionally allowing for exchangeable noble gas sources to be fed from the back of the oven through the reservoir and capillary. This new design also features a faster cooling down method to facilitate the change from Gly to residual gas or noble gas measurements for spectrometer calibration without changing the geometry in the vicinity of the interaction point.

2.4.1 Glycine sample

The crystalline glycine powder was acquired from Sigma-Aldrich with >98.5% purity and no further purification was performed. Crystal sizes are on average estimated to be ~0.1 mm^3.

2.5 Spectrometer settings

Figure 33 illustrates the total 13 applied potentials at the ion ToF spectrometer and MBES. 'Ret 1' to 4 can be used to discard low energy electrons and fine tune the energy resolution of the remaining electrons. The electron repeller and extractor act as ion extractor and repeller respectively. The applied voltage values can be found in the Appendix 5.6.

The ion drift tube needs to be quite short to allow for collection of the heavy and slow ions before arrival of the next FEL pulse. This, however, reduces the mass-to-charge resolution.

The magnetic field of the permanent magnet in the interaction zone is $B_\mathrm{i} = 400\,\mathrm{mT}$ and at maximum $B_\mathrm{max} = 540\,\mathrm{mT}$ [102]. The electron drift tubes are wrapped in a solenoid to form a homogeneous magnetic field of $B_\mathrm{drift} \approx 8\,\mathrm{mT}$ [102], which yields an kinetic energy resolution of $\frac{\Delta E}{E} = 2\%$. Integrating equation (25) over the horizontal angle results in a total solid acceptance angle of about 82% of the full 4π sr. Applying an electrostatic potential further increases the collection rate of electrons beyond the acceptance double-cone.

Ambient pressures in the MBES were $<1.8 \times 10^{-7}$ mbar.

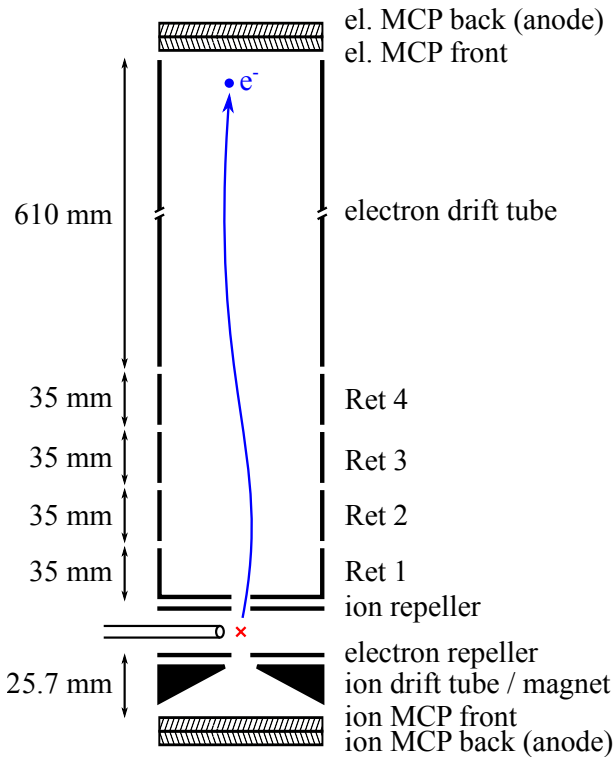

Figure 33: Scheme of the electron magnetic-bottle and ion time-of-flight spectrometer. The interaction zone is marked with a red cross. An illustrative electron flight path is indicated in blue. The complete length L from the interaction zone to the electron detector is 764 mm.

2.5.1 Detectors

Both the electron and the ion side use double multichannel plates (MCPs) in a chevron arrangement. Single electrons, ions or x-ray photons ionize secondary electrons in the microchannel walls. A voltage of about 2 kV is applied between the front and back of the MCP, which allows the secondary electrons to cascade into an electron avalanche. The open-area-ratio of the MCPs is 60% meaning 40% of all ionization products that impact on it will not be detected. More realistically, the total detection efficiency for electrons is around 40% [102].
The initial signals are then fed into conventional pre- and output amplifiers before being further analyzed by either an analog-to-digital or time-to-digital converter (ADC/TDC) and recorded.
The positions of the detector and electrodes of the MBES are fixed, whereas the positions of the interaction zone (FEL focus and capillary position), ion ToF spectrometer and the permanent magnet of the MBES can be adjusted.

The ADC signals were converted to discrete times using a software constant fraction discrimination (CFD) with a dead time of 50 ns to filter out overshoot. The zero crossing of the constant fraction signal was only evaluated within the accuracy of one ADC bin (0.5 ns). The 'FAST' TDCs do not require a hardware CFD but instead trigger on the rising edge (ramp-up time <0.3 ns) of the signal. The advantage of the TDC-based data acquisition (DAQ) system is the immediate feedback on the recorded electron and ion spectra and in turn allows to more precisely

calibrate the beam and detector positions and the voltages of the electrodes. The inherent pulse width of the MCPs is about 1 ns.

In order to avoid aliasing when converting the discrete ToF values to kinetic energy, either only the ToF bins were converted and the spectrum scaled via the Jacobian (see equation (31)) or a linear filter was applied.

Since both the ion and electron detector signals are recorded on individual ADC/TDC channels the t_0 and $t_{0,\mathrm{ion}}$ offsets based on the x-ray pulse arrival time on the detectors can slightly vary.

2.5.2 Electron time-of-flight to kinetic energy calibration

For the correct conversion from ToF to kinetic energy E_{kin} of the measured electron spectra, the noble gas argon was used, which has five well-documented binding energy levels that can be ionized at the FEL photon energy of $E_{\mathrm{ph}} \sim 274\,\mathrm{eV}$. The $3p_{1/2}$ and $3p_{3/2}$ energy levels lie 0.2 eV apart and cannot be individually resolved with the used MBES voltages.

Element	**K 1s**	**L_1 2s**	**L_2 $2p_{1/2}$**	**L_3 $2p_{3/2}$**	**M_1 3s**	**M_2 $3p_{1/2}$**	**M_3 $3p_{3/2}$**
Ar	3205.9	326.3	250.6	248.4	29.3	15.9	15.7

Table 4: Binding energies of specific Ar orbitals in eV. Reproduced from [80] and reference therein [81].

Additionally, several Auger decay lines from $L_{2,3}$ to MM are taken into consideration for the energy calibration. These lines lie very closely together. Figure 35b) illustrates the individual lines, as well as normal distribution curves with standard deviation σ corresponding to 2.5% of the respective E_{kin} to account for the energy resolution of the present MBES. The kinetic energy independent FEL bandwidth is not factored in here. The photo- and Auger electron spectral lines are obtained from two different publications and their relative intensities are scaled arbitrarily.

Figure 34 shows the linear regression performed for the energy calibration and 35a) the applied calibration to the measured data. The yield of the measured spectrum goes toward infinity for $E_{\mathrm{kin}} \to E_0$ due to the Jacobian.

For every used set of voltages applied to the MBES electrodes or change of FEL wavelength a separate Ar spectra was recorded and energy calibration performed.

The first-order relation between ToF and E_{kin} is given by equation (26) with the length of the ToF spectrometer flight path L, the electron mass m_{e} and U_{ret} the retardation voltage of the MBES. Substituting $x := \dfrac{1}{(t-t_0)^2}$ a linear regression can be performed with fitting parameters $a := \dfrac{L^2 m_{\mathrm{e}}}{2}$ being the slope and $E_0 := -eU_{\mathrm{ret}}$ the y-intercept. Figure 34 shows an exemplary energy calibration. The fitted value for the flight path length $L = (750 \pm 14)\,\mathrm{mm}$ is consistent within the error range over multiple sets of voltages and various photon energies.

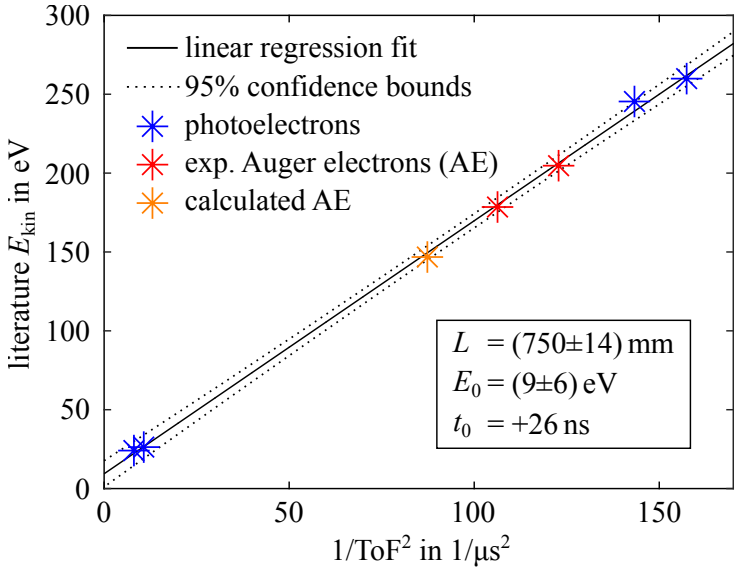

Figure 34: Exemplary time-of-flight to kinetic energy calibration of the magnetic-bottle spectrometer using Ar and a photon energy of E_{ph} = 274.7 eV. The fitted free variable E_0 agrees well with the applied retardation voltage of $U_{ret} = -10$ V. t_0 was determined beforehand from stray light FEL photons hitting the detector. The reference energies of the photoelectrons (blue) are specified in Table 4. The experimental (red) and theoretical (orange) Auger electron energies are defined by the local peaks in Figure 35b).

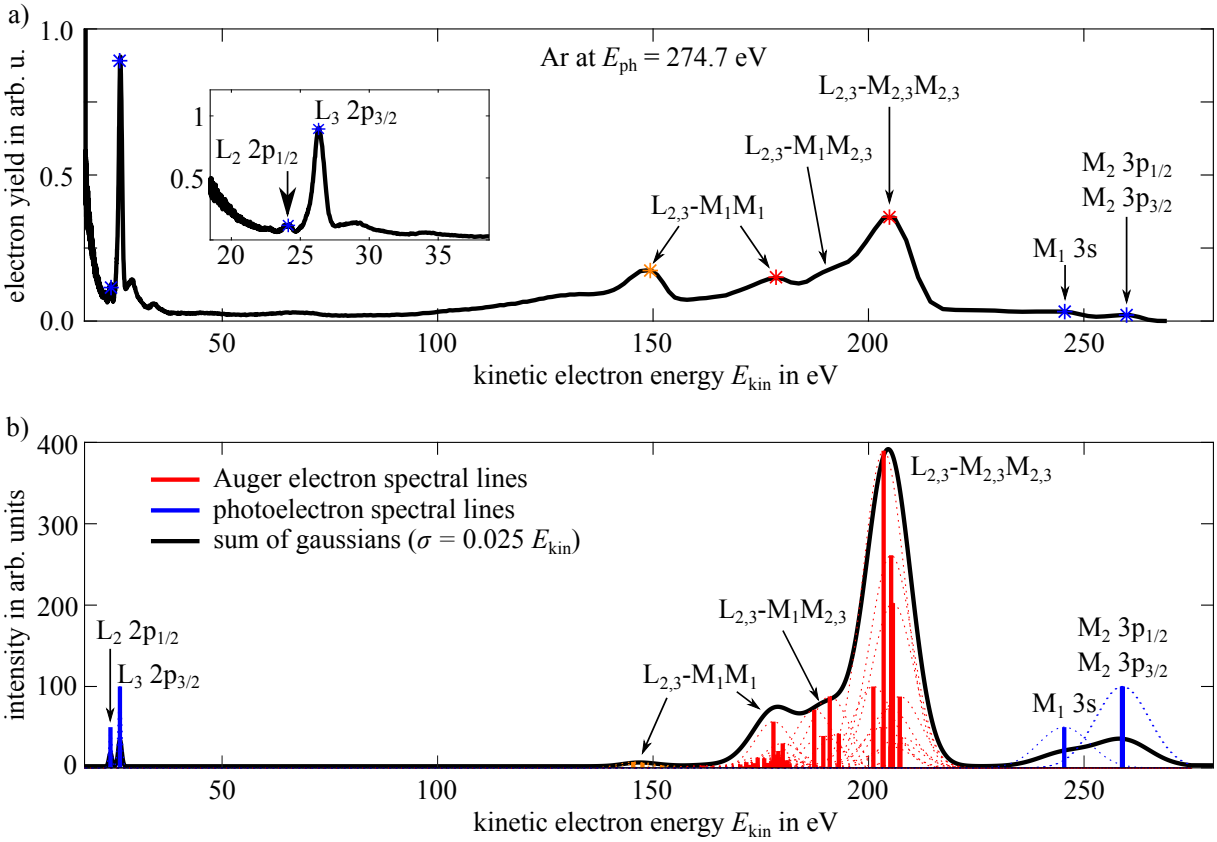

Figure 35: Measured calibrated **(a)** and literature **(b)** Ar spectrum at 274.7 eV. The photoelectron spectral lines (blue) are specified in Table 4. The experimental (red) and theoretical (orange) Auger electron spectral lines are from [103] measured at 265 eV. For each line a normal distribution curve with standard deviation σ corresponding to 2.5% of the respective E_{kin} is scaled to the respective intensity to account for the energy resolution of the present MBES. The full spectrum is given by the sum of each normal distribution.

2.5.3 Mass-to-charge ratio calibration

Similarly, mass spectra of the noble gases He (4.00 u), Ne (20.18 u), Ar (39.95 u) and Kr (83.80 u) [104] were recorded and a ToF to mass-to-charge ratio conversion based on equation (30) was conceived. Known parameters are the average masses of the molecules, the distance $L_2 = 25.7\,\mathrm{mm}$ between the ion side electrodes and their voltages $U_1 = -50\,\mathrm{eV}$ and $U_2 = -1800\,\mathrm{eV}$, as well as $t_{0,\mathrm{ion}}$. Left as a free parameter is the variable distance L_1 between the interaction zone and the first electrode (ion extractor). Figure 36 illustrates the mass-to-charge ratio m/q of the four aforementioned rare gases.

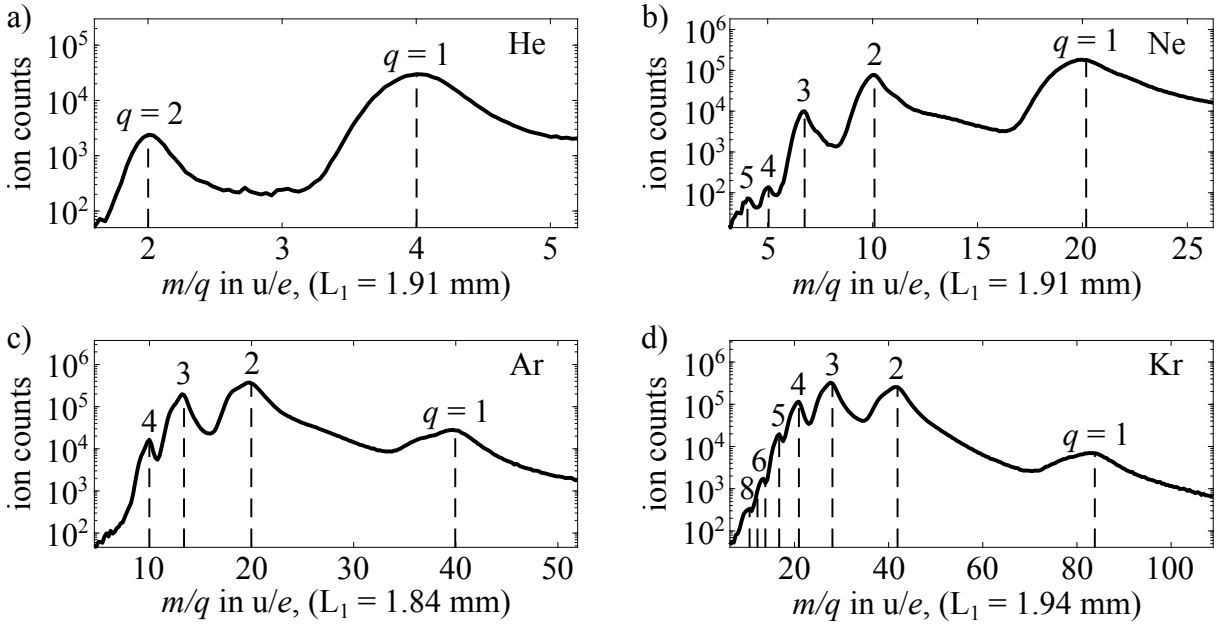

Figure 36: Noble gas ion spectra of He **(a)** Ne **(b)** Ar **(c)** and Kr **(d)** at 285 eV photon energy.

The calibrated Gly mass spectra, which were recorded afterward then use the latest value $L_1 = 1.94\,\mathrm{mm}$.

3 Results and interpretation

In this chapter time-resolved photoelectron spectroscopy is performed with orbital selectivity using sub-5 fs single-mode SASE pulses.

3.1 Photon energy dependent spectra

For Figure 37 the FEL wavelength was tuned from 4.42 nm (280.5 eV) to 4.61 nm (269 eV) in 0.3 nm steps by changing the FEL undulator gap width. For each step an electron spectrum at zero pump-probe delay, i.e., using single pulses, was recorded. Figure 37a) shows a linear interpolation between the respective spectra in a false-color plot.

The kinetic energy of the photoelectrons shifts equivalently with the excitation photon energy in superposition with the non-shifting Auger electrons (AE). All studied photon energies do not permit to ionize the C 1s MOs 4a′ and 5a′ but only to access the orbitals 6a′ to 16a′ ($10 < E_b < 34.3$ eV). The photoelectrons from a single photoionization partially overlap with photoelectrons from sequential double ionization processes. The SDI electron spectrum is generally shifted by the difference between the first and second ionization potential but can extend up to the first ionization potential due to high Rydberg states. The Auger electrons from C 1s core vacancies cover the whole extent of the studied kinetic energy range as can be seen in Figure 37a) [22].

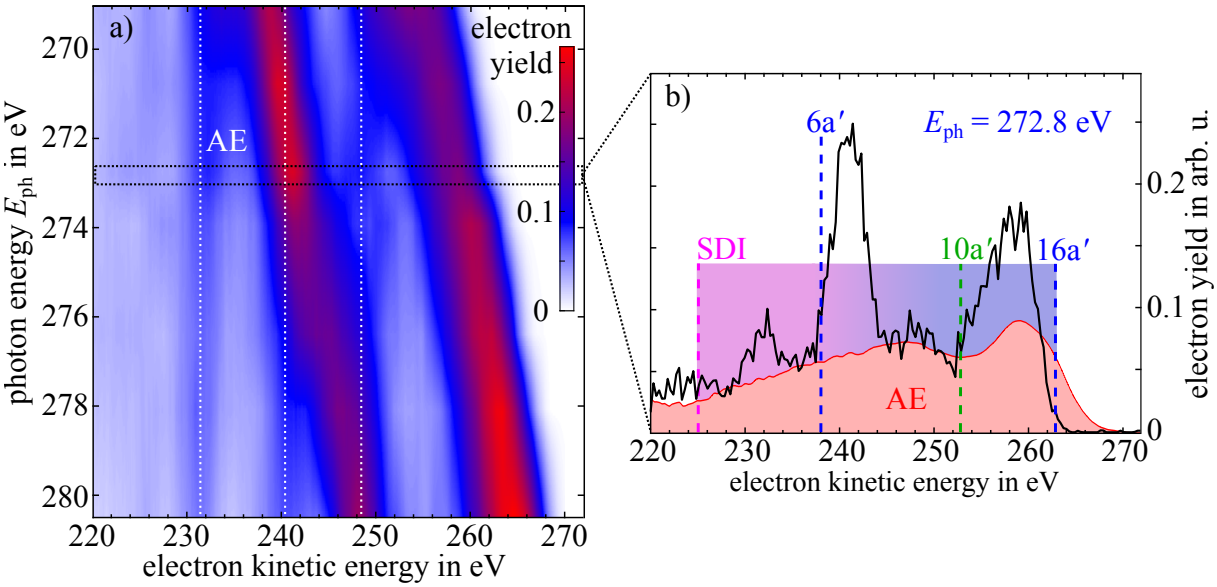

Figure 37: **a)** False-color map of the photon energy dependent glycine electron spectra linearly interpolated between seven discrete spectra.
b) A single electron spectrum at E_{ph} = 272.8 eV. The blue dashed lines mark the kinetic energy range of photoelectrons from direct photoionization. The contribution of SDI electrons (magenta) extends up to the 16a′ (HOMO) due to possible sequential ionization of high lying Rydberg states. The Auger electron spectrum, reproduced from [22], is indicated by the red shaded area.

3.2 Pump-probe delay scan

Following, the pump-probe time delay was controlled in the range between −0.9 and 24.1 fs in 0.93 fs steps at a central photon energy of $E_{\mathrm{ph}} = (274 \pm 1)$ eV. Residual gas measurements were taken at 24.1, 12.1 and 0 fs delays afterward and averaged to form the background spectrum for all delays. At each step the respective electron spectrum was recorded for 10 minutes. The FEL pulse energies, measured by the GMD on a shot-to-shot basis, were not reliable enough to eliminate FEL intensity fluctuations. Instead, each spectrum is normalized by the total amount of electrons per delay step.

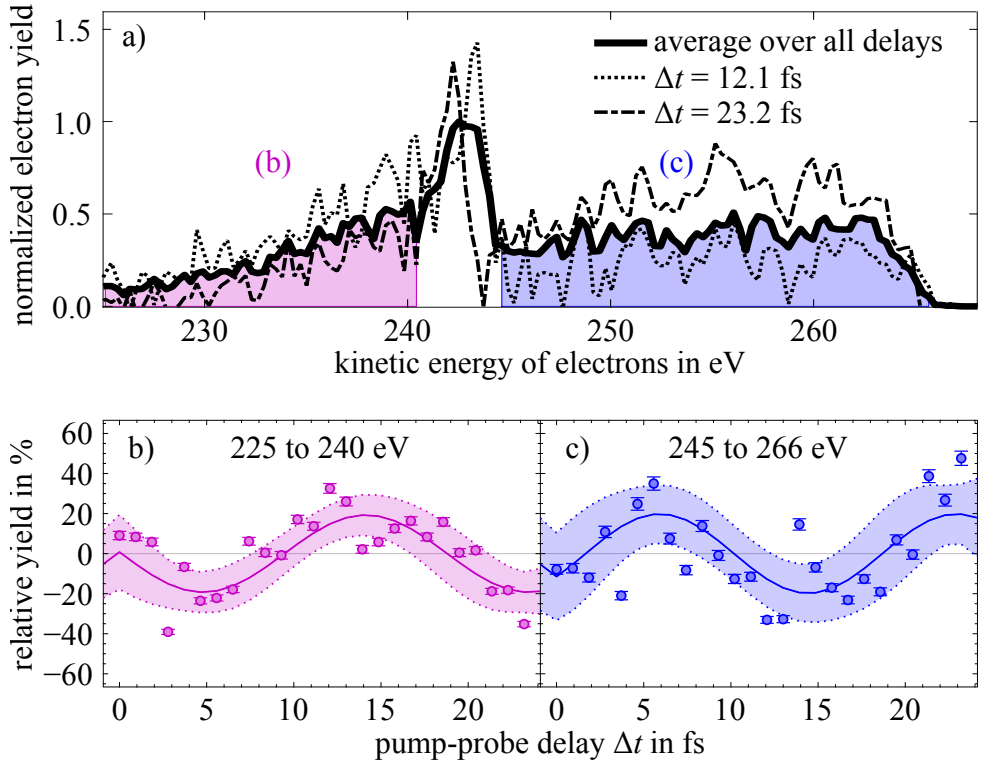

Figure 38: Average electron spectrum **(a)** over all delays and individual spectra for $\Delta t = 12.1$ fs and 23.2 fs recorded at $E_{\mathrm{ph}} = (274 \pm 1)$ eV. The maximum of the average spectrum is scaled to unity, the other spectra are scaled accordingly. Colored areas depict kinetic energy ranges where the time-resolved data shows opposite phase. **b)** and **c)** show the pump-probe delay dependent electron yield compared to the average over all yields for specific energy ranges marked in **(a)**. Vertical error bars represent statistical errors; pump-probe delay errors are too low to be resolved. A sine fit with 95% error bands is superimposed to the data.

Figure 38a) shows the residual gas background-subtracted average electron spectrum over all pump-probe delays, as well as two exemplary spectra at $\Delta t = 12.1$ fs and 23.2 fs. The delay-dependent electron yield in percentage around the average over all delays is given in Figure 38b) and c) for the two respective kinetic energy ranges prevailing direct photoelectrons (c) or SDI electrons (b). It is important to note that, from a theoretical perspective, the direct photoelectron emission channel cannot show any time dependence. When the pump and probe pulses are separated in time, the photoelectron has escaped the molecule before the probe pulse interacts with the molecular cation. Therefore, the delay-independent photoelectron yield background

is removed from the data by subtraction of the average over all delays. Nonetheless, both regions feature SDI and Auger electrons which are indicators of the time-dependent electronic coherence. For the data analysis, a sine curve of the form:

$$f_i(\Delta t) = A_i \sin\left(\frac{2\pi}{T_i}\Delta t + \varphi_i\right) \tag{36}$$

with amplitude A_i, period T_i and phase φ_i has been fitted to each kinetic energy range: $i = 1$ for 225 eV to 240 eV and $i = 2$ for 245 eV to 266 eV.

The two kinetic energy ranges show an anticyclic yield of almost equal strength ($A_1 = (19 \pm 7)\%$ and $A_2 = (20 \pm 10)\%$), with periods $T_1 = (19 \pm 3.3)$ fs, $T_2 = (17 \pm 4)$ fs and phases $\varphi_1 = (1 \pm 0.2)\pi$ and $\varphi_2 = (0 \pm 0.3)\pi$. All errors are given as ±2 standard errors (SE) rounded up.

In order to pinpoint the kinetic energy of the electrons at which the phase shift occurs, the relative electron yield changes have been analyzed in detail. A moving average with a window size of 4 eV simulates the energy resolution of the magnetic-bottle and FEL bandwidth. The step width is 1 eV. For each kinetic energy range i a sine curve with amplitude A_i, period T_i and phase φ_i was fitted to the relative yield. Fitting an offset c_i was omitted. The baseline of the relative yield change is defined by subtracting the mean over all delays in the corresponding energy range. This removes the time-delay independent pump-ionization background from the neutral molecule and probe-ionization background from states which do not exhibit quantum coherences, i.e., 13a′ to 16a′ [79]. If the relative yield offset were to be included in the fit, it would be below |±4|%. At $\Delta t = 0$ the fitted sine curves are mirrored.

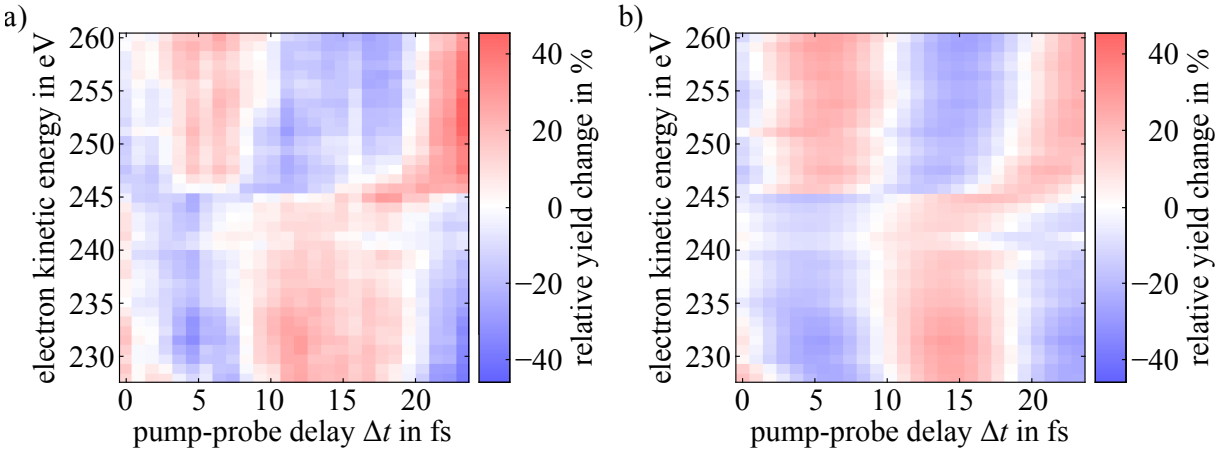

Figure 39: False-color plots of the kinetic energy averaged data **(a)** and fit results using 37 sine fits **(b)**. The moving average uses a window size of 4 eV and step size of 1 eV. The y-axis labels designate the center of the window. The fitted parameters are show in Figure 41.

The measured data with the applied moving average is shown in Figure 39a) compared to the fit results shown in Figure 39b). A second, independent from the first, moving average along the pump-probe delay with a window size of 4.6 fs has been applied to the false-color map of the

experimental data, in order to clearly observe the general trend, which was not applied for the fitting of the data. The individual values of the fitting parameters can be seen in Figure 41. Figure 40 shows a similar fit, but this time the constant period T was evaluated from fitting all energy ranges at once. This fit with 75 free parameters uses the results of the previous individual fits as starting values. The fit results in the period $T = (18.1 \pm 0.7)$ fs. The error of the fitted amplitude is on average ±11% and of the phase ±0.6 rad, all within 2 standard errors (SE).

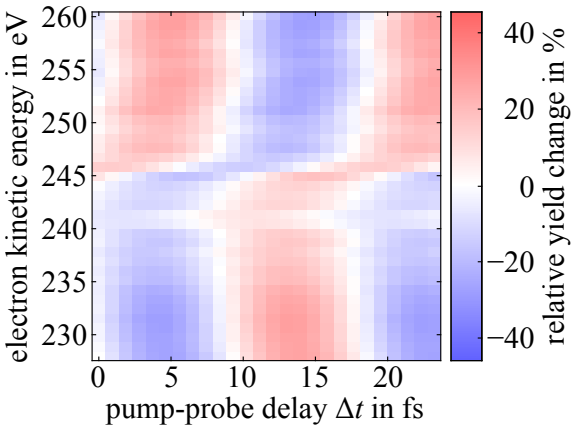

Figure 40: Fit results when using a single period for all energy ranges. The fitted period within two standard errors is $T = (18.1 \pm 0.7)$ fs. The coefficient of determination R^2 of the fit is 0.34.

Figure 41b) shows the fitted phase φ_i. The oscillations undergo a kinetic energy dependent π-phase shift from $(1.0 \pm 0.3)\pi$ to $(-0.2 \pm 0.3)\pi$ on average. The energy range between 240 and 245 eV is not simply explained by a mutual cancellation of the two superimposed oscillations but a complete breakdown of the MO and any electronic coherences as evidenced by numerical simulations (see Section 3.3). Due to their degeneracy the electrons cannot be allocated to a specific creation process. However, ranges where the relative yield is canceled out to a flat signal can mathematically also be constructed through very large periods. This is the reason for the stronger deviation at 246 eV and nearby kinetic energy ranges from the constant period T.

According to equation (20) the corresponding energy level splitting of the 10a′ orbital related to the observed time period is then $\Delta E = (229 \pm 4)$ meV in the simple two state picture.

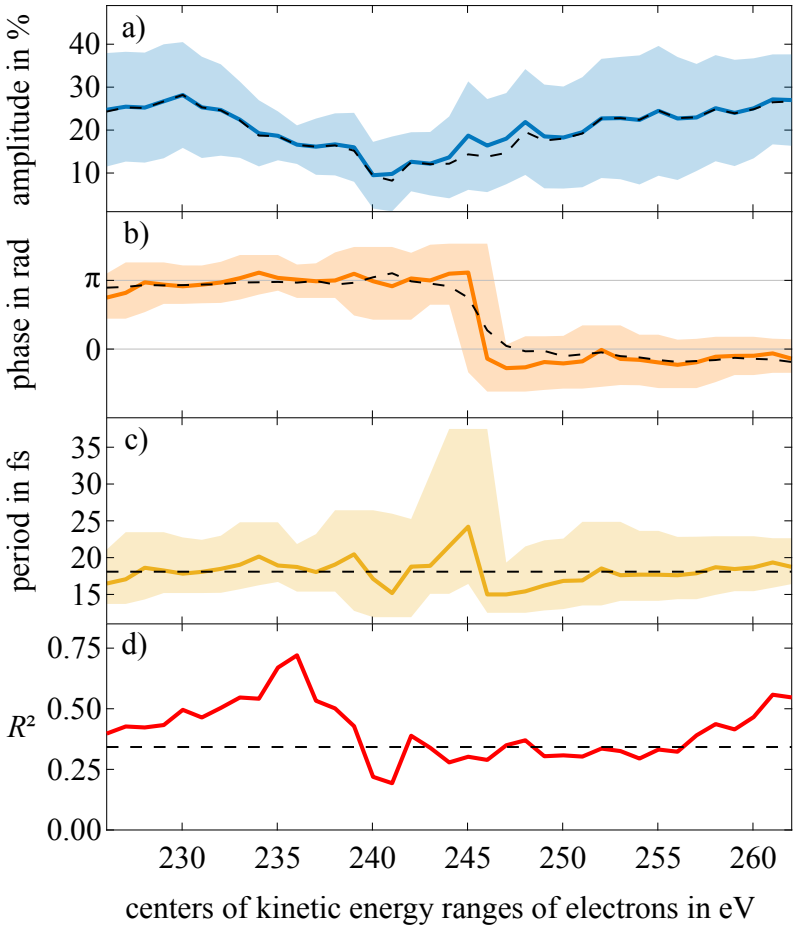

Figure 41: Fitted amplitude **(a)**, phase **(b)**, period **(c)** as well as the coefficient of determination R^2 **(d)** for each energy range. The error bands represent ± two standard errors. The fit results for using a single period for all energy ranges are depicted as a black dashed line.

3.3 Comparison with numerical many-electron simulations

Ab initio time-dependent RCS-ADC[24] simulations [105] by Marco Ruberti (Imperial College London) [3, 4] were performed following the above findings, which will be briefly discussed here. For more details of the used methods, the interested reader is referred to [79]. The simulation uses the measured FLASH pulse parameters obtained in Section 2.1.2. However, the pump and probe step are calculated independently, meaning the pulse overlap at short delays is not taken into consideration. This is due to the fact that a pulse overlap would require to model two photons for one interaction, which is currently not possible within the computational framework [79]. Moreover, vibronic coupling cannot be described fully quantum mechanically, but instead by averaging over the nuclear quantum uncertainties at the zero-point energy. The oscillation periods could be quantitatively reconstructed and furthermore agree well within the error margins of the experimental findings.

Figure 42 shows the simulated hole density evolution of the 10a′ pure-state, consisting of

[24]RCS = Restricted Correlation Space, ADC = Algebraic Diagrammatic Construction, The populations, degrees of coherence and relative phases between each pair of accessible cationic states were computed using the ADC(2,2) method [105].

a coherent superposition of eigenstates in the 10a′ band, on a full charge oscillation period timescale. Blue colored iso-surfaces indicate positive hole densities and red negative ones (i.e., electron densities) in comparison to the neutral molecule. After being created at $\Delta t = 0$ fs by the x-ray pump ionization at the C_α atom, the hole density decreases at the C_α, C and O_H atom in that order until $\Delta t = 10.6$–11.8 fs. Afterward, the charge migration is reversed until a full period is completed.

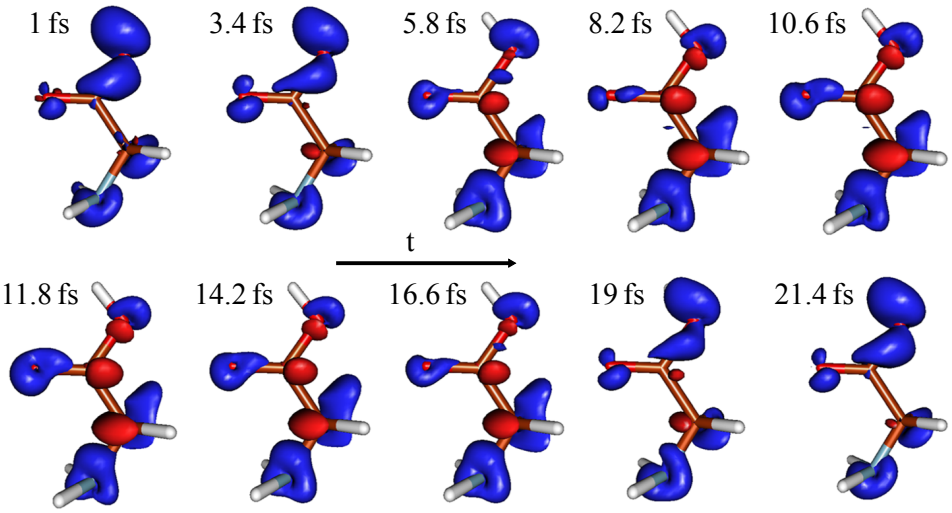

Figure 42: Simulated hole densities corresponding to the correlated 10a′ pure state channel between $\Delta t_1 = 1$ fs and $\Delta t_{10} = 21.4$ fs after the pump ionization event. The density iso-surfaces displayed are the ones with value 0.015, blue and red colors indicate positive and negative values of the hole density, respectively. Calculation performed by Marco Ruberti. Adapted from [79].

For the simulation of the probe pulse, two further coherent ionic channels, namely the level splitting of 9a′ and energy gap between 11a′ and 12a′, are taken into consideration, which have similar pump-produced population ratios (9–15%). Due to their similarity of ionization potentials ($IP_{9a'} \sim 23$ eV, $IP_{10a'} \sim 20$ eV, $IP_{11a'/12a'} \sim 17.5$ eV for Gly I, derived within the theoretical model), they can be populated to some extent within the spectral bandwidth and subsequently decay *via* the Auger effect. The 4a′ → 9a′ excitation is closer to resonance, while the 5a′ → 11a′/12a′ is off by ~2.5 eV. Figure 43 shows the individual probe-induced electron yield containing Auger electron and sequential double ionization contributions from the three different pure-state channels. All three not only have a similar energy level gap of 0.2–03 eV and therefore similar oscillation periods, but also start with a similar phase. The 11a′/12a′ orbitals feature the cleanest spectrum with only two predominant lines and thus offer the closest approximation to a sinusoidal oscillation.

The *ab initio* numerical calculations show that the phase shift only exists for the SDI electron signal but not for the Auger electron signal. Since the SDI signal is at least one order of magnitude stronger at this off-resonant photon energy of (274 ± 1) eV, the superposition of the two channels is dominated by the SDI signal, flipping the relative yield for the higher kinetic

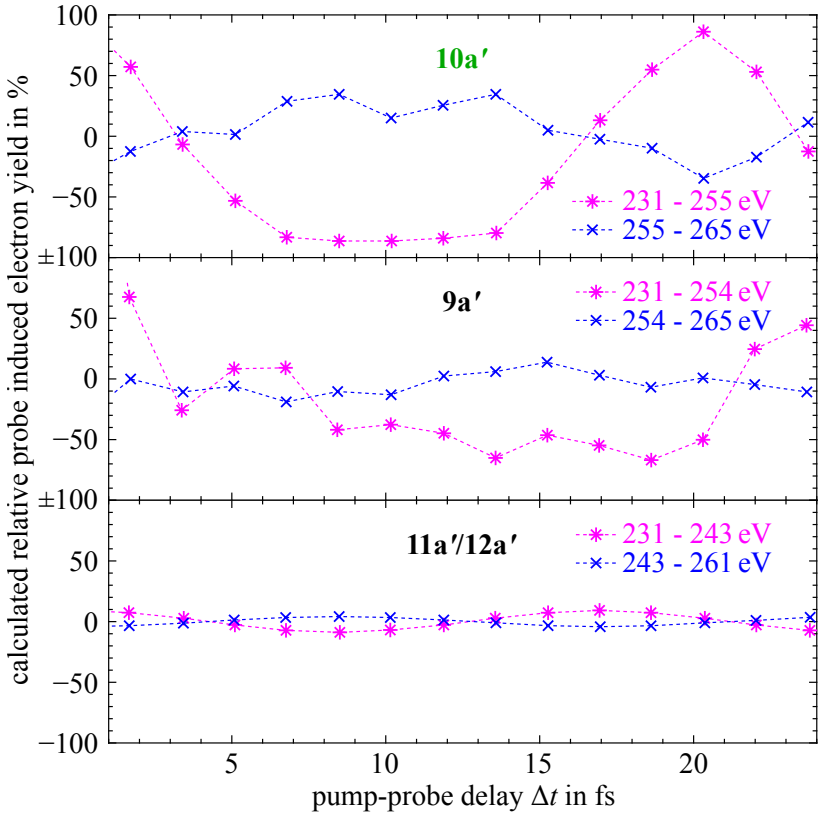

Figure 43: Calculated relative yield oscillations due to coherent superpositions of eigenstates in 10a′, 9a′ and 11a′/12a′ as a function of x-ray pump-probe delay. Both specified energy ranges per plot contain AE and SDI electron contributions. Calculations performed by Marco Ruberti. Adapted from [79].

energies (255–265 eV). The explanation for the π phase difference between the two different kinetic energy regions of the SDI photoelectron spectrum is the following: The spectral region of the phase shift exhibits a high density of doubly-ionized satellite states (3h1p configurations), which lead to a breakdown of the MO picture of double ionization, where it is no longer possible to distinguish between the main states (2h) and satellites (3h1p) [106]. Direct photoionization of the pure 10a′ 1h state cation by the probe-pulse will mostly lead to higher-excited dicationic 2h eigenstates and a low kinetic energy photoelectron. On the other hand, ionization from the lower-energy 2h1p cationic state with two outer-valence holes and less screening predominantly leads to lower-energy 3h1p dicationic states, accompanied by a higher-kinetic energy photoelectron. Immediately after the pump-ionization, the two-state system of the linear combination of 1h and 2h1p states is prepared in the pure 1h state. As such, the yield of photoelectrons in the lower kinetic energy range is at maximum at $\Delta t = 0$ fs, while the relative yield of the higher kinetic energy photoelectrons compared to the average of both is at its minimum. During the time evolution of the system both populations will be periodically inverted.

The calculated relative yield variation amplitudes for 10a′ for lower (231–255 eV) and higher kinetic energy ranges are ~80% and ~30%, respectively (compare Figure 43a)), which is on the order of the experimental findings. The other two ionic state superpositions show a similar

behavior, each with their respective yield amplitude based on initial pump-produced population, resonance proximity and different phase shift electron kinetic energy depending on the individual orbital. The theoretical model predicts the cumulative phase shift at $E_{\mathrm{kin}} \sim 255$ eV, 10 eV higher than observed in the experiment, which can be attributed to only including 2h but not 3h1p configurations in the simulation [79]. One has to be aware that the observed oscillation in the relative change of detected electrons is only slightly above noise level in the off-resonance excitation channel (see Figure 38a)). Thus, a quantitative comparison of the observed oscillation amplitude between experiment and theory is rather difficult in the sequential double ionization channel. Nevertheless, the calculated period is about 20 fs for both kinetic energy regions, which is a perfect match between experiment and theory.

3.4 Resonant core-orbital excitation

The calculations also predict a photon energy dependence of the Auger and SDI electron yield ratio. The former photon energy of (274 ± 1) eV is slightly off-resonant for the C 1s $\rightarrow$ C 2s transitions[25] ($4a' \rightarrow 9a'$, $5a' \rightarrow 10a'$), leading to a relative decrease of AE with respect to SDI electrons. As mentioned, the SDI contribution is roughly one order of magnitude stronger at 274 eV. On resonance, the C 1s core-hole excitation channel (i.e., probe-induced Auger decay) dominates and the splitting ratio is expected to be 3:1 based on the *ab initio* simulations. Figure 44 shows the experimental photon energy dependent yield of exactly two detected electrons per pulse with one of them from the 10a′ orbital, i.e., fixing its kinetic energy to $E_{\mathrm{kin}} = E_{\mathrm{ph}} - E_{\mathrm{b,10a'}} \pm 0.5$ eV (varying with E_{ph}) and the other with $E_{\mathrm{kin}} \gtrapprox 220$ eV in the analysis of electron-electron coincidences. This procedure allows to identify the photon energy for the resonance-enhanced, probe-induced Auger decay channel (see the experimental AE spectrum with $E_{\mathrm{kin}} \gtrapprox 220$ eV in Figure 37b). Once the FEL photon energy hits the transition resonance, the selected two-electron coincidence yield shows a maximum. The orifice of the molecular oven was moved from 10 mm to 1 mm in front of the FEL beam focus, increasing the target density and thereby count rate by a factor of 100 and allowing for electron-electron coincidence measurements shown in Figure 44. The previous data set presented in Figure 37 did not allow for coincidence analysis because of the rather low count rate.

[25] While $\Delta\ell = 0$ transitions, where ℓ is the azimuthal quantum number, are forbidden in centrosymmetric complexes according to the Laporte dipole selection rule, the two C atoms in this case are of tetrahedral and near trigonal planar nature, thus enabling s-s excitation and decay. Electronic transitions which are normally forbidden by the selection rules may also be allowed in the case of vibronic transitions breaking the centrosymmetry [107].

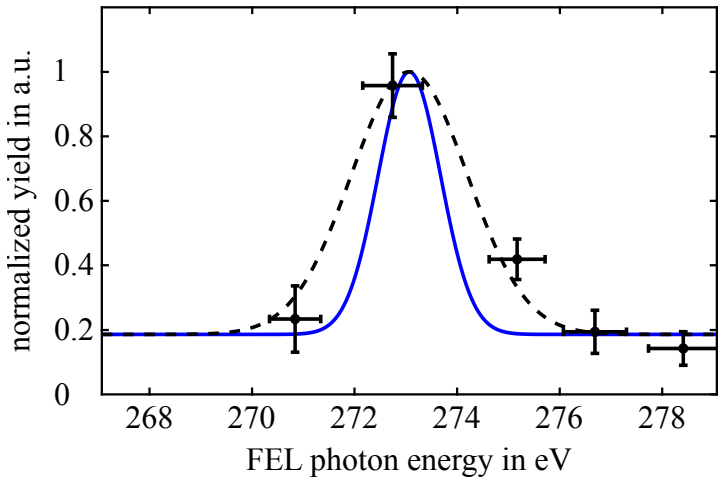

Figure 44: Photon energy dependent two electron coincidence yield. Only coincidences including one electron within a narrow 1 eV window around the 10a′ orbital (varying with E_{ph}) and the other electron $\gtrapprox$220 eV were selected. Horizontal error bars represent FEL photon energy fluctuations and vertical error bars the statistical error. A normal distribution (black, dashed) was fitted to the data taking the uncertainties into account. The previously determined bandwidth $\Gamma = 1$ eV of the FEL was deconvolved (blue, solid) from the fit to indicate the true width of the resonance. Adapted from [79].

The fitted and deconvolved normal distribution has a central photon energy of $E_\mu = (272.8 \pm 0.3)$ eV and standard deviation of $E_\sigma = (0.44 \pm 0.02)$ eV. In the following time-resolved and probe-induced Auger electron spectroscopy this resonant photon energy was used, which further increases the count rate.

3.5 Coincidence spectroscopy

In this section, the pump-probe delay scanning range is increased to up to 175 fs. This allows to determine the oscillation periods with more sophisticated analytical tools such as short-time Fourier transform (STFT) or, as in this case, continuous wavelet transform (CWT). STFT uses a fixed sliding window, whose width severely affects the results. Shorter windows emphasize faster oscillations and longer windows slower ones. STFT, on the one hand, has either good time or good frequency resolution [108]. CWT, on the other hand, uses a flexible time-frequency window and gives better time-frequency resolution [85]. This allows the study of the amplitude evolution of particular oscillations.

For this data set, recorded upon resonant excitation at zero delay and significantly higher glycine sample density (factor 100), the ionization products from the residual gas were several orders of magnitude lower compared to the off-resonant data set discussed in Section 3.1 and 3.2. Thus further residual gas measurements at different pump-probe time delays were omitted. The comparative residual gas measurement can be found in the Appendix 5.4.

The photoelectrons were also measured in coincidence with photoions using the calibration from Section 2.5.3. Figure 45 shows the spectrum of glycine molecules recorded at a photon energy

of E_{ph} = 272.7 eV. Since the ion ToF drift tube is quite short the mass resolution is restricted but good enough to differentiate between the main fragmentation pathways.

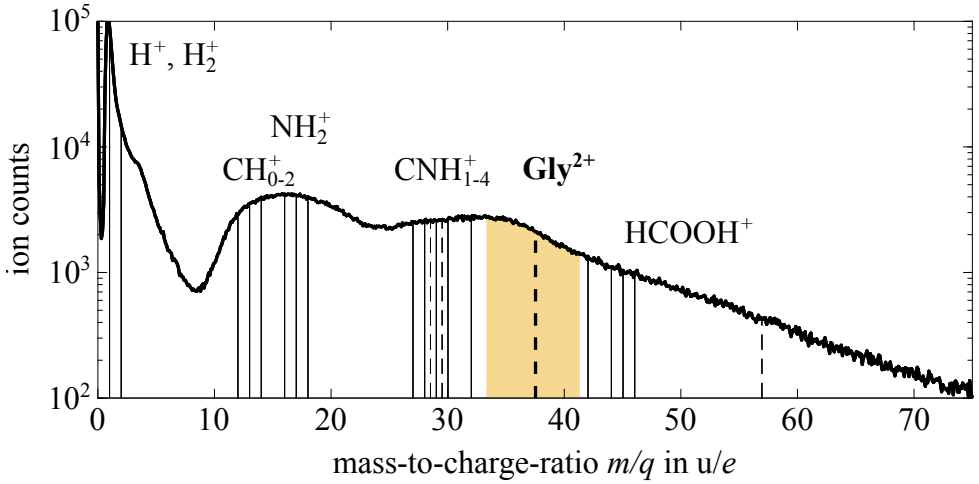

Figure 45: Mass-to-charge ratio spectrum of the glycine mother ion and fragments at E_{ph} = 272.7 eV and averaged over all delays of Δt = 0 to 175 fs. Vertical lines mark the mass-to-charge ratio of common fragments. The right-hand edge of the spectrum corresponds to Gly^+. The range around Gly^{2+} (m/q = 37.5 ± 4 u/e) will be evaluated more thoroughly.

Figure 46 shows that longer delays (Δt > 100 fs) in general yield larger ionization fragments and more frequently intact Gly^{2+} molecules (m/q = 37.5 u/e). However, the yield of any fragments with m/q > 16 u/e is transitionally minimized at Δt = 35 to 55 fs. The reasoning behind this, based on vibronic excitation and relaxation, will be explained in detail in Section 3.5.3.

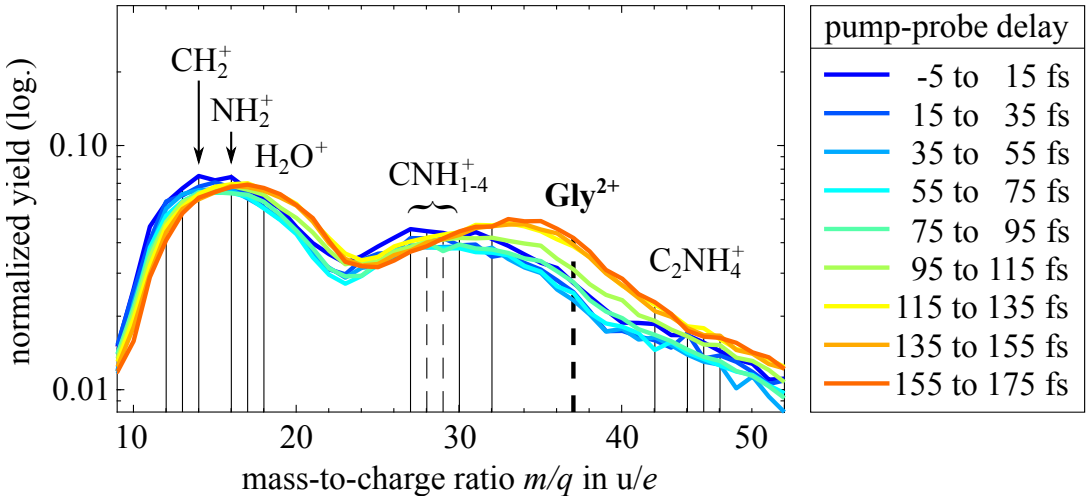

Figure 46: Shift of the glycine fragmentation pattern with increasing pump-probe delays. The characteristic cationic fragments are marked by vertical lines (dashed lines for dications) and the most notable have been labeled. All spectra are normalized to the not shown H^+ peak.

3.5.1 Photoion-photoion coincidence

To further elaborate the fragmentation process of glycine a photoion-photoion coincidence (PIPICO) map is presented in Figure 47.

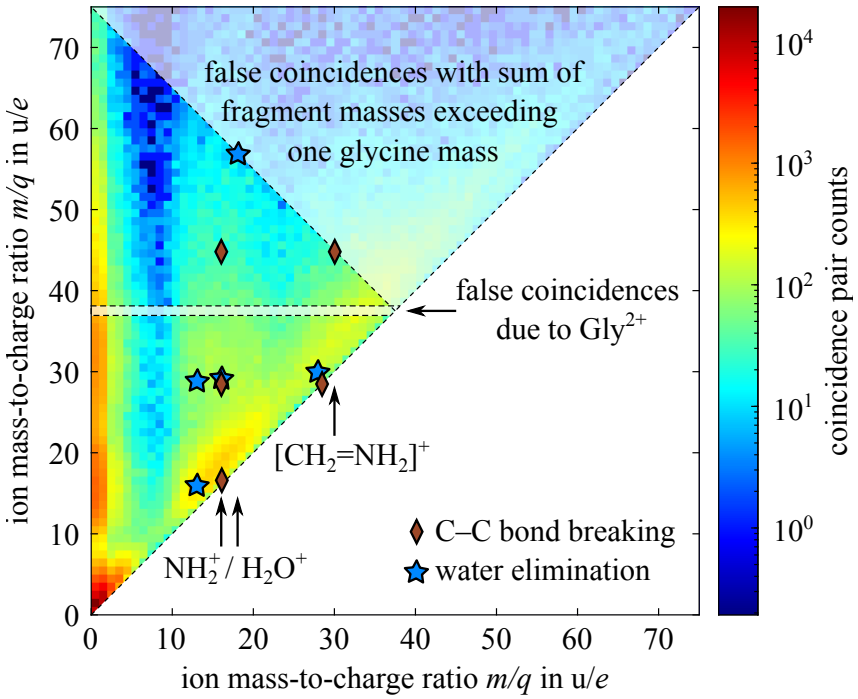

Figure 47: Photoion-photoion coincidence map integrated over 175 fs pump-probe delay. Two notable regions of false coincidences have been marked (white shaded area). Red diamonds indicate possible fragment pairs following the C–C bond breakage pathway, while blue stars indicate those from water elimination. Three different cationic fragments are indicated to give guidance.

Foremost, it shows that all photodissociation processes can be accompanied by H^+/H_2^+ losses. Secondary, the light to medium weight fragments form a pronounced off-diagonal, showing that most fragmentation pathways lead finally to similar masses. However, also intermediate steps in the fragmentation processes are visible, which are vertically offset upward or horizontally offset to the right of their daughter ionic fragments in the PIPICO map.

It should be noted, that near-diagonal elements may also appear due to false coincidences. Furthermore, a coincidence of two cations with a combined mass larger than one glycine mass leads to false ion and thereby false electron coincidences. Similarly, any coincidence events including a dication and another charged ion result in false coincidences. The indicated region of false coincidences including Gly^{2+} is experimentally larger due to the ion ToF spectrometer resolution. For other dications the false coincidences are more difficult to isolate because of overlap with singly charged cations.

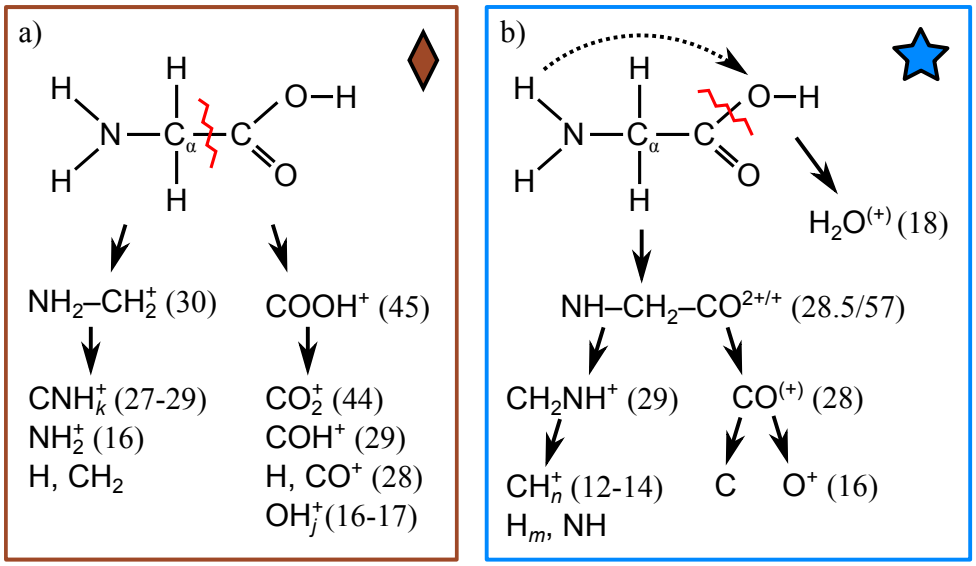

Figure 48: Glycine fragmentation pathways based on findings in Figure 47 and [78]. The two distinct processes are defined by initial C–C bond breaking **(a)** or water elimination **(b)**. Mass-to-charge ratios are given in brackets in u/e where applicable. ($n = 0, 1, 2$; $m = 2 - n$; $k = 1, \ldots, 4$, $j = 1, 2$)

Major fragmentation pathways include C–C bond breakage resulting in fragments with m/q of (30, 45) and further splitting into (16, 45), (27–30, 28-29), (16, 28–29), (16, 16–17) or minor variations as can be seen in Figure 48. The decreasingly smaller fragment pairings exhibit exponentially increased yields.

The second sketched pathway of water elimination produces the combinations (18, 57), (28, 29), (12–14, 28), (16, 29) or (12–14, 16). The doubly charged $[NH–CH_2–CO]^{2+}$ cannot be present in the PIPICO map (Figure 47) albeit as false coincidences. The intramolecular proton transfer (protonation) depicted in Figure 48b) (dashed arrow) relies heavily on the interatomic –H$\cdots$O– distance. Bending of the whole molecule as well as rotation around the N–C and C–C bond can introduce oscillatory distance variations on a ~90–100 fs timescale [109, based on simulations in aqueous solution].

3.5.2 Photoelectron-photoelectron coincidence

Furthermore, Figure 49 shows a coincidence map of all electrons over all delays.

The diagonal lines perpendicular to the auto-coincidence diagonal are the result of single-photon double ionization (SPDI). Their kinetic energies can be at most 241 eV due to the DIP of 32 eV. These electrons cannot exhibit delay-dependent yield variations because of the prompt single-photon double ionization of the neutral molecule. In the upper right triangle $\left(E_{\mathrm{kin},1} \gtrsim E_{\mathrm{kin},2} \gtrsim 225\,\mathrm{eV}\right)$ exist contributions of SDI electrons that overlap in energy with Auger electrons.

The coincidence peak of Auger electrons between 170 and 207 eV and corresponding photoelectrons at 29 eV (horizontal ellipse in Figure 49) originates from residual Ar gas, which was used

in the MBES chamber 8 hours prior to the glycine measurement. Likewise, the coincidence events at around 163 eV and 1–80 eV (vertical ellipse) are a result of double Auger decay in Ar [110]. These ionization events do not affect the following analysis, since they are filtered out based on their mass-to-charge ratio of 20 u/e for Ar^{2+} ions.

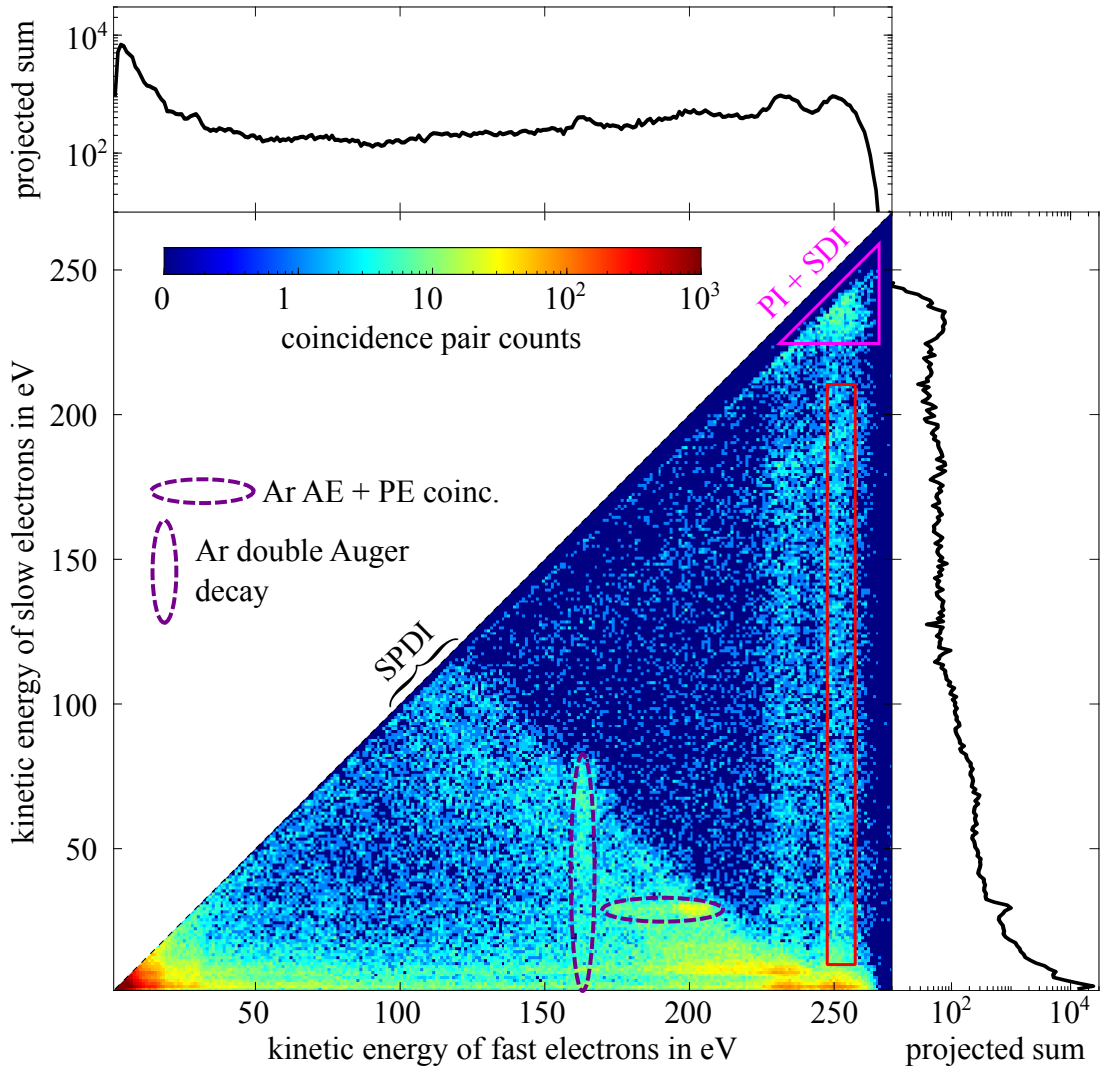

Figure 49: Photoelectron-photoelectron coincidence map integrated over 175 fs pump-probe delay at E_{ph} = 272.7 eV. A special selective area (red box) has been marked which only takes into account electrons between 10 and 210 eV in order to exclude SDI electrons. The horizontal width of the selection window is (252 ± 5) eV selecting primarily 10a′ photoionization events with some contributions from 9a′ and staying outside the lower left SPDI electron area. (The color scale is capped at 10^3; the highest point has 3778 counts.) The increasing gap between the auto-coincidence diagonal and the curve of coincidences with closest matching E_{kin} is a result of detector deadtime.

3.5.3 Photoelectron-photoelectron-photoion covariance

The most relevant ionic interaction product when studying the longevity of electronic quantum coherences in glycine molecules is the intact mother ion, since fragmentation involves the motion of nuclei. In the following, only events were selected which included at least one electron from

the 10a′ orbital (247 to 257 eV at $E_{\mathrm{ph}} = 272.7\,\mathrm{eV}$), at least one Auger electron without SDI contributions ($10\,\mathrm{eV} < E_{\mathrm{kin}} < 210\,\mathrm{eV}$) and at least one Gly^{2+} ion ($m/q = (37.5 \pm 4)\,\mathrm{u}/e$). The above kinetic energy selection also excludes electrons resulting from excitation of a C 1s state to a Rydberg state by the pump pulse followed by Auger decay of the core-excited neutral Gly even without interaction with the probe pulse as well as subsequent valence or Rydberg photoionization by the probe pulse. In order to distinguish between pure coincidences and the multi-particle electron events correlated with the detection of glycine in its final ionic charge state (Gly^{2+}), the abbreviation PEPEPICOV[26] instead of PEPEPICO[27] is introduced for this work. Covariance counting was favored over coincidences, because of the increased occurrence of multiple events per shot and only 40–60% detector efficiency, otherwise resulting in too many false coincidences. The number of detected electrons per pulse as a function of pulse energy is depicted in the Appendix 5.7. In order to primarily evaluate events from single-mode SASE pulses, only those with pulse energies below 2 µJ have been selected.

Out of 1.56×10^7 FEL light pulses, 12.2% featured any number of events. Combining the 2.2×10^6 detected ions and 2.56×10^6 electrons leaves 7.2×10^4 PEPICOV (including 3.2×10^4 PEPEPICOV) events, of which roughly 13% can be attributed to Gly^{2+}. After selecting the kinetic energy ranges of the electrons as described above, only 460 events remain for the glycine dication. Furthermore, selecting only FEL pulses with pulse energies below 2 µJ results in 116 events. Afterward, a moving average over 11 delay steps (10.2 fs) is applied and the maximum is scaled to unity. Finally, this selective yield is divided by the yield over the full kinetic electron energy range which has been treated by the same procedure, in order to eliminate FEL fluctuations similar to Section 3.2. The result is shown in Figure 50.

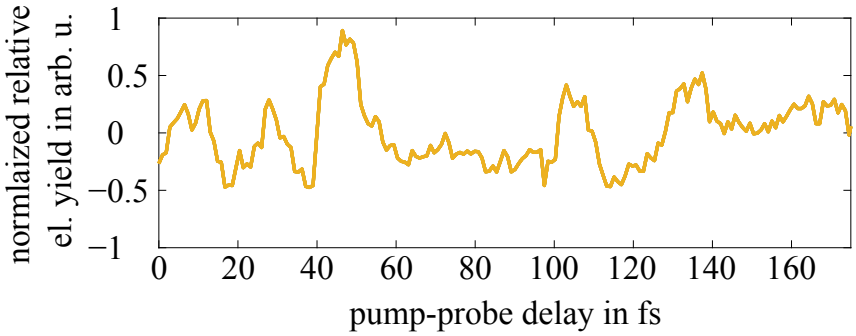

Figure 50: Delay dependent electron yield over 175 fs pump-probe delay covariant with selected Gly^{2+} ions from Figure 45. Only covariance events of electrons with $247 < E_{\mathrm{kin},1} < 257\,\mathrm{eV}$ and $10 < E_{\mathrm{kin},2} < 210\,\mathrm{eV}$ are considered and are normalized and set in relation to the overall yield (see text).

At first glance, the above signal exhibits a pronounced oscillation during the first ~60 fs only. In order to better understand the dynamic oscillation period and its amplitude evolution a time-frequency distribution was produced using the CWT with Airy wavelets as described in

[26] photoelectron-photoelectron-photoion-covariance
[27] photoelectron-photoelectron-photoion-coincidence

Section 1.7. The oscillation frequencies were converted to periods for better comparability, (see Figure 51).

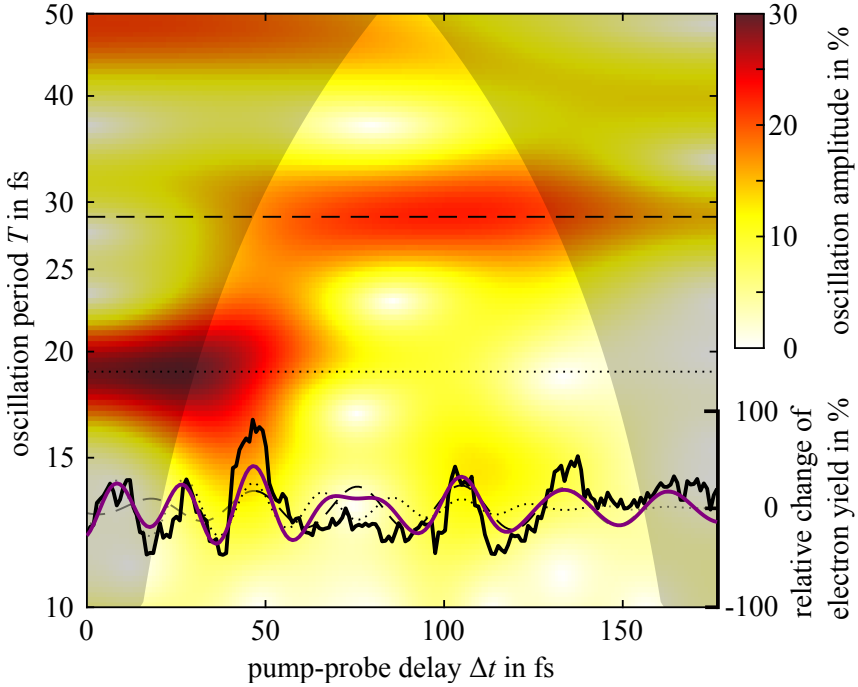

Figure 51: Time-period distribution of correlated Gly^{2+} ions and $247 < E_{kin,1} < 257\,eV$ and $10 < E_{kin,2} < 210\,eV$ electron multi-particle events. The original signal is overlaid in black. The two significant oscillations are reconstructed using the amplitude along the horizontal dashed and dotted lines. The superposition of both reconstructions is given in violet.

The Gly^{2+} dication and covariant photoelectron yield shows a beating pattern and transition from (18.9 ± 3.0) fs to (29.0 ± 4.0) fs as evidenced by the time-period analysis. The periods and 1 standard deviation (SD) values were obtained by fitting a normal distribution to the peak in the first 50 fs and the peak between 75 to 175 fs respectively, as seen in Figure 52. The certainty of these periods is also dependent on the utilized wavelet parameters since they control the trade-off between frequency (period) and time resolution, as well as frequency (period) range and the extent of the COI. Choosing a larger value for the time-bandwidth product results in smaller uncertainties but decreases the upper limit of the period range and simultaneously increases the extent of the COI. The extracted central periods are indicated in Figure 51 throughout the full pump-probe delay range. It can also be seen, that the maximum at $T = 18.9$ fs slightly shifts toward a 20 fs period after the first ~50 fs time delay, where its amplitude declines, which is attributed to the rising edge of the 29 fs oscillation.

The experimental data can be reasonably well reconstructed by the superposition of two sine curves, each with a constant period and phase, but varying amplitude derived from the time-period distribution, as shown in Figure 51.

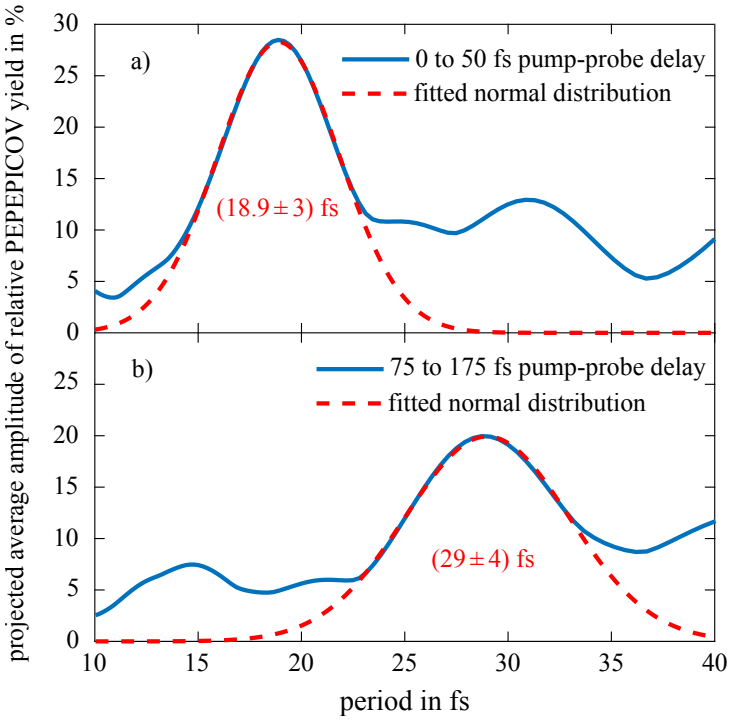

Figure 52: Projection of the time-period distribution of Gly^{2+} ions and $247 < E_{\mathrm{kin},1} < 257\,\mathrm{eV}$ and $10 < E_{\mathrm{kin},2} < 210\,\mathrm{eV}$ electrons for two different pump-probe delay ranges. A normal distribution is fitted to each respective maximum and the mean and standard deviation are indicated.

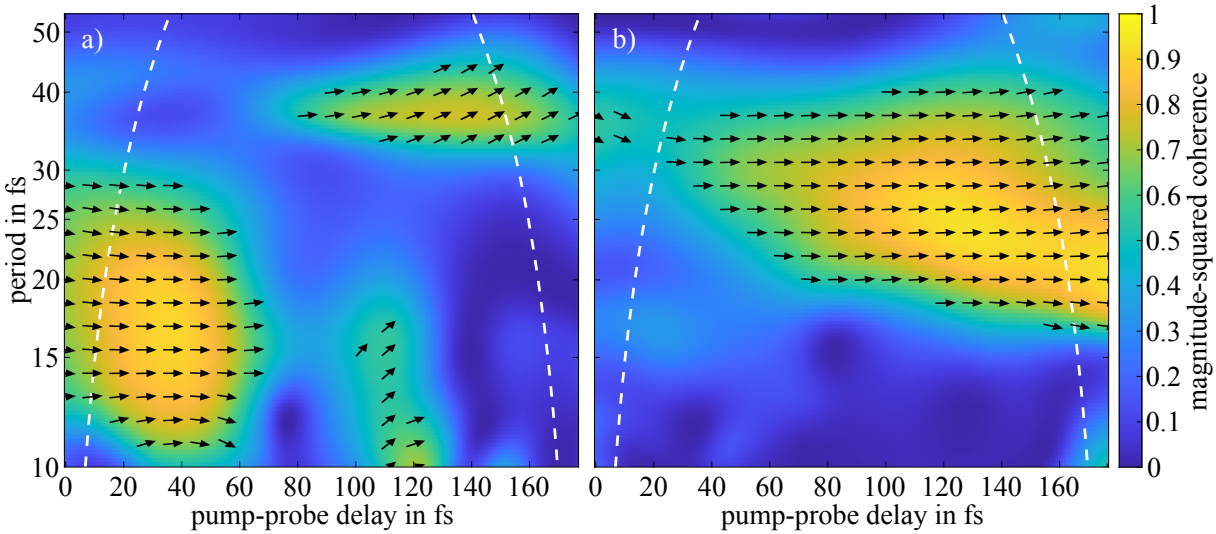

Figure 53: Correlation between the measured signal and a 18.9 fs period oscillation with phase $\varphi_{18.9\,\mathrm{fs}} = -0.44\pi$ **(a)**; a 29.0 fs period oscillation with phase $\varphi_{29.0\,\mathrm{fs}} = 1.27\pi$ **(b)** with amplitudes from the time-period distribution. The black arrows represent the phase difference between the two respective correlated signals where the magnitude-squared coherence is above 0.5. An arrow to the right represents a phase difference of zero and an upward pointing arrow a phase difference of $\pi/2$, *etc.* The white dashed lines mark the cone-of-influence where edge effects are prone to appear.

The phases used are $\varphi_{18.9\,\mathrm{fs}} = -0.44\pi$ and $\varphi_{29.0\,\mathrm{fs}} = 1.27\pi$, respectively. The simple sine curves and their superposition are shown together with the measured signal in Figure 51 and

illustrate the occurrence of a maximum at ~45 fs pump-probe delay followed by a flat amplitude at around 70–85 fs. The beating period between the two oscillations is $T_{\text{beat}} = (54 \pm 39)$ fs. Figure 53 shows the correlation between the individual sine curves with delay-dependent amplitudes and the input signal in a magnitude-squared wavelet coherence plot using the Morlet wavelet [111]. Black arrows indicate the relative phase between the individual reconstructed sine and the measured signal, where there is a strong correlation between the two. It can be seen, that the phases stay completely constant at pump-probe delays where their respective amplitude is strong. The full study reveals, that the $T = 18.9$ fs oscillation does exhibit variations of its phase, where the relative yield amplitude drops below 10% and the phase is therefore difficult to calculate properly, while the amplitude of the $T = 29.0$ fs oscillation never drops below 10% and the oscillation shows a constant phase. Since the amplitude in said regions is too low to properly estimate the phase, the phase variations in return are negligible and the simple reconstruction over all pump-probe delays is valid.

The oscillation amplitudes along the dashed and dotted lines in Figure 51 are shown separately in Figure 54. The amplitude of the oscillation with $T = (18.9 \pm 3.0)$ fs generally decays exponentially[28] with a decay constant of $\tau_{1/e} = (46 \pm 8.9)$ fs within 1 SE, defining the timespan during which the electronic coherence will be lost. Extrapolating the fit to $\Delta t = 0$ fs would result in a maximum relative yield change of (54 ± 10)%

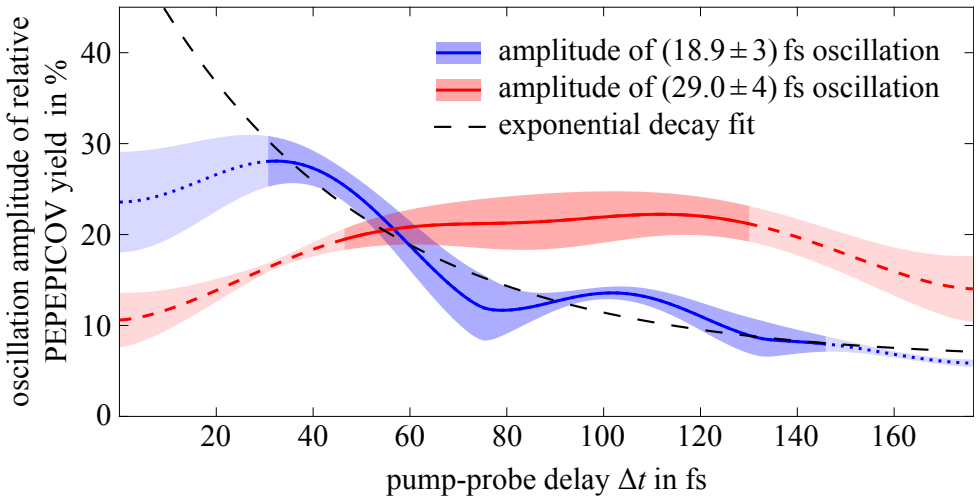

Figure 54: Gly^{2+} ions and $247 < E_{\text{kin},1} < 257$ eV and $10 < E_{\text{kin},2} < 210$ eV electrons PEPEPICOV oscillatory yield amplitudes. The shaded areas represent the averaged amplitude values within ±1 SE around the respective central periods. Less emphasis (light shaded areas) is placed on the pump-probe delays within the COI of the CWT. The exponential decay fit excludes the COI and has an initial amplitude of (54 ± 10)% and decay constant of (46 ± 8.9) fs.

Concurrently, the oscillation with $T = 29.0$ fs rises during the first 100 fs and declines afterward. This oscillation can be attributed to C–C stretch vibrations of the glycine cation, due to the coupling of electronic to nuclear motion with time. Thus, the enhanced formation of vibra-

[28] Exponential decay is not fundamentally inherent to electronic decoherence, but was chosen here as an all-purpose model.

tionally excited molecules with time supports probe-induced photodissociation (at the C-–C link) of glycine molecules once the electronic coherence has decayed and the deposited energy is transferred to nuclear degrees of freedom. This explains the minimum of the intact Gly^{2+} yield derived from Figure 46 in the delay range between 25 and 100 fs. After ~100 fs, vibrational relaxation reduces the likelihood of C–C bond breaking. Thus, the yield of intact Gly^{2+} (or semi-intact Gly^{2+}, missing only H/H_2) rises again (see Figure 46). This overall trend is also reflected by the decreasing amplitude of the nuclear wave packet observed for long time delays in Figure 54. Figure 55 isolates the Gly^{2+} yield from Figure 46 using the same mass-to-charge ratio range as the previous analysis. Using a narrower m/q range only minimally affects the result but linearly decreases the percentage value derived for the relative abundance of doubly charged mother ions.

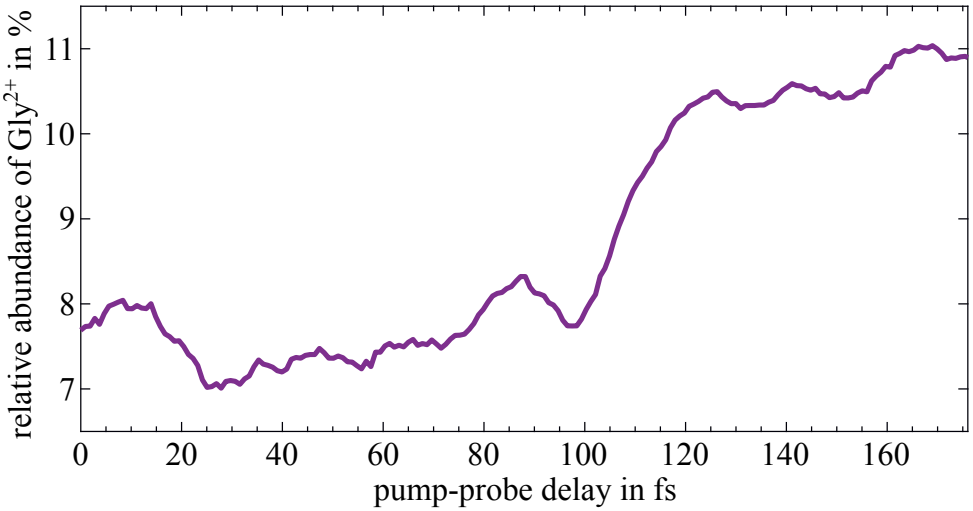

Figure 55: Pump-probe delay dependent yield of Gly^{2+} ions ($m/q = (37.5 \pm 4)$ u/e) as a percentage of the overall ion yield without electron considerations. A moving average over 10.2 fs is applied to the 0.93 fs-binned data.

The phase and period of the electronic coherence monitored at early times by means of resonant, probe-induced Auger decay agree well within the margins of error with the independent findings for off-resonant excitation presented in Figure 41. The latter values of $T = (18.1 \pm 0.7)$ fs and $\varphi = (-0.2 \pm 0.3)\pi$ for the electronic kinetic energy range of 244 to 264 eV are very similar to the on-resonance Auger channel $T = (18.9 \pm 3.0)$ fs and $\varphi = -0.44\pi$ for the range of 247 to 257 eV in covariance with the second electron and ion.

It should be noted, that νC=O stretching has a similar oscillation period of 18.7 fs [73] as the initial 18.9 fs in Figure 51. However, no anticyclic yield variation could be found between the intact Gly^{2+} selective ion channel and any of the C=O bond breakage products, nor the kinetic energy channel of the 7a′ orbital corresponding to the O_C atom. Furthermore, the *ab initio* calculations by Ruberti confirm that the pump ionization coherently populates several electronic states and therefore electronic excitations should be considered primarily. An additional coherent nuclear motion cannot be ruled out by the simulations but would merely provide an correction

on top of the purely electronic coherence and does not change the initial coherent oscillation. At the moment, the magnitude of this correction can only be estimated by comparing the nuclear position-averaged electronic theory to experiments, rather than by a direct full calculation.
Only after the decoherence time τ vibrational excitations are expected due to non-adiabatic coupling. As such it was shown, that the coupled vibrational mode of C–C instead of C=O stretching, in this case, depends more on physical proximity to the charge migration and not necessarily on the similarity in energy quanta, i.e., oscillation period.

3.5.4 Fragmentation dynamics: first insights

Apart from the Gly^{2+} ion, two further species of cationic fragments exhibit x-ray induced delay dependent PEPEPICOV yield dynamics. Namely H^+ (0.8–2 u/e) and H_2^+ (1.2–2.6 u/e) and the group of NH_2^+, O^+, OH^+, H_2O^+ (15.6–22.5 u/e). While the latter group also includes Ar^{2+} ions from the residual gas, their contributions in the selected kinetic energy region of the electrons is again several orders of magnitude lower due to the coincidence condition.

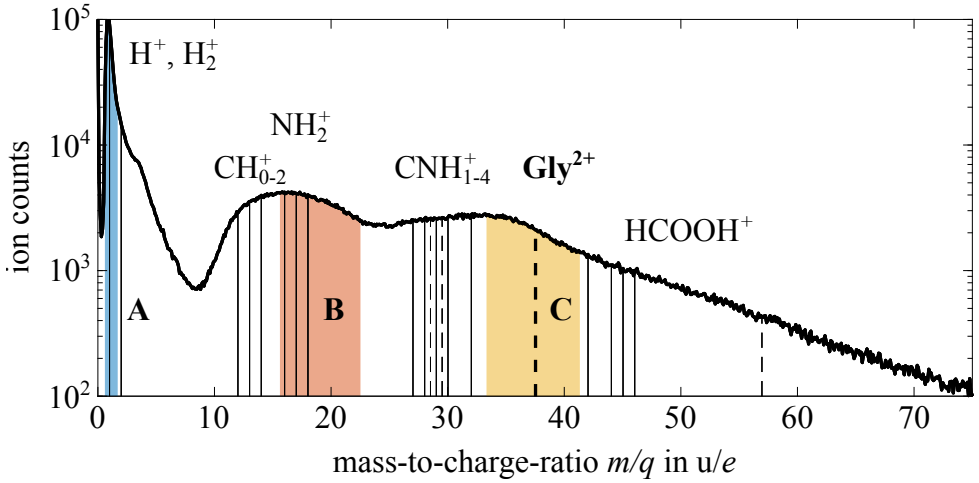

Figure 56: Mass-to-charge spectrum of the glycine mother ion and fragments at E_{ph} = 272.7 eV and averaged over all delays of Δt = 0 to 175 fs. Vertical lines mark the mass-to-charge ratio of common fragments. The right-hand edge of the spectrum corresponds to Gly^+. The ranges **A** (H^+) and **B** (NH_2^+, O^+, OH^+, H_2O^+) will be evaluated more thoroughly. For the range **C** (Gly^{2+}) please refer to Section 3.5.3.

Figure 56 shows the mass-to-charge ratio ranges for all three species and Figure 57 gives the relative multi-particle covariance yield change. The Gly^{2+} range and yield is plotted again for comparison purposes. All spectra have been treated by the same normalization process as described in Section 3.5.3 and use the same electron kinetic energy selection as before, i.e., the analysis is focused on glycine fragmentation dynamics following 10a′ photoionization.
It can be seen, that the H^+ yield variation is somewhat in phase with the one of Gly^{2+} during the first 60 fs although showing a slightly different time period, while NH_2^+/H_2O^+ is not synchronized. What follows is a short presentation and explanation of the involved electron and nuclear dynamics of the individual findings albeit not substantiated by theoretical calculations.

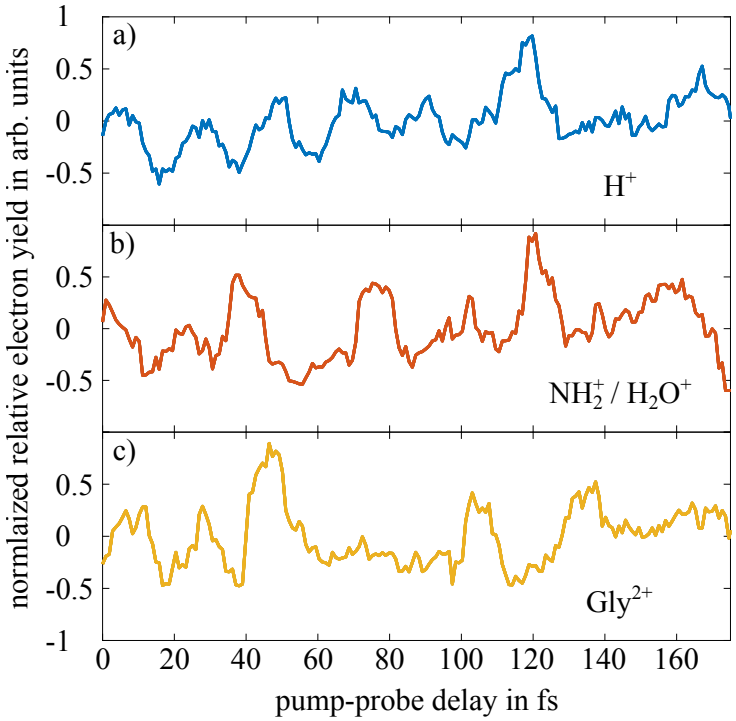

Figure 57: Delay dependent electron yield over 175 fs pump-probe delay covariant with selected ions from Figure 45. Only covariance events of electrons with $247 < E_{\mathrm{kin},1} < 257$ eV and $10 < E_{\mathrm{kin},2} < 210$ eV are considered and are normalized and set in relation to the overall yield.

H^+ and H_2^+ PEPEPICOV yield

The electron yield covariant with H^+ ions exhibits an oscillation with a mainly 23.4 fs period closely correlated to CH_2 bending (δCH_2, [73]) and which slightly diminishes after the first ~80 fs. The H_2^+ signal amplitude on the other hand mainly picks up at later delays and shows a strong 23.8 fs period oscillation which relates to CH_2 bending (δ) and wagging (ω). It also includes a weaker $T_2 \approx 12$ fs contribution which coincides with νCH_2 stretching periods [73]. The detected H^+/H_2^+ ions with the electron signal sensitive to C 1s probe pulse absorption ($5a' \rightarrow 10a'$) likely originate from the $-C_\alpha H_2-$ moiety, where the hole state localizes and the resonant absorption can take place before any other fragmentation of the molecule. For short time delays vibronic coupling is still weak and predominantly only one H atom can be photodissociated. Whereas for the H_2^+ yield stronger C–H_2 vibrations either excited through direct vibrational coupling or intermediate C–C stretching modes and subsequent thermalization play a significant role. Figure 58a) and b) show the time-period distribution for H^+ and H_2^+ yield variations, respectively. A figure showing the combined signal and time-period distribution can be found in the Appendix 5.8.

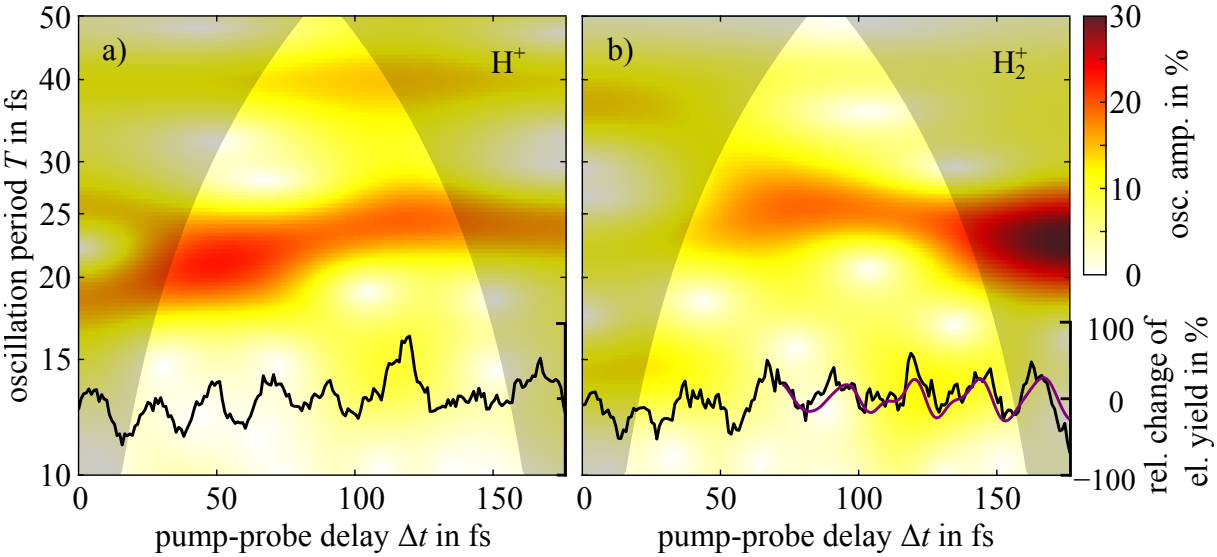

Figure 58: Time-period distribution of H^+ ions **(a)**; H_2^+ ions **(b)** and $247 < E_{\mathrm{kin},1} < 257\,\mathrm{eV}$ and $10 < E_{\mathrm{kin},2} < 210\,\mathrm{eV}$ electrons. The original signal is overlaid in black. For the H_2^+ ions, a reconstructed signal based on two sine curves with constant periods $T_1 = 23.8\,\mathrm{fs}$, $T_2 = 12.2\,\mathrm{fs}$ and constant phases $\varphi_1 = 0.54\pi$, $\varphi_2 = 0.73\pi$ and dynamic amplitudes from the time-period distribution is partially overlaid in violet for the relevant pump-probe delays to emphasize the contribution of the 12.2 fs period.

NH_2^+ and H_2O^+ PEPEPICOV yield

The ionization fragments including NH_2^+, O^+, OH^+ and H_2O^+ contain both a 20.6 fs and strong 39.4 fs component covering the first ~130 fs.

The fragments occurring in this range of the ToF mass spectrum are products from both discussed fragmentation pathways (C–C bond breaking or water elimination, see Figure 48) which makes interpretation of the oscillation modes difficult. Slower, delayed oscillations can be generally attributed with intramolecular degrees of freedom.

According to Rosado *et al.* (1998) there exists a prevalent vibrational mode with a period of 41.7 fs mainly consisting of νC–C stretching (45% contribution) and ωNH_2 rotation (13%). Another vibrational mode with intermediate intensity consisting of ωNH_2 (46%), νC–C (17%) and δNH_2 (16%) has a period of 37.8 fs [73].

The 20.6 fs oscillation shown in Figure 59 likely does not relate to electronic coherences as it is present for over 130 fs but instead it might relate to NH_2 bending (δNH_2 (71%), ωNH_2 (24%)) with a period of 20.5 fs [73]. νC=O stretching has a similar period of 18.7 fs [73] and might be enabled in this selective ion channel after the electronic decoherence time, requiring coherent vibronic coupling. All of the values from [73] are for neutral glycine, which still hold true for the singly ionized molecule as long as no vibrational coupling has occurred. The involvement of NH_2 and to a lesser degree O^+, OH^+ and H_2O^+ in both the ion channel and the related vibrational modes implies that the oscillatory yield pattern is a result of protonation likelihood based on the oscillatory intramolecular –H$\cdots$O– proximity. It has yet to be resolved whether each of the two oscillations can be attributed to a particular fragment. It is so far also

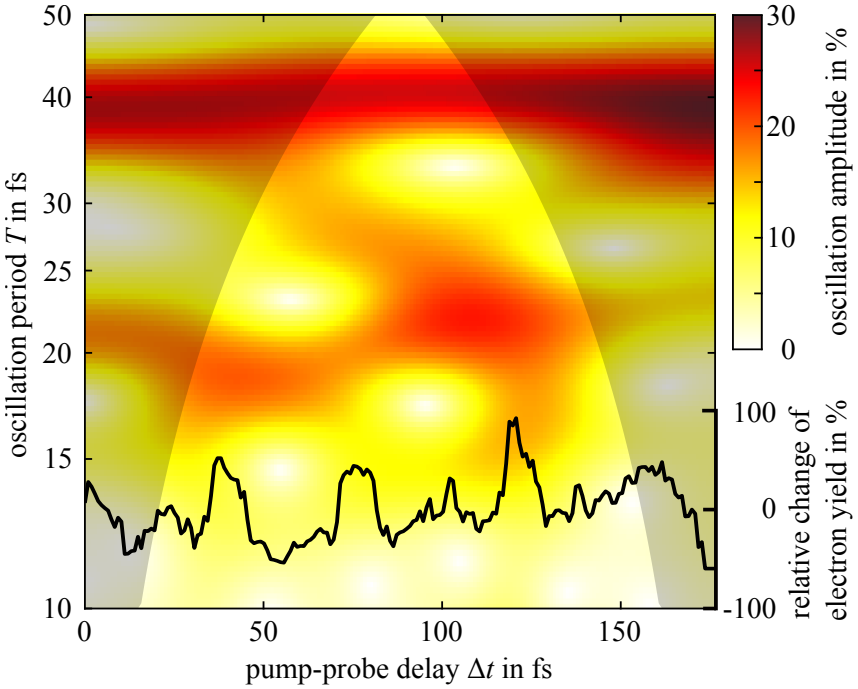

Figure 59: Time-period distribution including mainly NH_2^+, but also O^+, OH^+ and H_2O^+ ions and $247 < E_{kin,1} < 257$ eV and $10 < E_{kin,2} < 210$ eV electrons. The original signal is overlaid in black.

unclear what role the resonant C 1s to inner valence excitation, for which the electron channel is sensitive, plays in the protonation process. I believe that these experimental findings will prove beneficial for the development of theoretical treatments of the interplay between electronic states and nuclear degrees of freedom.

4 Conclusion

From the point of view of enabling technologies, this work substantiates that split-and-delay units are a versatile tool for studying molecular dynamics on a wide range of timescales. The use of short wavelengths, i.e., high photon energies requires an all-reflective approach with reduced transmission, therefore requiring high brilliance FELs. The FEL bandwidth was found to be about 1 eV around the central photon energy of 273 eV. The presented grating-mirror based SDU offers improved focal properties regarding phase contrast and spatial coherence compared to conventional split half-mirror SDUs. The use of fast active stabilization further improves the phase contrast, allows for integrative measurements over prolonged times and substantially shortens the time required for analysis and sorting of the delays. Additionally, replacing the ADC for recording the electronic signal of the MBES with a TDC allows for real-time viewing of photoelectron and photoion spectra.

4.1 Summary

By using a single-color XUV pump-probe scheme, it was shown that electronic quantum coherences of the 10a′ MO of glycine survive for $\tau_{1/e} = (52 \pm 2.8)$ fs. The oscillation period was found to be (18.5 ± 1.7) fs averaged over two independent measurements using two independent methods of analysis, which relates to a level splitting of 220^{+25}_{-18} meV within one propagated standard error. These findings are in good agreement with numerical simulations. Furthermore, two kinetic energy regions, 223 to 245 eV and 246 to 264 eV, could be identified which exhibit anticyclic yield variations in the case of off-resonant excitation.

The above results are valid for a mixture of mainly Gly I and Gly III at a ratio of about 2:1. Other conformers contribute less than 10% each.

It was shown that the 9a′ band and 11a′/12a′ level splitting could also be coherently excited by the spectral bandwidth of the FEL albeit with a lower population weight than 10a′. The simulations have proven that these additional contributions have a similar oscillation period of the yield variation but smaller amplitude.

By observing the photoelectrons in coincidence with photoions it could be revealed that localized, coherent molecular vibronic dynamics settle in as the electronic coherence decays and reach their maximum at ∼105 fs. The nuclear wave packet dynamics further thermalize after 2–3 periods. The characterized vibronic mode of (29.0 ± 4.0) fs is tentatively attributed to C–C stretching vibrations, which is followed by characteristic fragmentation patterns. First insight into the underlying processes has been gained from the corresponding data evaluation.

Last, but not least, a further step toward charge-directed reactions in glycine has been achieved, by observing the increased creation of intact glycine dications and radical fragments at specific pump-probe delays.

4.2 Outlook

4.2.1 Future scientific questions

A major goal of ultrafast spectroscopy is the study of electron dynamics and charge transfer on atto- to nanosecond timescales and the gain of a detailed understanding of ever larger, biologically relevant, complex molecules. Such information can be used to optimally control, direct or prohibit unprecedented chemical reactions or those so far only found in nature. More specifically, ultrafast charge dynamics in larger, aromatic amino acids such as i.e., phenylalanine [24], tryptophan [25] and tyrosine [12] have already been studied by Calegari *et al.* at photon energies between 15 and 35 eV. Due to the experimental challenges, studies requiring high intensities and photon energies[29] on amino acids and other bio-relevant molecules are still pending. Alternatively, amino acid chains are of great interest as they are key to protein–protein cross-links and DNA damage or repair [12]. One such molecule related to the present work is Gly–Gly–NH–CH_3, for which electron charge dynamics on a 5–6 fs scale have been predicted by Kuleff and Cederbaum *et al.* [112] or [113]. However, a detailed experimental pump-probe scheme has yet to be conceived. One experimental hindrance that arises for larger biological samples, is either earlier thermal decomposition at high evaporation/sublimation temperatures or insufficient target densities at decreased temperatures.

4.2.2 Technical improvements

During the 2 years between the two experimental campaigns many improvements were added to the experimental setup. With further additions also new complications emerged.
As stated in Section 2.2.6, due to the nature of the reference arm of the PicoScale interferometers an expansion of the U-bracket due to slow thermal drifts results in drifts of the measured displacement d and calculated vertical angle of the movable grating-mirror leading to erroneous overcorrection. The horizontal angle remains unaffected because of symmetry. Thermal drifts occur most notably during sunrise and sunset, wasting valuable FEL runtime. Furthermore, the absolute zero position had to be re-established after each drift, which also halts a continuous operation.
One solution would be to measure the temperature of the aluminum holder and calculate the thermal expansion and its effect upon the positional measurements. An alternative countermeasure, an additional fifth, HeNe laser interferometer, has already been installed and tested in order to measure the slow drifts and correct the PicoScale data. This interferometer can be switched in, in place of the WLI, after initial determination of time zero and for feedback-control at 10 Hz.

[29] Note, inner-valence hole formation in the present work is still possible at ionization energies of about 20 eV. Only the detection scheme requires high photon energies for resonant core level excitation and to unambiguously differentiate between the MOs.

The reflectivity of the grating-mirrors and thereby the FEL intensity in the interaction volume with the sample can be further improved by using longer gratings to allow for a shallower grazing incidence angle and simultaneously use a larger footprint on the grating. Thereby, higher intensities in the interaction zone can be achieved while beam damage of the gratings will be suppressed. Current activities revolve around doubling the effective width of the gratings.
Furthermore, as a side effect of replacing the linear actuators controlling the pitch and yaw angle of the movable grating-mirror, a sizable improvement of the transmission of the device can be achieved. For the time being, the torsion return springs were replaced by weaker ones with the same diameter to reuse the machined frames. However, springs of similar strength with a smaller diameter are sold by the same manufacturer which would allow for a smaller profile suspension and halving the minimum incidence angle. Rebuilding the vacuum chambers and acquiring a new toroidal focusing mirror could nearly double the current throughput.
Another important goal is advancement toward smaller lamellas at preserved surface quality and flatness. This would allow for shorter focal lengths required for separating the diffraction orders at short wavelengths and a shorter Rayleigh length and smaller beam waist. A thereby gained substantial increase in intensity in the focus allows for the time-resolved study of non-linear processes.

On a final note, let it be said, that the advancement of two-color x-ray pump/x-ray probe FEL pulse delivery schemes opens new prospects of measuring and manipulating light-matter interactions in physics, chemistry and biology by doubling the control in site and orbital selectivity. Thus it becomes possible to induce electronic dynamics on a specific atomic constituent with high element specificity provided by the soft x-rays of a particular color and to probe the dynamics at a different site/element as a function of time delay with a probe pulse of different color. In recent developments, two-color FEL pulses could be generated using an undulator with alternately tuned segments for the two different wavelengths. When part of the electron bunch traverses an out-of-tune segment the respective FEL process stops but bunching still occurs. The in-tune part generates radiation based on the undulator parameter[30]. This has first been demonstrated at the Linac Coherent Light Source (LCLS) [116] and recently at DESY. Still, the challenge remains to tune the reflectivity of the individual gratings in the split-and-delay unit to each of the two colors.

[30]Other modes of generating two-color pulses are, in a non-exhaustive list, using two electron packages of different kinetic energy with variable time delay in the same undulator [114] or using two undulator segments with different periods and, in simple terms, an electron bunch of which half of it lases in the first undulator and the other half in the second. For the latter, the temporal delay can be adjusted by a chicane delaying the whole electron bunch between the two undulators [115].

Appendix

5.1 FEL beam footprint after reflection on the grating-mirrors

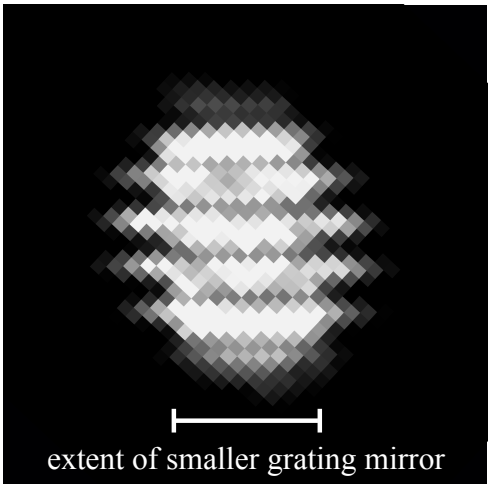

Figure 60: Footprint on a Ce:YAG screen of the nearly collimated FEL beam after being reflected from the SDU grating-mirrors. The width of the apparent grating-mirrors is compressed due to the 8° incidence angle projection. The diffraction orders are not yet separated.

5.2 WLED spectrum

In relation to Section 2.2.2.

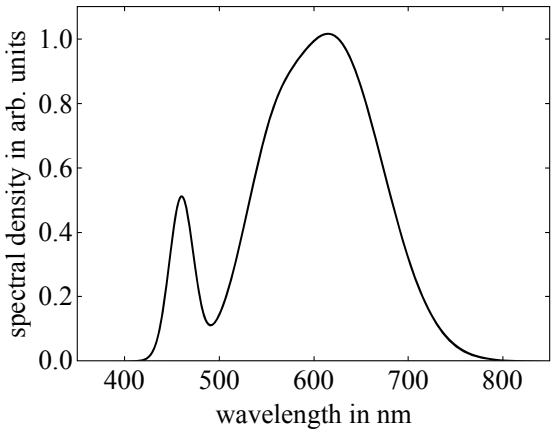

Figure 61: Spectrum of the utilized white-light LED with a central wavelength of 570 nm. Reproduced from [1].

5.3 Ni and Si reflectivity

In relation to Section 2.2.1.

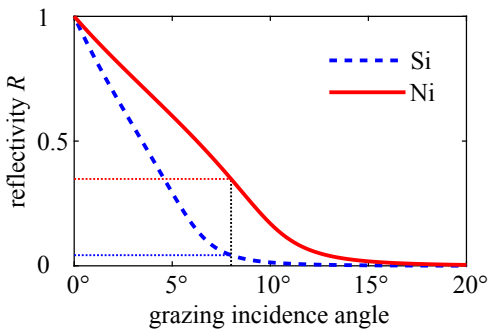

Figure 62: Comparison of Ni and Si reflectivity at variable incidence angle α for a photon energy of 274 eV. At the nominal $\alpha = 8°$, the reflectivity of Ni is 8 times higher than that of Si. Adapted from [93].

5.4 Residual gas spectrum

In relation to Section 3.5.

The two spectra in Figure 63 were recorded at comparable FEL pulse energies and have been corrected for their different measurement durations. The absolute y-scale is dependent on the bin size of the kinetic energy of electrons. Note that the yield of the glycine photoelectrons is more than an order of magnitude greater than the residual gas contributions for the majority of the kinetic energy range. If the coincidence condition is taken into account the relative yield between the two scales quadratically so that the residual gas contributions are at least 2 – 3 orders of magnitude lower, than the glycine signal.

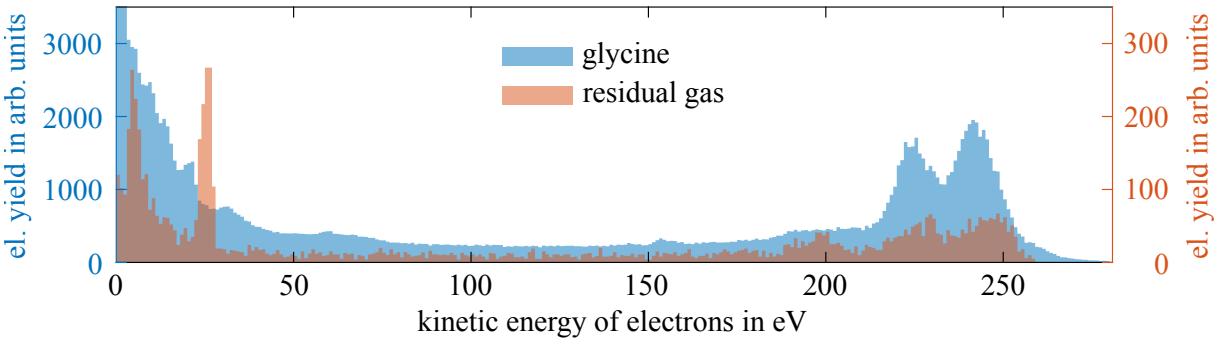

Figure 63: Exemplary glycine and residual gas photoelectron spectra for the second experimental campaign (2020).

5.5 PicoScale calculations

In relation to Section 2.2.6.

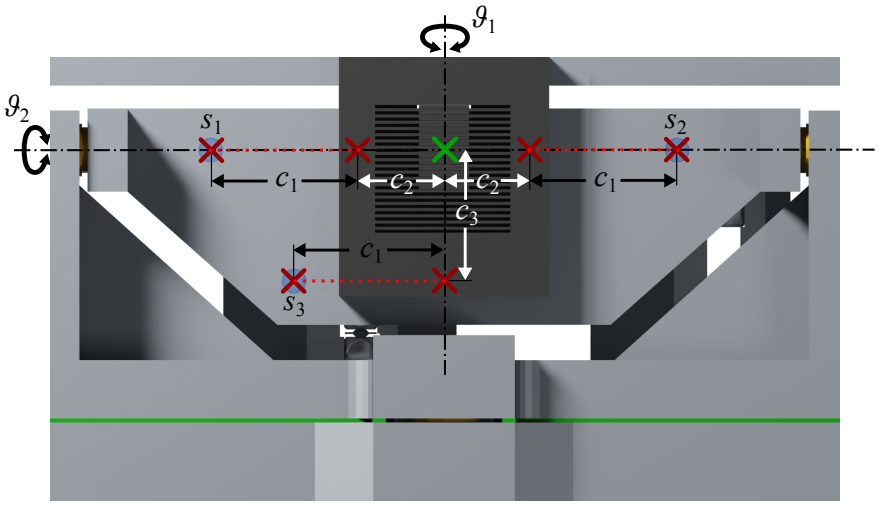

Figure 64: Front view of the SDU with PicoScale dimensions. The green cross marks the center of rotation. The red crosses mark the laser spots of the three differential PicoScale interferometers. The red dotted lines between the red crosses indicate which spots belong to one interferometer unit. $s_{1,2,3}$ are the measurement values of the interferometers; $c_{1,2,3}$ are constants. Each interferometer measures the distance between the fixed grating-mirror and the rotatable holder of the smaller interleaved grating-mirror. The lamella widths are not to scale. Adapted from [84].

5.6 MBES voltages

In relation to Section 2.5.

Electrode	Voltage (2018)	Voltage (2020)
el. MCP back (anode)	+2400	+2000
el. MCP front	−10	0
electron drift tube	−10	0
Ret 4	−10	0
Ret 3	−10	0
Ret 2	0	0
Ret 1	0	0
ion repeller	0	0
capillary	0	0
electron repeller	−100	−50
ion drift tube	−200	−1850
ion MCP front	−200	−1850
ion MCP back	+2200	0
ion MCP back	+2200	0

Table 5: MBES voltage sets used in the Dec. 2018 and 2020 experiments in Volt (V).

5.7 FEL pulse energy distributions

In relation to Section 3.5.3.

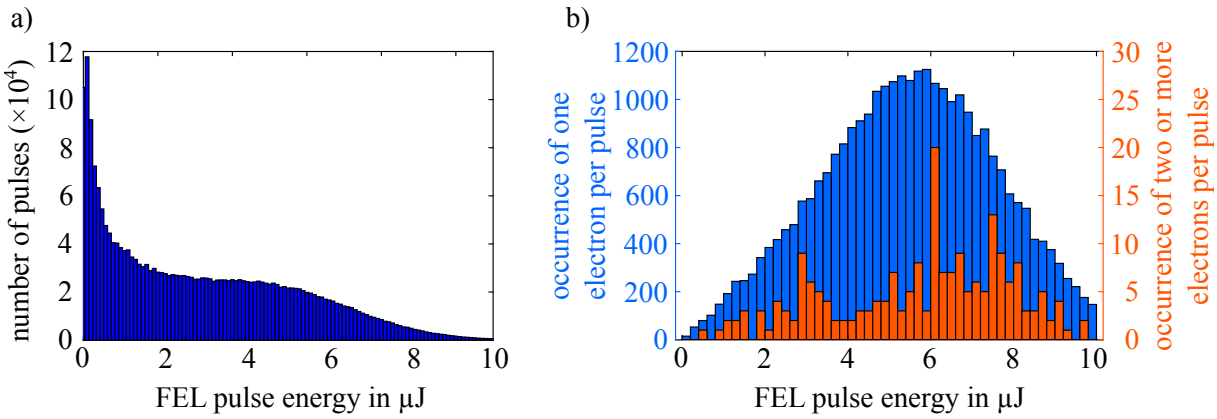

Figure 65: Single-mode SASE FLASH pulse energy **(a)** and photoelectron coincidence histograms for 0 fs pump-probe delay **(b)** (2018). Pulses with three electrons occurred 5 times in total in this instance.

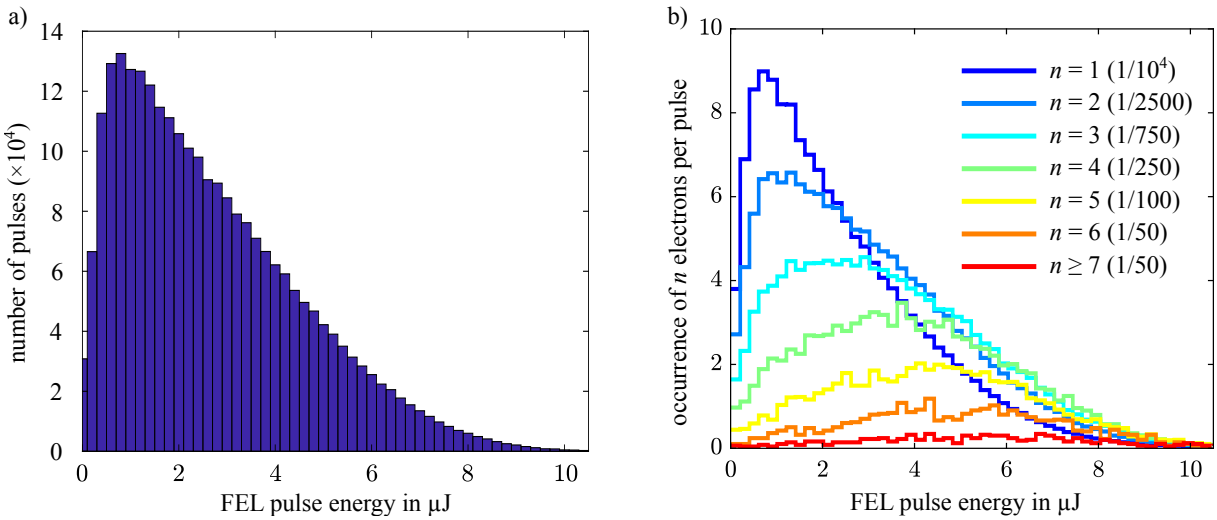

Figure 66: Single-mode SASE FLASH pulse energy **(a)** and photoelectron coincidence histograms for 0 to 225 fs pump-probe delay **(b)** (2020). Different scalings (in brackets) were applied to each line in **(b)**.

Slow charge accumulation on the electrodes and spontaneous discharges leads to shifts and jumps of the spectra over time. Figure 67 shows an example of the average spectral shift versus measurement duration represented by the stepwise linear pump-probe delay. Only the photoelectron spectra have been rectified. Major charge accumulation effects start at 176 fs and as such were discarded.

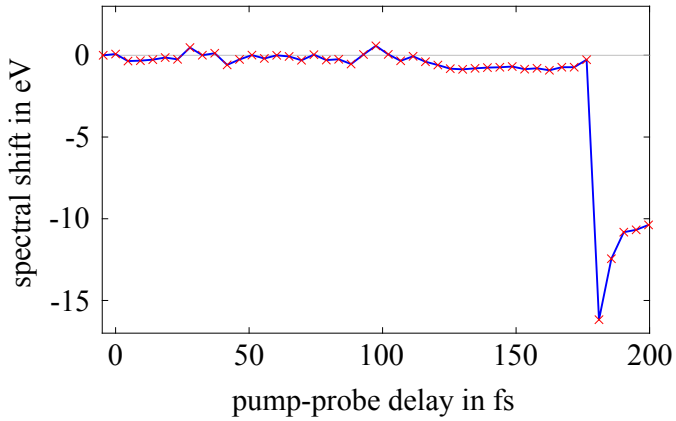

Figure 67: Energy shift of an electron spectrum due to charge accumulation on the MBES electrodes over 4:15 hours. Several delay steps have been grouped to form unambiguous peaks for detection of the energy shift (red crosses). For finer delay dependent corrections a linear interpolation was used (blue line).

5.8 PEPEPICOV Time-period distribution for H^+ and H_2^+

In relation to Section 3.5.4.

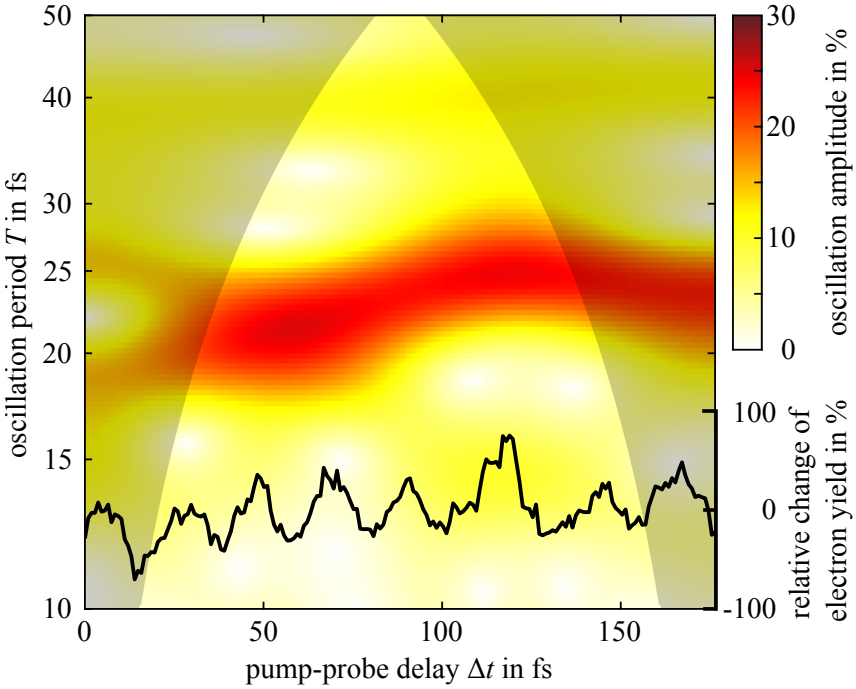

Figure 68: Time-period distribution of H^+ and H_2^+ ions and $247 < E_{\mathrm{kin},1} < 257\,\mathrm{eV}$ and $10 < E_{\mathrm{kin},2} < 210\,\mathrm{eV}$ electrons. The original signal is overlaid in black.

List of own publications

Electronic quantum coherence in glycine molecules probed with ultrashort x-ray pulses in real time
D. Schwickert, M. Ruberti, P. Kolorenč, S. Usenko, A. Przystawik, K. Baev, I. Baev, M. Braune, L. Bocklage, M.K. Czwalinna, S. Deinert, S. Düsterer, A. Hans, G. Hartmann, C. Haunhorst, M. Kuhlmann, S. Palutke, R. Röhlsberger, J. Rönsch-Schulenburg, P. Schmidt, S. Toleikis, J. Viefhaus, M. Martins, A. Knie, D. Kip, V. Averbukh, J.P. Marangos, and T. Laarmann
arXiv:2012.04852v2 [physics.chem-ph]

Full characterization of a phase-locked DUV double pulse generated in an all-reflective shaping setup working under grazing incidence in a broad spectral range
S. Hartwell, A. Azima, C. Haunhorst, M. Kazemi, M. Namboodiri, A. Przystawik, D. Schwickert, S. Skruszewicz, D. Kip, M. Drescher, and T. Laarmann
Appl. Phys. B 128, 2 (2022)

Table-top interferometry on extreme time and wavelength scales
S. Skruszewicz, A. Przystawik, D. Schwickert, M. Sumfleth, M. Namboodiri, V. Hilbert, R. Klas, P. Gierschke, V. Schuster, A. Vorobiov, C. Haunhorst, D. Kip, J. Limpert, J. Rothhardt, and T. Laarmann
Opt. Express 29, 40333 (2021)

Auger electron wave packet interferometry on extreme timescales with coherent soft x-rays
S. Usenko, D. Schwickert, A. Przystawik, K. Baev, I. Baev, M. Braune, L. Bocklage, M.K. Czwalinna, S. Deinert, S. Düsterer, A. Hans, G. Hartmann, C. Haunhorst, M. Kuhlmann, S. Palutke, R. Röhlsberger, J. Rönsch-Schulenburg, P. Schmidt, S. Skruszewicz, S. Toleikis, J. Viefhaus, M. Martins, A. Knie, D. Kip, and T. Laarmann
J. Phys. B 53, 244008 (2020)

References

[1] Sergey Usenko. “Interferometry on small quantum systems at short wavelength”. PhD thesis. Universität Hamburg, 2016.

[2] Sergey Usenko et al. “Split-And-Delay Unit for FEL Interferometry in the XUV Spectral Range”. In: *Applied Sciences* 7.6 (2017). ISSN: 2076-3417. DOI: 10.3390/app7060544. URL: https://www.mdpi.com/2076-3417/7/6/544.

[3] M. Ruberti. “Restricted Correlation Space B-Spline ADC Approach to Molecular Ionization: Theory and Applications to Total Photoionization Cross-Sections”. In: *Journal of Chemical Theory and Computation* 15.6 (2019). PMID: 31136172, pp. 3635–3653. DOI: 10.1021/acs.jctc.9b00288. eprint: https://doi.org/10.1021/acs.jctc.9b00288. URL: https://doi.org/10.1021/acs.jctc.9b00288.

[4] M. Ruberti. “Onset of ionic coherence and ultrafast charge dynamics in attosecond molecular ionisation”. In: *Phys. Chem. Chem. Phys.* 21 (32 2019), pp. 17584–17604. DOI: 10.1039/C9CP03074C. URL: http://dx.doi.org/10.1039/C9CP03074C.

[5] A. Ku et al. “Auger electrons for cancer therapy - a review”. In: *Radiopharmacy and Chemistry* 4 (2019). DOI: doi:10.1186/s41181-019-0075-2.

[6] K. Gokhberg et al. “Site- and energy-selective slow-electron production through intermolecular Coulombic decay”. In: *Nature* 505 (2014), pp. 661–663. DOI: doi:10.1038/nature12936.

[7] L.S. Cederbaum and J. Zobeley. “Ultrafast charge migration by electron correlation”. In: *Chemical Physics Letters* 307.3 (1999), pp. 205–210. ISSN: 0009-2614. DOI: https://doi.org/10.1016/S0009-2614(99)00508-4. URL: https://www.sciencedirect.com/science/article/pii/S0009261499005084.

[8] Elinor Zerah Harush and Yonatan Dubi. “Do photosynthetic complexes use quantum coherence to increase their efficiency? Probably not”. In: *Science Advances* 7.8 (2021), eabc4631. DOI: 10.1126/sciadv.abc4631. eprint: https://www.science.org/doi/pdf/10.1126/sciadv.abc4631. URL: https://www.science.org/doi/abs/10.1126/sciadv.abc4631.

[9] Sergei Savikhin, Daniel R. Buck, and Walter S. Struve. “Oscillating anisotropies in a bacteriochlorophyll protein: Evidence for quantum beating between exciton levels”. In: *Chemical Physics* 223.2 (1997), pp. 303–312. ISSN: 0301-0104. DOI: https://doi.org/10.1016/S0301-0104(97)00223-1. URL: https://www.sciencedirect.com/science/article/pii/S0301010497002231.

[10] Gregory S. Engel. “Quantum coherence in photosynthesis”. In: *Procedia Chemistry* 3.1 (2011). 22nd Solvay Conference on Chemistry, pp. 222–231. ISSN: 1876-6196. DOI: https://doi.org/10.1016/j.proche.2011.08.029. URL: https://www.sciencedirect.com/science/article/pii/S1876619611000684.

[11] Cathal Smyth, Francesca Fassioli, and Gregory D. Scholes. “Measures and implications of electronic coherence in photosynthetic light-harvesting”. In: *Philosophical Transactions of the Royal Society A: Mathematical, Physical and Engineering Sciences* 370.1972 (2012), pp. 3728–3749. DOI: 10.1098/rsta.2011.0420. eprint: https://royalsocietypublishing.org/doi/pdf/10.1098/rsta.2011.0420. URL: https://royalsocietypublishing.org/doi/abs/10.1098/rsta.2011.0420.

[12] Francesca Calegari et al. “Charge migration induced by attosecond pulses in bio-relevant molecules”. In: *Journal of Physics B: Atomic, Molecular and Optical Physics* 49.14 (June 2016), p. 142001. DOI: 10.1088/0953-4075/49/14/142001. URL: https://doi.org/10.1088/0953-4075/49/14/142001.

[13] Hans Jakob Wörner et al. “Charge migration and charge transfer in molecular systems”. In: *Structural Dynamics* 4.6 (2017), p. 061508. DOI: 10.1063/1.4996505. eprint: https://doi.org/10.1063/1.4996505. URL: https://doi.org/10.1063/1.4996505.

[14] Gregory S. Engel. “Quantum coherence in photosynthesis”. In: *Procedia Chemistry* 3 (2011), pp. 222–231.

[15] John C. Hall. “Review: Glycine”. In: *Journal of Parenteral and Enteral Nutrition* 22.6 (1998), pp. 393–398. DOI: https://doi.org/10.1177/0148607198022006393. eprint: https://aspenjournals.onlinelibrary.wiley.com/doi/pdf/10.1177/0148607198022006393. URL: https://aspenjournals.onlinelibrary.wiley.com/doi/abs/10.1177/0148607198022006393.

[16] B. López-Corcuera, A. Geerlings, and C. Aragón. “Glycine neurotransmitter transporters: an update”. In: *Molecular membrane biology* 18(1) (2001). PMID: 11396606, under review, pp. 13–20.

[17] Jamie E. Elsila, Daniel P. Glavin, and Jason P. Dworkin. “Cometary glycine detected in samples returned by Stardust”. In: *Meteoritics & Planetary Science* 44.9 (2009), pp. 1323–1330. DOI: https://doi.org/10.1111/j.1945-5100.2009.tb01224.x. eprint: https://onlinelibrary.wiley.com/doi/pdf/10.1111/j.1945-5100.2009.tb01224.x. URL: https://onlinelibrary.wiley.com/doi/abs/10.1111/j.1945-5100.2009.tb01224.x.

[18] Kathrin Altwegg et al. “Prebiotic chemicals – amino acid and phosphorus – in the coma of comet 67P/Churyumov-Gerasimenko”. In: *Science Advances* 2.5 (2016), e1600285. DOI: 10.1126/sciadv.1600285. eprint: https://www.science.org/doi/pdf/10.1126/sciadv.1600285. URL: https://www.science.org/doi/abs/10.1126/sciadv.1600285.

[19] Y. Zheng, J. J. Neville, and C. E. Brion. “Imaging the Electron Density in the Highest Occupied Molecular Orbital of Glycine”. In: *Science* 270.5237 (1995), pp. 786–788. DOI: 10.1126/science.270.5237.786. URL: https://www.science.org/doi/abs/10.1126/science.270.5237.786.

[20] John J. Neville, Y. Zheng, and C. E. Brion. “Glycine Valence Orbital Electron Densities: Comparison of Electron Momentum Spectroscopy Experiments with Hartree-Fock and Density Functional Theories”. In: *Journal of the American Chemical Society* 118.43 (1996), pp. 10533–10544. DOI: 10.1021/ja9613015. eprint: https://doi.org/10.1021/ja9613015. URL: https://doi.org/10.1021/ja9613015.

[21] Alexander I. Kuleff and Lorenz S. Cederbaum. “Charge migration in different conformers of glycine: The role of nuclear geometry”. In: *Chemical Physics* 338.2 (2007). Molecular Wave Packet Dynamics, pp. 320–328. ISSN: 0301-0104. DOI: https://doi.org/10.1016/j.chemphys.2007.04.012. URL: https://www.sciencedirect.com/science/article/pii/S0301010407001413.

[22] A Sanchez-Gonzalez et al. “Auger electron and photoabsorption spectra of glycine in the vicinity of the oxygen K-edge measured with an X-FEL”. In: *Journal of Physics B: Atomic, Molecular and Optical Physics* 48.23 (Oct. 2015), p. 234004. DOI: 10.1088/0953-4075/48/23/234004. URL: https://doi.org/10.1088/0953-4075/48/23/234004.

[23] Bridgette Cooper et al. “Analysis of a measurement scheme for ultrafast hole dynamics by few femtosecond resolution X-ray pump–probe Auger spectroscopy”. In: *Faraday Discuss.* 171 (0 2014), pp. 93–111. DOI: 10.1039/C4FD00051J. URL: http://dx.doi.org/10.1039/C4FD00051J.

[24] F. Calegari et al. “Ultrafast electron dynamics in phenylalanine initiated by attosecond pulses”. In: *Science* 346.6207 (2014), pp. 336–339. DOI: 10.1126/science.1254061. eprint: https://www.science.org/doi/pdf/10.1126/science.1254061. URL: https://www.science.org/doi/abs/10.1126/science.1254061.

[25] Manuel Lara-Astiaso et al. “Attosecond Pump–Probe Spectroscopy of Charge Dynamics in Tryptophan”. In: *The Journal of Physical Chemistry Letters* 9.16 (2018). PMID: 30044916, pp. 4570–4577. DOI: 10.1021/acs.jpclett.8b01786. eprint: https://doi.org/10.1021/acs.jpclett.8b01786. URL: https://doi.org/10.1021/acs.jpclett.8b01786.

[26] Eberhard J. Jaeschke et al., eds. *Synchrotron Light Sources and Free-Electron Lasers*. 2nd ed. Springer, 2020. ISBN: 978-3-030-23200-9.

[27] N. Hartmann et al. “Attosecond time–energy structure of X-ray free-electron laser pulses”. In: 12 (2018), pp. 215–220. URL: https://doi.org/10.1038/s41566-018-0107-6.

[28] W. Colson. “The nonlinear wave equation for higher harmonics in free-electron lasers”. In: *IEEE Journal of Quantum Electronics* 17.8 (1981), pp. 1417–1427. DOI: 10.1109/JQE.1981.1071273.

[29] E. D. Johnson and J. B. Hastings, eds. *Sources and Applications of High Intensity UV-VUV Light, ACCELERATOR BASED SOURCES OF UV RADIATION*. BNL—45499. NATIONAL SYNCHROTRON LIGHT SOURCE. 1990. URL: https://inis.iaea.org/collection/NCLCollectionStore/_Public/23/043/23043891.pdf.

[30] Jörg Rossbach, Jochen R. Schneider, and Wilfried Wurth. “10 years of pioneering X-ray science at the Free-Electron Laser FLASH at DESY”. In: *Physics Reports* 808 (2019). 10 years of pioneering X-ray science at the Free-Electron Laser FLASH at DESY, pp. 1–74. ISSN: 0370-1573. DOI: https://doi.org/10.1016/j.physrep.2019.02.002. URL: https://www.sciencedirect.com/science/article/pii/S0370157319300663.

[31] Deutsches Elektron-Synchrotron. *From Synchrotron Radiation to a SASE FEL*. URL: https://photon-science.desy.de/research/students__teaching/sr_and_fel_basics/fel_basics/tdr_from_synchrotron_radiation_to_a_sase_fel/index_eng.html.

[32] Peter Schmüser, Martin Dohlus, and Jörg Rossbach. *Ultraviolet and Soft X-Ray Free-Electron Lasers*. Vol. 229. Springer, 2008. ISBN: 978-3-540-79571-1.

[33] Claudio Pellegrini. “EPAC 2006”. In: *X-RAY FREE-ELECTRON LASERS AND ULTRAFAST SCIENCE AT THE ATOMIC AND MOLECULAR SCALE*. 2006. URL: https://accelconf.web.cern.ch/e06/PAPERS/FRYBPA01.PDF.

[34] Avraham Gover et al. “Beating the shot-noise limit”. In: *Nature Physics* 8 (2012), pp. 877–880. ISSN: 1745-2481. DOI: https://doi.org/10.1038/nphys2443. URL: https://www.sciencedirect.com/science/article/pii/S0370157319300663.

[35] *Ninth International Accelerator School for Linear Colliders*. 2015. URL: https://agenda.linearcollider.org/event/6906/sessions/3828/attachments/27990/42384/LCschool-FEL.pdf.

[36] J. Rönsch-Schulenburg et al., eds. *OPERATION OF FLASH WITH SHORT SASE-FEL RADIATION PULSES*. 2014. URL: https://accelconf.web.cern.ch/FEL2014/papers/tub04.pdf.

[37] P. Emma, R. Akre, and J. Arthur. “First lasing and operation of an ångstrom-wavelength free-electron laser”. In: *Nature Photonics* 4 (2010), pp. 641–647. ISSN: 1749-4893. DOI: https://doi.org/10.1038/nphoton.2010.176. URL: https://www.nature.com/articles/nphoton.2010.176.

[38] Bruno Gilles. *GRAZING INCIDENCE DIFFRACTION: A REVIEW*. URL: https://inis.iaea.org/collection/NCLCollectionStore/_Public/28/044/28044557.pdf.

[39] Detlef-M. Smilgies. *Grazing-Incidence Small-Angle Scattering (GISAXS)*. 2017. URL: https://www.classe.cornell.edu/~dms79/gisaxs/tutorial/SAXS-Guide-Smilgies.pdf.

[40] B. Raj and C. B. Rao. “Study of engineering surfaces using laser-scattering techniques”. In: *Sadhana* 28 (2003), pp. 739–761. DOI: https://doi.org/10.1007/BF02706457. URL: https://link.springer.com/content/pdf/10.1007/BF02706457.pdf.

[41] Daniele Cocco. “X-ray Optics”. In: *Synchrotron Radiation & Free Electron Lasers*. Sincrotrone Trieste ScpA. 2011.

[42] *Proceedings of the Cambridge philosophical society, Vol. XVII. Part 1*. 1913.

[43] Wallace Glab. *What’s a Rydberg state, anyway?* 1997. URL: http://www.phys.ttu.edu/~gglab/rydberg_state.html.

[44] Thomas Gallagher, ed. *Springer Handbook of Atomic, Molecular, and Optical Physics*. Springer-Verlag New York, 2006. ISBN: 978-0-387-20802-2. DOI: 10.1007/978-0-387-26308-3_14.

[45] D. C. Haynes et al. “Clocking Auger electrons”. In: *Nature Physics* 17 (2021), pp. 512–518. DOI: 10.1038/s41567-020-01111-0. URL: https://doi.org/10.1038/s41567-020-01111-0.

[46] Yongjun Li et al. “Effects of single-photon double photoionization and direct double Auger decay on K-shell ionization kinetics of Ar atoms interacting with XFEL pulses”. In: *Journal of Physics B: Atomic, Molecular and Optical Physics* (2022). URL: http://iopscience.iop.org/article/10.1088/1361-6455/ac4ccf.

[47] S. Huotari et al. “Intrashell Electron-Interaction-Mediated Photoformation of Hollow Atoms near Threshold”. In: *Phys. Rev. Lett.* 101 (4 July 2008), p. 043001. DOI: 10.1103/PhysRevLett.101.043001. URL: https://link.aps.org/doi/10.1103/PhysRevLett.101.043001.

[48] Louis de Broglie. “A Tentative Theory of Light Quanta”. In: *Philosophical Magazine* 47 (1924), pp. 446–458.

[49] Wenxiang Hu, Bing Gu, and Ignacio Franco. "Lessons on electronic decoherence in molecules from exact modeling". In: *The Journal of Chemical Physics* 148.13 (2018), p. 134304. DOI: 10.1063/1.5004578. URL: https://doi.org/10.1063/1.5004578.

[50] Yulei Shi and Li Wang. "Collective vibrational spectra of α- and γ-glycine studied by terahertz and Raman spectroscopy". In: *Journal of Physics D: Applied Physics* 38.19 (Sept. 2005), pp. 3741–3745. DOI: 10.1088/0022-3727/38/19/024. URL: https://doi.org/10.1088/0022-3727/38/19/024.

[51] Kinya Iijima, Kumiko Tanaka, and Shigeki Onuma. "Main conformer of gaseous glycine: molecular structure and rotational barrier from electron diffraction data and rotational constants". In: *Journal of Molecular Structure* 246.3 (1991), pp. 257–266. ISSN: 0022-2860. DOI: https://doi.org/10.1016/0022-2860(91)80132-N. URL: https://www.sciencedirect.com/science/article/pii/002228609180132N.

[52] Nicola Marzari. "Intro to DFT - Day 1: Density-functional theory - Nicola Marzari". In: *Materials Cloud* (2020). URL: https://www.youtube.com/watch?v=kYxOWYWxYcQ.

[53] Ralf Stubner. "Diagrammatic techniques for time-dependent density-functional theory". PhD thesis. Friedrich-Alexander-Universität Erlangen-Nürnberg, 2005.

[54] Andreas Dreuw and Michael Wormit. "The algebraic diagrammatic construction scheme for the polarization propagator for the calculation of excited states". In: *WIREs Computational Molecular Science* 5.1 (2015), pp. 82–95. DOI: https://doi.org/10.1002/wcms.1206. eprint: https://wires.onlinelibrary.wiley.com/doi/pdf/10.1002/wcms.1206. URL: https://wires.onlinelibrary.wiley.com/doi/abs/10.1002/wcms.1206.

[55] Tobias Brandes. *The Two-Level System: Time-Evolution - Time Evolution of States*. 2004. URL: https://www1.itp.tu-berlin.de/brandes/public_html/qm/umist_qm/node74.html.

[56] Tobias Brandes. *Energy Measurements - Eigenstates of the Two-Level System*. 2004. URL: https://www1.itp.tu-berlin.de/brandes/public_html/qm/umist_qm/node69.html.

[57] Wolfram Research Inc. *Mathematica, Version 12.3.1*. Champaign, IL, 2021. URL: https://www.wolfram.com/mathematica.

[58] Oliver Benson. *Interaction of Atoms With a Classical Light Field*. 2009. URL: https://www.physik.hu-berlin.de/de/nano/lehre/copy_of_quantenoptik09/Chapter7.

[59] Edward U. Condon. "Nuclear Motions Associated with Electron Transitions in Diatomic Molecules". In: *Phys. Rev.* 32 (6 Dec. 1928), pp. 858–872. DOI: 10.1103/PhysRev.32.858. URL: https://link.aps.org/doi/10.1103/PhysRev.32.858.

[60] Arthur Beiser. *Concepts of Modern Physics*. sixth edition. McGraw-Hill, 2003. ISBN: 0-07-244848-2.

[61] V. Gligorijević et al. "Structure-based protein function prediction using graph convolutional networks". In: *Nature Communications* 12 (2021). DOI: 10.1038/s41467-021-23303-9. URL: https://doi.org/10.1038/s41467-021-23303-9.

[62] Kara Rogers. *What Is the Difference Between a Peptide and a Protein?* Accessed 12 October 2021. URL: https://www.britannica.com/story/what-is-the-difference-between-a-peptide-and-a-protein.

[63] Daniel E. Koshland and Felix Haurowitz. *General structure and properties of proteins – The amino acid composition of proteins*. Accessed 12 October 2021. URL: https://www.britannica.com/science/protein/General-structure-and-properties-of-proteins.

[64] Maryam M. Javadpour et al. "Helix Packing in Polytopic Membrane Proteins: Role of Glycine in Transmembrane Helix Association". In: *Biophysical Journal* 77.3 (1999), pp. 1609–1618. ISSN: 0006-3495. DOI: https://doi.org/10.1016/S0006-3495(99)77009-8. URL: https://www.sciencedirect.com/science/article/pii/S0006349599770098.

[65] P.H. Cannington and Norman S. Ham. "He(I) and He(II) photoelectron spectra of glycine and related molecules". In: *Journal of Electron Spectroscopy and Related Phenomena* 32.2 (1983), pp. 139–151. ISSN: 0368-2048. DOI: https://doi.org/10.1016/0368-2048(83)85092-0. URL: https://www.sciencedirect.com/science/article/pii/0368204883850920.

[66] Oksana Plekan et al. "Investigation of the Amino Acids Glycine, Proline, and Methionine by Photoemission Spectroscopy". In: *The Journal of Physical Chemistry A* 111.43 (2007). PMID: 17918919, pp. 10998–11005. DOI: 10.1021/jp075384v. eprint: https://doi.org/10.1021/jp075384v. URL: https://doi.org/10.1021/jp075384v.

[67] H. J. Svec and D. D. Clyde. "Vapor Pressures of Some α-Amino Acids." In: *Journal of Chemical & Engineering Data* 10.2 (1965), pp. 151–152. DOI: 10.1021/je60025a024. eprint: https://doi.org/10.1021/je60025a024. URL: https://doi.org/10.1021/je60025a024.

[68] Ingrid M. Weiss et al. "Thermal decomposition of the amino acids glycine, cysteine, aspartic acid, asparagine, glutamic acid, glutamine, arginine and histidine". In: *bioRxiv* (2017). DOI: 10.1101/119123. eprint: https://www.biorxiv.org/content/early/2017/03/22/119123.full.pdf. URL: https://www.biorxiv.org/content/early/2017/03/22/119123.

[69] Thomas Miller and David Clary. "Quantum free energies of the conformers of glycine on an ab initio potential energy surface". In: *Phys. Chem. Chem. Phys.* 6 (May 2004).

[70] Fan Liu, Jing Yu, and Yan-Ru Huang. "High-level theoretical study of the evolution of abundances and interconversion of glycine conformers". In: *Chinese Physics B* 27 (Apr. 2018), p. 043102. DOI: 10.1088/1674-1056/27/4/043102.

[71] Roman M. Balabin. "Experimental thermodynamics of free glycine conformations: the first Raman experiment after twenty years of calculations". In: *Phys. Chem. Chem. Phys.* 14 (1 2012), pp. 99–103. DOI: 10.1039/C1CP20805E. URL: http://dx.doi.org/10.1039/C1CP20805E.

[72] Chantal T. Falzon and Feng Wang. "Understanding glycine conformation through molecular orbitals". In: *The Journal of Chemical Physics* 123.21 (2005), p. 214307. DOI: 10.1063/1.2133727. eprint: https://doi.org/10.1063/1.2133727. URL: https://doi.org/10.1063/1.2133727.

[73] Mario T. Rosado, Maria Leonor T.S. Duarte, and Rui Fausto. "Vibrational spectra of acid and alkaline glycine salts". In: *Vibrational Spectroscopy* 16 (1998), pp. 35–54. URL: https://core.ac.uk/download/pdf/144022643.pdf.

[74] Santosh Kumara et al. "Vibrational spectrum of glycine molecule". In: *Spectrochimica Acta Part A* 61 (2005), pp. 2741–2746. DOI: 10.1016/j.saa.2004.09.029.

[75] Riccardo Mincigrucci et al. “Impulsive UV-pump/X-ray probe study of vibrational dynamics in glycine”. In: *Scientific Reports* 8 (2018). DOI: 10.1038/s41598-018-33607-4. URL: https://doi.org/10.1038/s41598-018-33607-4.

[76] B. Maté et al. “An infrared study of solid glycine in environments of astrophysical relevance”. In: *Physical Chemistry Chemical Physics* 13(26) (2011). DOI: 10.1039/c1cp20899c. URL: https://pubs.rsc.org/en/content/articlepdf/2011/cp/c1cp20899c.

[77] A. Gómez-Zavaglia and R. Fausto. “Low-temperature solid-state FTIR study of glycine, sarcosine and N,N-dimethylglycine: observation of neutral forms of simple α-amino acids in the solid state”. In: *Physical Chemistry Chemical Physics* 15 (2003). DOI: 10.1039/B304888H. URL: https://pubs.rsc.org/en/content/articlelanding/2003/CP/B304888H.

[78] E. Itälä et al. “Soft x-ray ionization induced fragmentation of glycine”. In: *The Journal of Chemical Physics* 140.23 (2014), p. 234305. DOI: 10.1063/1.4882648. eprint: https://doi.org/10.1063/1.4882648. URL: https://doi.org/10.1063/1.4882648.

[79] David Schwickert et al. *Electronic Quantum Coherence in Glycine Molecules Probed with Ultrashort X-ray Pulses in Real Time*. 2021. arXiv: 2012.04852 [physics.chem-ph].

[80] Gwyn P. Williams. *ELECTRON BINDING ENERGIES*. [Online; Stand 6. Juli 2021]. 2000. URL: https://xdb.lbl.gov/Section1/Table_1-1a.htm.

[81] M. Cardona and L. Ley, eds. *Photoemission in Solids I, General Principles*. Vol. 26. Springer-Verlag Berlin Heidelberg, 1978. ISBN: 978-3-662-30919-3. DOI: 10.1007/3-540-08685-4.

[82] Robert J. Goldston and Paul H. Rutherford, eds. *Introduction to plasma physics*. Institute of Physics Publishing Bristol and Philadelphia, 1995. ISBN: 0750303255.

[83] HELM. *Workbook 27: Multiple Integration*. Changing Coordinates. 2008. URL: https://learn.lboro.ac.uk/archive/olmp/olmp_resources/pages/workbooks_1_50_jan2008/Workbook27/27_4_chng_coords.pdf.

[84] Daniel Junge. “Design einer Regelungsschleife zur Stabilisierung einer Röntgenpulssequenz”. MA thesis. Technische Hochschule Lübeck, 2020.

[85] Ingrid Daubechies. “The wavelet transform, time-frequency localization and signal analysis”. In: *IEEE Transactions on Information Theory* 36.5 (1990), pp. 961–1005. DOI: 10.1109/18.57199.

[86] Jonathan M. Lilly and Sofia C. Olhede. “Generalized Morse Wavelets as a Superfamily of Analytic Wavelets”. In: *IEEE Transactions on Signal Processing* 60.11 (2012), pp. 6036–6041. DOI: 10.1109/TSP.2012.2210890.

[87] Amir-Homayoon Najmi and John Sadowsky. “The Continuous Wavelet Transform and Variable Resolution Time–Frequency Analysis”. In: *Johns Hopkins APL Technical Digest (Applied Physics Laboratory)* 18.1 (1997), pp. 134–139. URL: https://www.jhuapl.edu/Content/techdigest/pdf/V18-N01/18-01-Najmi.pdf.

[88] Christopher Torrence and Gilbert P. Compo. “A Practical Guide to Wavelet Analysis”. In: *Bulletin of the American Meteorological Society* 79.1 (1998), pp. 61–78. DOI: 10.1175/1520-0477(1998)079<0061:APGTWA>2.0.CO;2. URL: https://journals.ametsoc.org/view/journals/bams/79/1/1520-0477_1998_079_0061_apgtwa_2_0_co_2.xml.

[89] B Faatz et al. “Simultaneous operation of two soft x-ray free-electron lasers driven by one linear accelerator”. In: *New Journal of Physics* 18.6 (June 2016), p. 062002. DOI: 10.1088/1367-2630/18/6/062002. URL: https://doi.org/10.1088/1367-2630/18/6/062002.

[90] K. Tiedtke et al. “Gas detectors for x-ray lasers”. In: *Journal of Applied Physics* 103.9 (2008), p. 094511. DOI: 10.1063/1.2913328. eprint: https://doi.org/10.1063/1.2913328. URL: https://doi.org/10.1063/1.2913328.

[91] Markus Braune et al. “A non-invasive online photoionization spectrometer for FLASH2”. In: *Journal of Synchrotron Radiation* 23.1 (Jan. 2016), pp. 10–20. DOI: 10.1107/S1600577515022675. URL: https://doi.org/10.1107/S1600577515022675.

[92] S. Palutke et al. “Spectrometer for shot-to-shot photon energy characterization in the multi-bunch mode of the free electron laser at Hamburg”. In: *Review of Scientific Instruments* 86.11 (2015), p. 113107. DOI: 10.1063/1.4936293. eprint: https://doi.org/10.1063/1.4936293. URL: https://doi.org/10.1063/1.4936293.

[93] CXRO The Center for X-Ray Optics. *X-Ray Interactions With Matter*. 2010. URL: https://henke.lbl.gov/optical_constants/.

[94] B.L. Henke, E.M. Gullikson, and J.C. Davis. “X-Ray Interactions: Photoabsorption, Scattering, Transmission, and Reflection at E = 50-30,000 eV, Z = 1-92”. In: *Atomic Data and Nuclear Data Tables* 54.2 (1993), pp. 181–342. ISSN: 0092-640X. DOI: https://doi.org/10.1006/adnd.1993.1013.

[95] Sergey Usenko et al. “Attosecond interferometry with self-amplified spontaneous emission of a free-electron laser”. In: *Nature Communications* 8 (2017). Molecular Wave Packet Dynamics. ISSN: 2041-1723. DOI: 10.1038/ncomms15626. URL: https://doi.org/10.1038/ncomms15626.

[96] Kai Schlage et al. *Apparatus for depositing material on the surface of a substrate*. US patent 11193201, July 2021.

[97] SmarAct GmbH. *PicoScale User Manual*. 2.1.11. SmarAct GmbH. Schuette-Lanz-Strasse 9, D-26135 Oldenburg, 2019.

[98] Zoltán Sárosi et al. “Evaluation of reflectivity of metal parts by a thermo-camera”. In: Nov. 2010.

[99] Shlomo Hava, J. Ivri, and Mark Auslender. “Reflection of infrared radiation from lamellar gratings on a silicon wafer”. In: *Journal of Applied Physics* 85 (June 1999), p. 7893. DOI: 10.1063/1.370603.

[100] Rebecca Grinham and Andrew Chew. “Gas Correction Factors for Vacuum Pressure Gauges”. In: *Vakuum in Forschung und Praxis* 29 (2 Apr. 2017), pp. 25–30. DOI: 10.1002/vipr.201700640. URL: https://doi.org/10.1002/vipr.201700640.

[101] C. B. Lucas, ed. *Atomic and Molecular Beams, Production and Collimation*. CRC Press, 2014. ISBN: 978-1-4665-6106-9.

[102] Sascha Deinert. “Aufbau eines hocheffizienten Photoelektron-Photoion-Koinzidenzexperiments”. PhD thesis. Universität Hamburg, 2013.

[103] H Pulkkinen et al. “Correlation effects in the - MM Auger transitions of Ar”. In: *Journal of Physics B: Atomic, Molecular and Optical Physics* 29.14 (July 1996), pp. 3033–3050. DOI: 10.1088/0953-4075/29/14/016. URL: https://doi.org/10.1088/0953-4075/29/14/016.

[104] Linde Gas GmbH. *Helium 5.0; Neon 4.5; Argon 5.0; Krypton 4.0*. 09.07.2021. Linde Gas GmbH. Carl-von-Linde-Platz 1, A-4651 Stadl-Paura, 2021.

[105] P. Kolorenč and V. Averbukh. “Fano-ADC(2,2) method for electronic decay rates”. In: *The Journal of Chemical Physics* 152.21 (2020), p. 214107. DOI: 10.1063/5.0007912. eprint: https://doi.org/10.1063/5.0007912. URL: https://doi.org/10.1063/5.0007912.

[106] J Schirmer et al. “Break-down of the molecular-orbital picture of ionization: CS, PN and P2”. In: *Journal of Physics B: Atomic and Molecular Physics* 11.11 (June 1978), pp. 1901–1915. DOI: 10.1088/0022-3700/11/11/007. URL: https://doi.org/10.1088/0022-3700/11/11/007.

[107] Peter Atkins and Julio de Paula. *ATKINS’ PHYSICAL CHEMISTRY*. eigth edition. W. H. Freeman and Company, 2006. ISBN: 0-7167-8759-8.

[108] G. Boultadakis, K. Skrapas, and P. Frangos. “Time-Frequency Analysis of Radar Signals”. In: (2004). URL: https://www.google.com/url?sa=t&rct=j&q=&esrc=s&source=web&cd=&ved=2ahUKEwjcgoT4wKr1AhX4SfEDHe5OCiwQFnoECAQQAQ&url=https%3A%2F%2Fwww.sto.nato.int%2Fpublications%2FSTO%2520Meeting%2520Proceedings%2FRTO-MP-SET-080%2FMP-SET-080-07.pdf&usg=AOvVaw0oBeDE6EK_58jGD5PQk4BU.

[109] Iñaki Tuñón et al. “Intramolecular Proton Transfer of Glycine in Aqueous Solution Using Quantum Mechanics–Molecular Mechanics Simulations”. In: *The Journal of Physical Chemistry A* 102.45 (1998), pp. 8673–8678. DOI: 10.1021/jp982162b. eprint: https://doi.org/10.1021/jp982162b. URL: https://doi.org/10.1021/jp982162b.

[110] P. Lablanquie et al. “Multielectron Spectroscopy : Auger decays of the Argon 2p hole”. In: *Journal of Electron Spectroscopy and Related Phenomena* 156-158 (2007), pp. 222–231. DOI: doi:10.1016/j.elspec.2006.11.062.

[111] P. Goupillaud, A. Grossmann, and J. Morlet. “Cycle-octave and related transforms in seismic signal analysis”. In: *Geoexploration* 23.1 (1984). Seismic Signal Analysis and Discrimination III, pp. 85–102. ISSN: 0016-7142. DOI: https://doi.org/10.1016/0016-7142(84)90025-5. URL: https://www.sciencedirect.com/science/article/pii/0016714284900255.

[112] Alexander I. Kuleff, Siegfried Lünnemann, and Lorenz S. Cederbaum. “Electron-correlation-driven charge migration in oligopeptides”. In: *Chemical Physics* 414 (2013). Attosecond spectroscopy, pp. 100–105. ISSN: 0301-0104. DOI: https://doi.org/10.1016/j.chemphys.2012.02.019. URL: https://www.sciencedirect.com/science/article/pii/S030101041200095X.

[113] Morgane Vacher, Michael J. Bearpark, and Michael A. Robb. “Communication: Oscillating charge migration between lone pairs persists without significant interaction with nuclear motion in the glycine and Gly-Gly-NH-CH3 radical cations”. In: *The Journal of Chemical Physics* 140.20 (2014), p. 201102. DOI: 10.1063/1.4879516. eprint: https://doi.org/10.1063/1.4879516. URL: https://doi.org/10.1063/1.4879516.

[114] A. Marinelli et al. “High-intensity double-pulse X-ray free-electron laser”. In: *Nature Communications* 6 (2015). ISSN: 2041-1723. DOI: https://doi.org/10.1038/ncomms7369. URL: https://doi.org/10.1038/ncomms7369.

[115] A. Lutman et al. “Fresh-slice multicolour X-ray free-electron lasers”. In: *Nature Photonics* 10 (2016). ISSN: 1749-4893. DOI: 10.1038/nphoton.2016.201. URL: https://doi.org/10.1038/nphoton.2016.201.

[116] A. Marinelli et al. “Multicolor Operation and Spectral Control in a Gain-Modulated X-Ray Free-Electron Laser”. In: *Phys. Rev. Lett.* 111 (13 Sept. 2013), p. 134801. DOI: 10.1103/PhysRevLett.111.134801. URL: https://link.aps.org/doi/10.1103/PhysRevLett.111.134801.

List of Figures

Acknowledgements

Special thanks to current and former group members: Andreas Przystawik, Sergey Usenko, Samuel Hartwell, Malte Sumfleth, Slawomir Skruszewicz, Mahesh Namboodiri, Markus Jakob, Leslie Lazzarino, Lena Worbs, Florian Jacobs, Daniel Junge, Ekaterina Izotova, Luis Carretero, Evgeny Saldin and Tim Laarmann; all participating colleagues: Sven Toleikis, Karolin Baev, Steffen Palutke and Sascha Deinert; as well as all members of the SFB925 and PIER, the FLASH infrastructure group and the mechanical and electronic workshops and collaborators from the University of Kassel, the Helmut-Schmidt-University (especially Anton Vorobiov and Christian Haunhorst) and Imperial College London (especially Marco Ruberti, Vitali Averbukh and Jon Marangos).